FABRICATION, CHARACTERIZATION, AND CHEMICAL MODIFICATION OF PLASMONIC DEVICES

by

Matthew J. Kofke

B.S., Carnegie Mellon, 2003

Submitted to the Graduate Faculty of

Dietrich School of Arts and Sciences in partial fulfillment

of the requirements for the degree of

Doctor of Philosophy

University of Pittsburgh

2012

UNIVERSITY OF PITTSBURGH

DIETRICH SCHOOL OF ARTS AND SCIENCES

This dissertation was presented

by

Matthew Joseph Kofke

It was defended on

August 14th, 2012

and approved by

Dr. Geoffrey Hutchison, Assistant Professor, University of Pittsburgh Department of Chemistry

Dr. Nathaniel Rosi, Assistant Professor, University of Pittsburgh Department of Chemistry

Dr. David Yaron, Associate Professor, Carnegie Mellon Department of Chemistry

Dr. David H. Waldeck, Professor, University of Pittsburgh Department of Chemistry

FABRICATION, CHARACTERIZATION, AND CHEMICAL MODIFICATION OF PLASMONIC DEVICES

Matthew Joseph Kofke

University of Pittsburgh, 2012

Fabrication, Characterization and Chemical Modification of Plasmonic Devices

Matthew J. Kofke, PhD

University of Pittsburgh, 2012

Metallic structures with feature sizes on the order of the wavelength of light show numerous optical phenomena which have been attributed to excitation of surface plasmons upon the structures. The ability to prepare and characterize metallic nanostructures has resulted in a host of novel applications ranging from biosensing to optoelectronics, both for devices integrated on chips and small nanoparticles in solution. In order to fully realize the potential of such plasmonic devices a better understanding of the fundamental physical processes responsible for the observed phenomena is essential. This dissertation explores the underlying process of the extraordinary optical transmission (EOT) mechanism in nanoaperture array plasmonic devices. The first part of this work explores how surface plasmon polaritons influence the EOT in two dimensional annular aperture arrays. This study is followed by an analysis of the geometrical factors of the nanoaperture in the array and how they impact the observed transmission. From these data, the role of localized surface plasmons, which are supported by the central disk of the annular aperture, are found to have significant effects on the device performance. These findings were demonstrated further by designing devices composed of a nanoparticle nested in a nanoslit in which the only mechanism for observed EOT is through localized plasmon resonances on the nanoparticles. Lastly, a novel method for conducting seedless anisotropic synthesis upon both Au nanoapertures and substrate bound Au nanoparticles is described, and control of the resultant nanostructures through alteration of either the surface chemistry or the growth solution conditions is demonstrated. The topics covered here should enable a deeper understanding of EOT in nanoaperture arrays as well as establish new pathways for making plasmonic devices.

TABLE OF CONTENTS

LIST OF FIGURES

DEDICATION

This work is dedicated to the significant people in my life who have helped me achieve my personal and professional goals:

My parents: Marianne and Andrew Kofke, for their unconditional love, support, and guidance.

My wonderful wife Genie and our son Sean: You are my world.

ACKNOWLEDGEMENTS

I am grateful to the many people who helped though my graduate journey. Dr. David Waldeck has been an excellent graduate advisor. He helped me to grow both personally and professionally and has always been understanding and patient during the challenging moments. His support provided me with a sandbox from which I was able to develop a robust skillset and appreciation for Chemistry and Nanotechnology, and for that experience, I am truly grateful. Our weekly meetings to discuss my research were always enjoyable and provided a great push for me to accomplish my goals.

I also thank the many professors who made themselves available for me during my time at Pitt. Dr. Gilbert Walker for his support and for suggesting we investigate annular aperture arrays. The trips to Toronto for the BiopSys meetings were very enjoyable and educational. I would also like to thank Dr. David Pratt for inviting me into his lab my first summer at Pitt and serving on my comprehensive exam committee. I really enjoyed learning about the nature of his research in high resolution spectroscopy and discussions about my career ambitions. I thank Dr. Nathaniel Rosi and Dr. Geoffrey Hutchison for serving on my dissertation committee. Also, I would like to thank Prof. Sanford Asher for serving on my comprehensive exam committee and for his excellent class in spectroscopy. I thank Prof. Haitao Liu for serving as my proposal committee chair and Prof. Millstone for serving on my proposal committee as well as giving me

research advice. I thank Prof. David Yaron from Carnegie Mellon for serving on my dissertation committee and being my mentor and friend during my undergraduate years.

The members of the Waldeck research group have been an asset to my success at Pitt. I thank Dr. Palwinder Kaur for helping me become accustomed to my research project. Dr. Emil Wierzbinski has been a great colleague and friend. He has helped me solve many difficult research problems and has been an excellent mentor. I thank Daniel Lamont for his constant patience answering all my questions about optics and photonics. I am also grateful to have worked with and learned from Dr. Amit Paul, Dr. Subhasis Chakrabarti, Dr. Lei Wang, Dr. Kathryn Davis, Dr. Hongjun Yue, Dr. Mingyan Wu, Xing Yin, Yang Wang, Robin Sloan, Brian Bloom, Brittney Graff, Madu Mendis, Hao Lu, Dr. Prasun Mukherjee, and Dr. Himadri Mandal. Thanks also to Dr. Justin Young and Dr. Leo Alvarez for their friendship and scholarly assistance. I also thank my collaborators Dr. Shell Ip, Dr. Zahra Fakhraai and Dr. Jianjun Wei.

I owe many thanks to Michael McDonald from the Peterson Institute for Nanoscience and Engineering. Throughout my graduate career the nanoscience center was like a second home and Mike made me feel welcome. I was able to learn about many aspects of nanofabrication and characterization and the skillset I was able to develop will serve me well throughout my career. I also thank Dr. Susheng Tan for his help with the characterization instruments and assistance with TEM images. I thank Matthew France, for providing technical support for the nanofabrication instruments. I am also thankful for the technical support and nanofabrication assistance of Carsen Kline and Chris Bowman from the Carnegie Mellon University Nanofabrication Facility.

I thank the chemistry department staff. The machine shop, especially Tom and Jeff, were very helpful both at solving mechanical problems with lab equipment as well as with the design

of specialized devices for my experiments. The graduate office has always been helpful and supportive at every milestone in my graduate experience. Starting with my initial visit through my dissertation defense, they handled all administrative elements of the graduate process with competency and professionalism.

Lastly, I thank my family for the unconditional love and support during this challenging period in my life. I would not have been able to reach this goal were it not for the solid foundation provided by my parents: Andrew and Marianne Kofke, my Siblings: Elise, Lauren and her husband Stas, as well as Marisa and her husband Manny. I am thankful to Ted Maniet, and Dave and Tammy Kofke for their support. I also thank my grandparents Edward and Anna Maniet and William and Maureen Kofke for their kindness and support throughout my life. To my wife Genie, I love you. I could not have imagined when I started graduate school that the girl I randomly met at a swing dance in Squirrel Hill would become my dance partner through life's song.

1.0 INTRODUCTION

Nanoscale metal structures have generated considerable interest since Ebbesen and coworkers[1] demonstrated that an array of subwavelength holes transmits more light than predicted by classical diffraction theory[2] and correlated the extraordinary optical transmission (EOT) to the resonant excitation of surface plasmons[3] that arise from the periodic nature of the arrays[4]. On a fundamental level this discovery has sparked interest in the basic process underlying the ability of a nanoaperture to tunnel light with high efficiency and the physics of surface plasmons. On an applied level this work has encouraged researchers to explore the potential for creating nanoscale sensors[5], communication devices[6], optical circuits[7], and other devices from such arrays. This dissertation is focused on the field of plasmonics and understanding the complex processes that are responsible for the EOT phenomenon in nanoaperture array devices with nested nanoparticles, as well as developing novel strategies to modify nanoaperture with optically resonant nanoparticles through chemical means.

This chapter provides necessary background information for understanding better the findings documented in this thesis. The important physical concepts about exciting surface plasmons and their role in EOT is introduced, followed by a discussion of localized plasmon resonances and their relevant optical phenomena. Next, chemical approaches towards synthesizing anisotropic nanoparticles are covered. Lastly, the various fabrication strategies

employed for making nanoaperture arrays, randomly oriented nanoaperture, and alkanethiol self-assembled monolayers is discussed.

1.1 WHAT IS A SURFACE PLASMON?

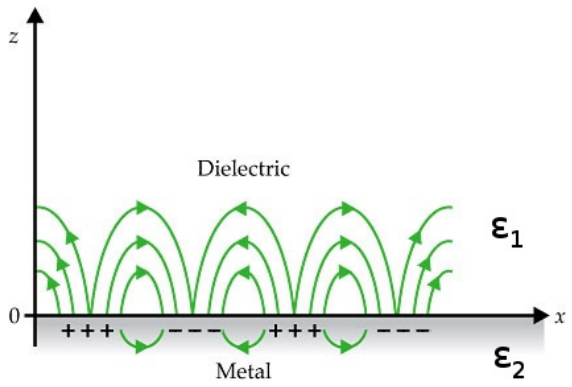

Figure 1.1. E-field diagram of a propagating surface plasmon at a metal/dielectric interface, adapted from ref. 8.

Surface plasmons, or surface plasma waves, are propagating collective oscillations in the free electron gas of a metal (Fig 1.1). This wave has an oscillating field profile along the surface and an evanescent electromagnetic field that extends in the normal (±z) direction into both the metal (for non-perfect conductors) and dielectric. As illustrated by the figure, the electric field extends substantially further into the dielectric, but still decays exponentially away from the metal/dielectric interface[8]. In essence a surface plasmon is a special type of waveguide in which the boundary is the interface between a metal and a dielectric, instead of two dielectrics such as in a typical fiber optic waveguide.

Unlike light in vacuum, which has the dispersion relationship $k_o = \frac{\omega}{c}$ (where k_o represents the wave vector in the direction of propagation, ω is the frequency, and c is the speed of light) the dispersion relationship for a surface plasmon polariton[3] is

$$k_{spp} = k_o \sqrt{\frac{\varepsilon_1 \varepsilon_2}{\varepsilon_1 + \varepsilon_2}} \tag{1.1}$$

where ε_1 is the dielectric function of medium 1(typically a dielectric material) and ε_2 is the dielectric function of medium 2(the metal). For this relationship to be valid the absolute value of ε_2 must be greater than ε_1 and ε_2 must be less than 0. The complex dielectric function for the metal, ε_2, varies with the frequency of the electromagnetic field incident upon it and can be approximated by the Drude model[9] as

$$\varepsilon_2(\omega) = \varepsilon_2(\infty) - \frac{{\omega_p}^2}{\omega - i\gamma_2 \omega} \tag{1.2}$$

where $\varepsilon_2(\infty)$ represents the dielectric function at very high frequency, ω_p is the plasma frequency for the metal, ω is the frequency of electromagnetic radiation incident on the metal, and γ_2 is the damping term which accounts for absorptive losses within the metal. This model is in good agreement with experimental data[10] for optical energies < 3eV.

1.2 EXCITING SURFACE PLASMONS

Two primary concepts are used to relate the physics of a surface plasmon to a photon: phase velocity and momentum. The momentum of a photon is given as $\mathbf{p} = \hbar\mathbf{k}$ and the phase velocity is given as $\mathbf{v} = \omega/\mathbf{k}$ (equivalently expressed as $v = c/n$ since $\omega = ck_o/n$). Comparing the

wavevectors of both light and surface plasmons provides the criterion for conservation of momentum when exciting a surface plasmon.

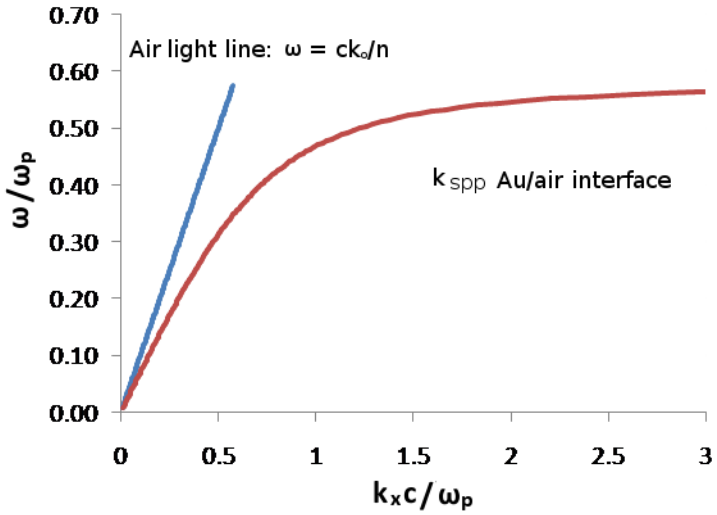

Figure 1.2. SPP dispersion curve for light propagating in air incident on a metal film (blue) and SPP dispersion (red).

To excite a surface plasmon the following condition must be met:

$$k_x(\omega) = k_{spp}(\omega) \tag{1.3}$$

Light incident on a metal film will have a wavevector parallel to the x-axis: $k_x = k_o \sin(\theta)$. As shown by figure 1.2, the dispersion curve lies below the light line in vacuum at all frequencies ω. The wavevector component k_x is less than k_{spp}, which implies that it is not possible to excite a surface plasmon by simply illuminating a metal film, at any angle. For frequencies $\omega << \omega_p$, both the dispersion of light and surface plasmon exhibit linear behavior. However, as the frequency increases, the curve corresponding to a surface plasmon begins to asymptotically approach a maximum value which, for a Drude-like metal is $\omega_p / \sqrt{2}$. This represents the maximum frequency at which a surface plasmon can be supported.

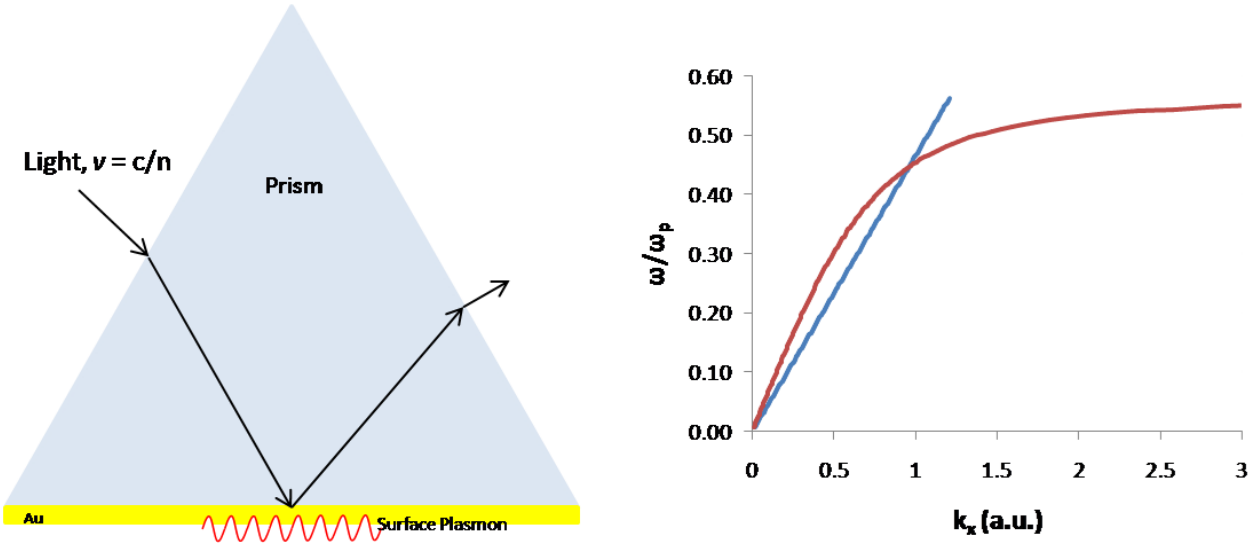

Figure 1.3. Cartoon of ATR prism SPP excitation (left) and dispersion relationship in which the light line now intersects the dispersion of a surface plasmon(right).

A common method to overcome the momentum mismatch between the incident wavevector and a surface plasmon polariton wavevector is to change the dielectric constant for the medium of the incident light so that the photon's dispersion line is less steep. This can be achieved by using a prism configured for attenuated total internal reflection[11] (Fig 1.3). For a prism with a refractive index, $n \approx 2$, the phase velocity of light in the prism will change by $v = c/n$, slowing the velocity of light.

Light propagating through a medium with $n > n_{air}$, such as a prism, changes the relationship between the light line $\omega = ck_o/n$ and k_{spp} for a surface plasmon. At the appropriate frequency, the magnitude of both k_x and k_{spp} are equal and a surface plasmon can be excited. On the graph in figure 1.3 this condition occurs for the intersection between the blue line (light line) and the k_{SPP} dispersion line (red). Currently, this method is the most popular for exciting surface plasmons, and it has seen numerous applications in biological sensing[12].

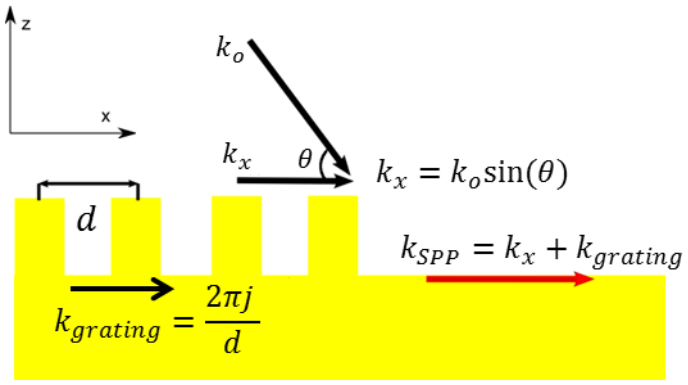

Figure 1.4. Cartoon image of a surface plasmon being excited by a metallic grating.

Another common method to satisfy the surface plasmon resonance condition is to introduce a periodic corrugation onto the surface (Figure 1.4). In reciprocal space, any periodic structure has a momentum vector which correlates to the reciprocal lattice vector of the structure along a given axis[13]. In the case of a 1D grating, $k_{grating} = 2\pi j/d$ where d represents the period of the grating and j is an integer, the term $2\pi/d$ is the reciprocal unit vector. Light incident upon a grating structure has an x-component, which can additively combine with $k_{grating}$ to satisfy the relationship

$$k_x \pm k_{grating} = k_{spp} \tag{1.4}$$

whereupon a surface plasmon with wavevector k_{spp} can be excited and propagate at the air/metal interface. It is also possible for the reverse process to occur; a propagating surface plasmon can scatter off of a grating structure back into far field radiation.

1.3 NANOAPERTURES AND WAVEGUIDES

A nanoaperture is the popular colloquialism which refers to an aperture in an optically thick metal film whose radius r << λ of light incident upon it. Bethe and Bouwkamp[2] solved the problem of electromagnetic field transmission for a subwavelength aperture. At the limit when $r << \lambda$ the transmission scales as

$$T = \frac{64}{27\pi^2}(k_o r)^4 \propto \left(\frac{r}{\lambda}\right)^4 \tag{1.5}$$

where $k_o = \frac{2\pi}{\lambda_o}$; thus as the radius of the aperture decreases, the transmission through the aperture, T, scales as $\left(\frac{r}{\lambda}\right)^4$. This result implies that subwavelength apertures should transmit light with poor efficiency. The Bethe-Bouwkamp theory has limitations, however. Namely, it assumes the film to be an infinitely thin perfect conductor, so that it does not account for geometrical effects other than the aperture radius.

It is well known that cylindrical holes can function as waveguides. A cylindrical waveguide is a medium which in three dimensions has the shape of a cylinder and it transects an opaque material such as a metal (fig 1.5).

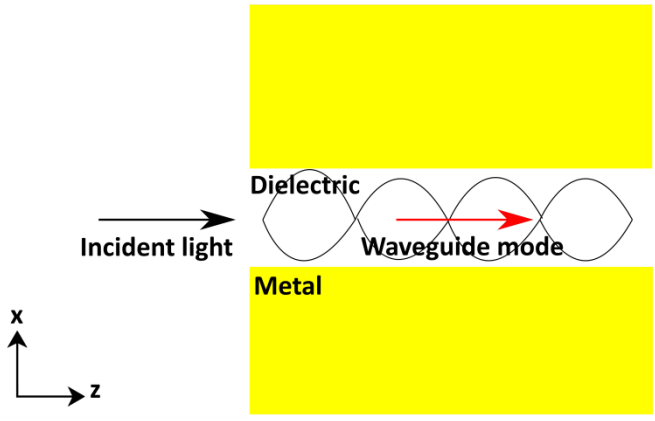

Figure 1.5: A cartoon for a cylindrical waveguide (side view).

Due to the geometry of the cylinder, it is possible for light incident upon it to couple into guided modes, which are standing waves that propagate down the length of the waveguide. Using the geometry of the waveguide for the boundary conditions, it is possible to derive the cutoff frequency from the equations for light. Typically boundary conditions are defined for metals modeled as perfect electric conductors (PEC) to simplify the analysis while retaining the important physical parameters. Cylindrical waveguides have both TE and TM standing wave solutions. TE solutions correspond to modes in which the E-field has zero magnitude along the z-axis, or direction of propagation, and likewise for TM modes the H-field has no magnitude along the z-axis.

A special kind of cylindrical waveguide known as a coaxial waveguide is of particular interest to this work. Depicted in figure 1.6, a coaxial waveguide consists of a cylindrical aperture in an optically thick metal film with a metallic island located centrally inside the cylinder. The important geometric parameters are the inner radius, R1, and outer radius R2.

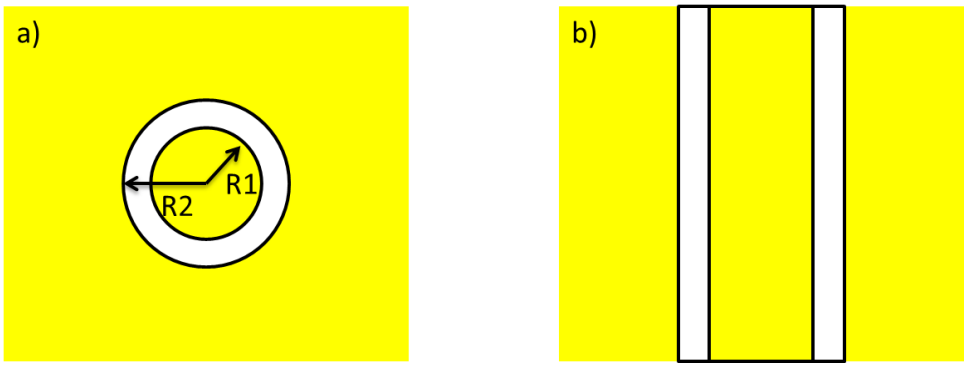

Figure 1.6. A cartoon diagram of a coaxial waveguide mode; a) top view and b) side view.

The general dispersion relation for modes within a coaxial waveguide can be expressed as[14]:

$$k_z{}^2 = \frac{4\pi^2}{\lambda_c{}^2} - \frac{4\pi^2}{\lambda_o{}^2} \tag{1.6}$$

where k_z is the propagation constant along the *z*-axis, λ_o is the wavelength of light incident on the structure and λ_c is the cutoff wavelength of the waveguide mode. In general, a coaxial waveguide can support propagating modes with wavelength λ_o below the cutoff wavelength λ_c. In the case where $\lambda_o > \lambda_c$, the transmission becomes lossy. For a coaxial waveguide TE mode, the cutoff wavelength is defined as[14]:

$$\lambda_{cTE_{n,1}} = \frac{\pi(R1 + R2)}{n} \tag{1.7}$$

where *R1* and *R2* represent the inner and outer radius as seen in figure 1.6 and *n* represents the order of the mode. For $n = 1$, a TE_{11} waveguide mode has a cutoff frequency determined by the sum of the inner and outer radius of the coaxial structure.

1.4 NANOAPERTURE ARRAYS AND EXTRAORINDARY OPTICAL TRANSMISSION

As observed in section 1.2, periodic corrugations in a metal surface can satisfy the momentum matching condition for launching SPPs. Two dimensional nanoaperture arrays (Fig 1.7), which are nanoapertures laid out in an array fashion with a fixed hole-to-hole spacing as well as symmetry (square/hexagonal/rhombic, etc) are analogous to a grating. Owing to the periodic corrugations, nanoaperture arrays are able to launch SPPs. In addition, discovered by Ebbesen *et al*, nanoaperture arrays transmit certain wavelengths of light with an efficiency that is significantly greater than that predicted by Bethe-Bouwkamp theory.

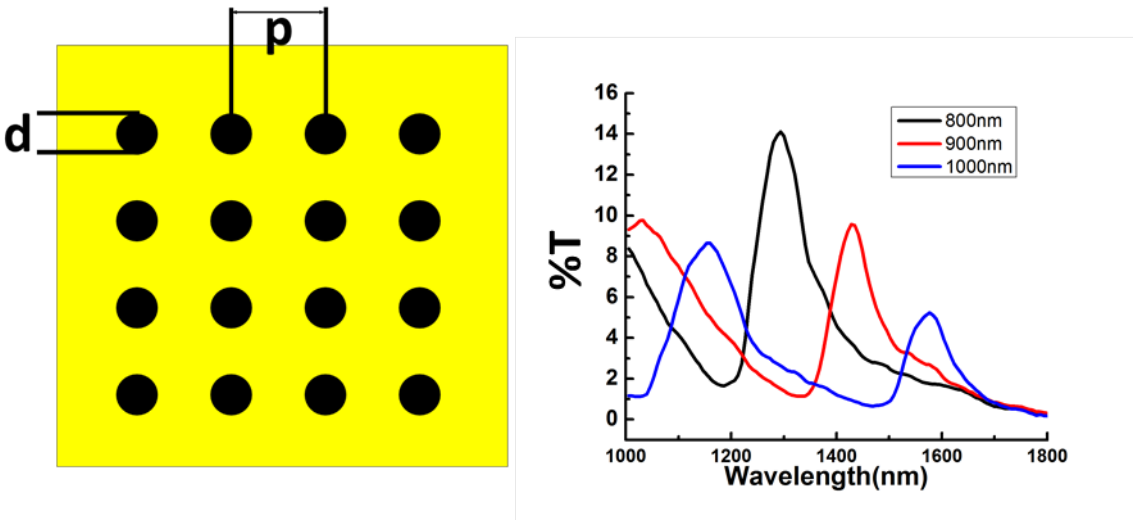

Figure 1.7. Cartoon (left) and experimental transmission spectra (right) of a two-dimensional cylindrical nanoaperture array for array period 1000nm – 800nm.

A particularly interesting phenomenon with nanoaperture arrays is that they show multiple transmission peaks. The transmission cutoff wavelength of cylindrical nanoapertures is not affected by the corrugations. Thus, the transmission that is seen with nanoaperture arrays arises from the array itself and its ability to excite surface plasmons. For a two-dimensional nanoaperture array to excite surface plasmons, the same principle of momentum matching of incident photons to that of surface plasmons applies. In the case of a two-dimensional grating, the expression for momentum can be written as

$$k_x = k_o \sin(\theta) \pm iG_x + jG_y \tag{1.8}$$

where G_x and G_y represent the reciprocal lattice vectors,($\frac{2\pi}{p}$ in the *x* and *y* direction on the nanoaperture array), and the mode indices *i* and *j* are integers which influence both the magnitude and direction of the lattice vectors *G*. By combining Eq. 1.8 with Eq. 1.1 one can approximate, for a square array, the wavelength of maximum transmission for a given mode *i,j* as[4]

$$\lambda_{SPP}(i,j) = \frac{p}{(i^2 + j^2)}\left(\frac{\varepsilon_1 \varepsilon_2}{\varepsilon_1 + \varepsilon_2}\right) \tag{1.9}$$

Based on this relationship it is possible to understand the influence of the nanoaperture array on the transmission process. The experimental transmission spectrum shown in fig 1.7, was measured for d = 400nm holes with the array period ranging from 800nm to 1000nm in a 150nm thick Au film. It is evident from the spectrum that two resonances are present, which correspond to the excitation of surface plasmons at the Au/SiO_2 interface.

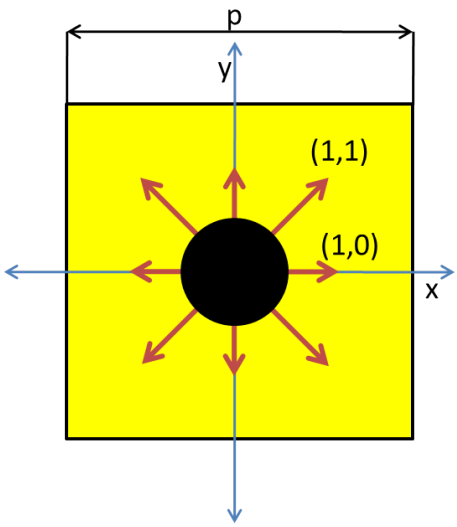

Figure 1.8. A unit cell of the square lattice structure of a nanoaperture array with direction of fundamental plasmonic Bloch modes (SPP-Bloch modes) excited by the array structure.

As seen the figure 1.7, the actual transmission of a cylindrical nanoaperture array is low. However, taking account for the total area illuminated relative to the total open area presented by the nanoapertures, for certain modes the transmission actually exceeds unity; i.e. the light being transmitted through the hole exceeds the theoretical maximum. This effect has been termed 'Extraordinary optical transmission" (EOT), and it implies that the areas of the nanoaperture array aside from the nanoapertures themselves are playing a role in the EOT process. It is

believed that this arises from surface plasmons that are excited by the grating structure of the nanoaperture array. SPPs excited over the array form standing periodic surface waves[15] which repeat in multiples of the total number of apertures that make the full array. The direction and degeneracy are functions of the lattice symmetry, which for a square two-dimensional lattice can be reduced into two fundamental modes in the ±(1,1) and ±(1,0) directions(fig 1.8). These modes have unique values for the wavevector k_x that arise from the structure of the lattice, and thus the value $\lambda_{SPP}(i,j)$ will be unique for each mode, which is evident in the transmission spectra(fig 1.7).

1.5 EXTRAORDINARY OPTICAL TRANSMISSION WITH ANNULAR APERTURE ARRAYS

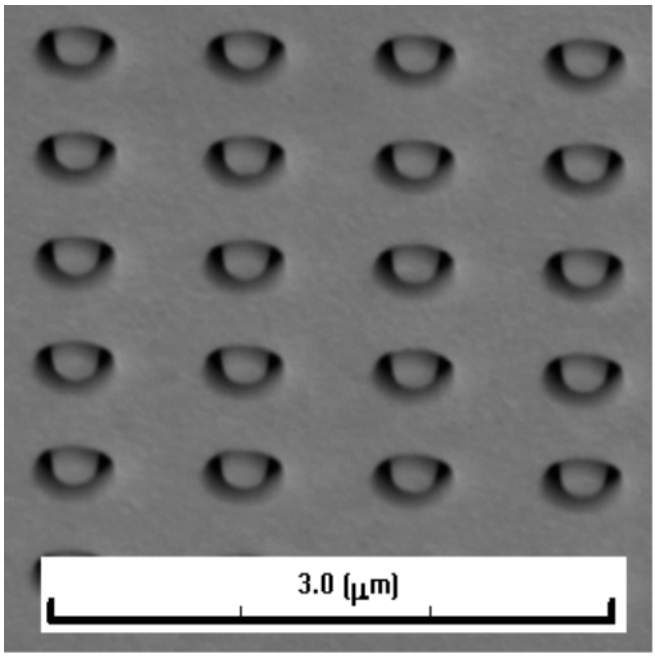

Figure 1.9. SEM image of an annular aperture array with R1 = 125 R2 = 215 and P = 800nm. Taken with the sampled tilted 55^{o} relative to the SEM column.

In contrast to cylindrical hole arrays, coaxial (or annular aperture arrays (AAA)), contain a metallic island within the cylindrical nanoaperture so that a ring with a <100nm width is created (fig 1.9). It was first predicted by Baida *et al*[16] that these structures would be capable of supporting coaxial TE_{11} waveguide modes, and it was later demonstrated that structures in a two dimensional square array exhibit excellent transmission,[14, 17-19] approaching 90%[20] under the right geometric configuration. Haftel *et al*[21, 22] proposed that the enhanced transmission arises from the excitation of cylindrical surface plasmons(CSP) at the edges of the coaxial structure on

both the inner and outer ring. It also was suggested that, owing to the periodic nature of the AAA, surface plasmons could be excited and thus affect the transmission[23]. Most recently it was suggested that the mechanism for EOT in AAAs does not solely arise from a waveguide resonance within the individual aperture, but also from array-induced surface plasmons being in resonance with the coaxial TE_{11} waveguide mode[22].

Until recently, no experimental studies of AAAs addressed the role of the array periodicity in the transmission. We found that for AAAs fabricated with different array period, a noticeable change in the transmission was observed (Fig 1.10). Surprisingly, the transmission spectra show only a single peak, whereas a two-dimensional nanoaperture array (figure 1.7) has multiple transmission peaks that correspond to the grating based surface plasmon modes thought to play a role in the EOT process. The change in the observed transmission with different array period along with the lack of multiple transmission modes raises several questions about the nature of AAAs which will be discussed in chapter 2.

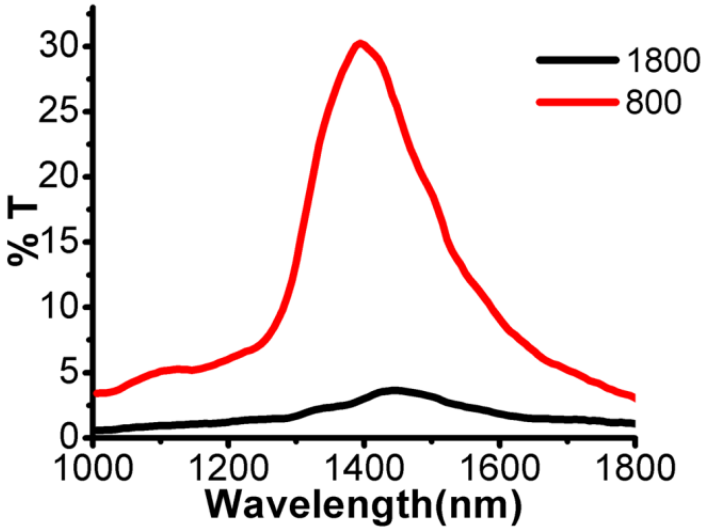

Figure 1.10. Transmission spectra are shown for two AAAs R1 = 125nm, R2 = 215nm, P = 2000nm (black line), and P = 600nm (red line).

1.6 LOCALIZED SURFACE PLASMON RESONANCE

Non-propagating surface plasmons are known as localized surface plasmons and exist within surface features in nanostructured films or more commonly on nanoparticles with dimensions much less than the wavelength of the light with which they interact. A basic understanding of how localized surface plasmon resonance (LSPR) is excited and its physical consequences can be explained through a system consisting of a subwavelength metallic sphere in a uniform dielectric medium. Light incident upon a metallic sphere at its LSPR will induce coherent oscillation of the free electron gas that is confined to the nanoparticle (figure 1.11). The oscillation is induced by displacement of the electrons by the incident electromagnetic field of light. The displaced electrons within the nanoparticle create opposed regions of net positive and negative charge, which results in a restoring force that is able to drive the oscillation.

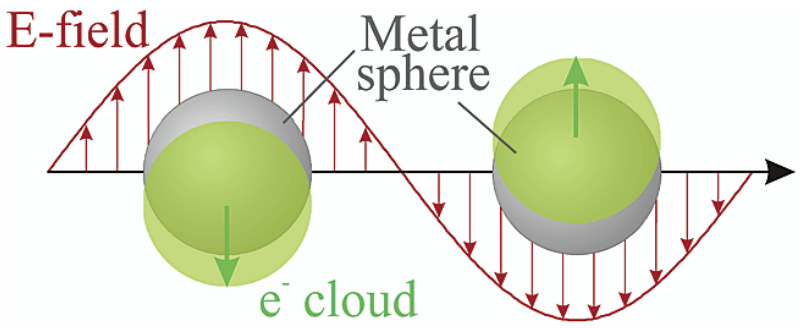

Figure 1.11. Cartoon depiction of free electron displacement upon a subwavelength metallic sphere by incident electromagnetic radiation at wavelengths corresponding to the localized surface plasmon resonance. Adapted from ref. 24.

The nanoparticle dipole, P, induced by the charge separation on a spherical nanoparticle in the quasistatic limit can be expressed as[24]:

$$P = \alpha E_o \tag{1.10}$$

where α is the polarizability and E_o is the magnitude of the static electric field from the incident light. The wavelength dependent polarizability can be defined as[25]:

$$\alpha(\lambda) = 4\pi a^3 \frac{\varepsilon_m(\lambda) - \varepsilon_d}{\varepsilon_m(\lambda) + 2\varepsilon_d} \tag{1.11}$$

where a is the radius of the sphere, ε_m is the wavelength dependent dielectric function of the metal, and ε_d is the dielectric constant of the surrounding dielectric medium. At wavelengths where $\varepsilon_m = -2\varepsilon_d$ the polarizability is at a maximum and the fields around the nanoparticle are enhanced relative to the incident electromagnetic field. The combined absorption and scattering of incident light at the LSPR by a nanoparticle can be expressed as[26]:

$$E(\lambda) = \frac{24\pi^2 N a^3 {\varepsilon_d}^{3/2}}{\lambda \ln(10)} \left[\frac{\varepsilon_m(\lambda)}{(\varepsilon_m(\lambda) + \gamma\varepsilon_d)^2 + i\varepsilon_m(\lambda)^2} \right] \tag{1.12}$$

where γ is a geometric factor taken as 2 for a sphere but can vary for different aspect ratio nanoparticles. N is the sum of finite polarizable elements on the nanoparticle and is typically quantified through the discrete dipole approximation or finite difference time domain methods. These relationships indicate that the resonance of the nanoparticle is sensitive to the surrounding medium and the electromagnetic fields are enhanced at the resonance. These features of LSPR on nanoparticles have been exploited in numerous ways to develop systems and devices for applications including biosensing[27-29], bioimaging & cancer therapy[30-32], chemical sensing[33], surface enhanced spectroscopies[34-37], and optoelectronics[38]. Of particular interest to this dissertation is the interaction of nanoparticles fixed upon a flat substrate in a periodic configuration. These nanoparticle arrays have several interesting optical features which have been found to have a significant influence upon the EOT in nanoapertures arrays.

1.6.1 Plasmonic Nanoparticle Arrays

Two dimensional arrays of subwavelength nanoparticles have received much attention since Van Duyne and coworkers demonstrated the robust ability of these structures for both biosensing[28] and SERS[39]. For their experiments, nanoparticle arrays were fabricated by nanosphere lithography[40] in which the nanoparticles were formed within the gaps created by hexagonally packed polystyrene nanospheres (<500nm diameter) fixed on a transparent substrate. These served as deposition masks for triangular nanoparticles with geometries ranging from 20 – 100nm. Plasmonic nanoparticle arrays are also fabricated through standard nanofabrication methods such as electron beam lithography using a positive resist to form a mask for the physical vapor deposition of a metal to form nanoparticles.

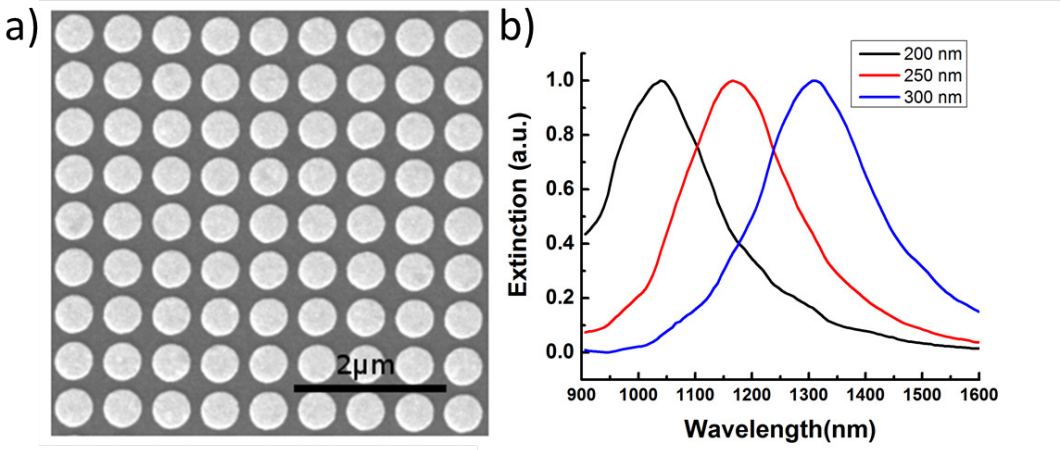

Figure 1.12. Panel a) shows a SEM image of an Ebeam lithography fabricated Au nanoparticle array and b) shows optical extinction spectra for Au nanodisk arrays showing spectral redshift with increasing nanodisk diameter.

A typical nanoparticle array will consist of periodic nanoparticles on a transparent substrate that normally are arranged in a square or hexagonal array[41] (figure 1.12 a)). The type of metal used, as well as the size and shape of the nanoparticle, dictates the wavelength of the

LSPR for the array. As seen in figure 1.12 b), the LSPR wavelength is tied to the diameter of the nanoparticle, which allows a degree of tunability in the optical response of the array. Other factors related to the spacing of the nanoparticles within the array as well as the optical effects induced by placing nanoparticles within the proximity of their respective near-field will be discussed in subsequent sections.

1.6.2 Nanoparticle Array Diffractive Coupling

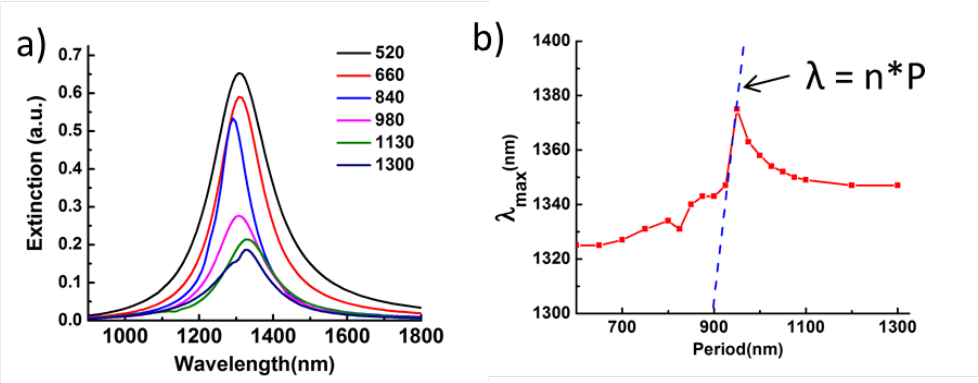

Figure 1.13. a) Optical extinction of an Au nanodisk array at different array period and b) plot of the point of maximum extinction, λ_{max}, at different period (red line) overlaid with the light line ($\lambda = n*P$, dashed blue line) for the substrate diffractive mode.

Nanoparticle arrays exhibit unusual optical behavior with incremental variation in the array period. Unlike nanoapertures arrays that show a correlated monotonic change in transmission wavelength as a function of period, nanoparticle arrays tend to have a more complex response. Initially reported by Lamprecht and coworkers[42] and later further explored upon by Haynes and coworkers[41], it was shown that two dimensional nanoparticle arrays exhibit a redshift or blueshift in the optical response with incremental change in the array period. Additionally, the shape of the LSPR curve becomes asymmetric for array periods where the redshift to blueshift transition

was observed. As seen in figure 1.13 a), as the period of the grating is increased from 520nm to 1300nm, noticeable changes occur in the direction of the wavelength shift as well as the magnitude, bandwidth, and shape of the peak. All of these can be attributed to interactions with the nanoparticle LSPR and diffractive modes induced by the periodicity of the grating. These dependences are illustrated in figure 1.13 b), which plots the wavelength shift on the y-axis vs. grating period on the x-axis. The red-shift of the LSPR with an increase in the array period is believed to be due to constructive interference between the LSPR and diffractive modes, while blue-shifts are attributed to destructive interference. Studies have shown that this effect can be exploited to generate ultrasharp diffractive resonances in two-dimensional nanoparticle arrays.

1.6.3 Nanoparticle Near-field Coupling

Plasmonic nanoparticles in solution and as arrays exhibit several nonlinear phenomena when the distance between adjacent nanoparticles is within the near-field generated by the LSPR. At these close distances the dipolar nanoparticle resonances become coupled and the magnitude of the electromagnetic field between the nanoparticles is amplified by orders of magnitude. The degree of this amplification is sensitive to the spacing between the nanoparticles and an exponential decrease in the field magnitude as a function of nanoparticle separation is observed. This phenomenon is thought to be one of the primary physical processes responsible for generating the signal amplification seen in SERS spectroscopy. As a consequence of the resonances between adjacent nanoparticles becoming coupled, the resonance frequency decreases which is observed as a red-shift in the optical response of the system. Because of their non-linear nature and their potential applications, numerous studies have been conducted for nanoparticles in solution and as arrays to better understand this process.

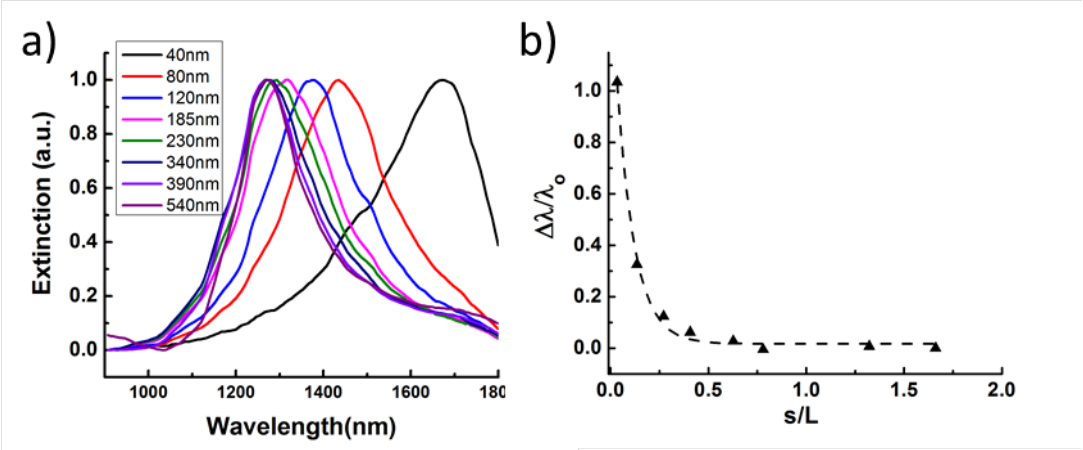

Figure 1.14. a) Optical response of an Au nanoparticle array at different nanoparticle separation and b) plot of the fractional wavelength shift of λ_{max} against the nanoparticle separation normalized to the diameter of the disk.

For nanoparticle pairs or arrays on a substrate, this process was first observed and characterized by Rechiberger and coworkers[43], who observed that, for EBL fabricated nanodisk pairs, the optical response red-shifted as the spacing between the nanodisks was reduced. The magnitude of the red-shift as a function of nanoparticle separation was found to be exponential in nature with the largest shifts occurring for the smallest nanoparticle separations (Figure 1.14 a). A thorough analysis of the optical response of nanoparticle pairs of different geometry by Jain and coworkers[44] established the universal behavior of this process. They found that when the fractional wavelength shift was compared to the ratio between nanodisk separation and diameter, the exponential behavior of the red-shift was retained regardless of the nanodisk size. They were able to propose a universal relationship for the plasmon ruler behavior as

$$\frac{\Delta\lambda}{\lambda} \approx 0.18\exp\left(\frac{-\left(\frac{s}{D}\right)}{0.23}\right) \qquad (1.12)$$

where $\Delta\lambda$ represents the change in λ_{max} as the separation is decreased, s is the separation between the adjacent nanoparticles, and D is the nanoparticle diameter(Figure 1.14 b).

1.7 SURFACTANT MEDIATED SYNTHESIS OF GOLD NANOPARTICLES

Since the discovery by Yu and coworkers[45], who successfully synthesized rod-like Au nanoparticles via electrodeposition in the presence of cationic surfactants, a large body of work has been dedicated to both understanding the mechanism behind anisotropic particle growth and to synthesizing novel structures through changes in the solution conditions during synthesis[46, 47]. These efforts have resulted in methods that allow for anisotropic particles to be synthesized with good size control and yield.

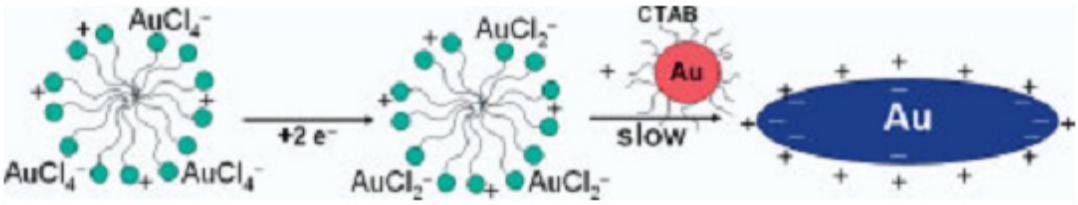

Figure 1.15: Depiction of CTAB mediated anisotropic particle growth. $\mathbf{AuCl_4^-}$ bound to CTAB micelles is reduced to $\mathbf{AuCl_2^-}$ and interactions with Au seeds initiate anisotropic nanoparticle nucleation and growth. Figure taken from ref. 47.

The cationic surfactant commonly used is cetyltrimethylammonium bromide (CTAB), which consists of a quaternary amine head group with a 14 carbon hydrophobic chain. Typically CTAB concentration is above the critical micelle concentration and the surfactant predominantly exists as micelles. The quaternary amine is stabilized by a halogen counter ion, normally

bromide or chloride and studies have indicated that the halogen counter ion can have significant influence on the shape directing properties of the surfactant. Upon addition of $HAuCl_4$ to a solution of CTAB, $AuCl_4^-$ ions bind to the CTAB micelles (Figure 1.15), addition of the reducing agent ascorbic acid converts the $AuCl_4^-$ to $AuCl_2^-$. In the absence of CTAB, addition of ascorbic acid leads to the immediate formation of Au nanoparticles; however in the presence of CTAB no nanoparticle nucleation and growth occurs because of the exceptionally strong interaction between CTAB and $AuCl_2^-$. To initiate nanoparticle growth small Au seeds have to be added to the solution.

1.7.1 Shape directing Effects of Ions in Au Nanoparticle Synthesis

Initial work with Au nanorod synthesis by Murphy and coworkers[45, 48-50] found that addition of a small amount of $AgNO_3$ to the growth solution leads to a significant increase in the yield and narrowing of the size distribution for Au nanorods. It was initially thought that AgBr formed in solution by addition of $AgNO_3$ would bind to the surface of the growing nanorod and inhibit growth to specific facets on the growing nanoparticle. Liu and coworkers[51] proposed that underpotential deposition (UPD) of Ag^+ during nanoparticle growth is the primary mechanism behind the shape directing role of Ag. UPD is the process by which metal adlayers form on another metal at potentials significantly more positive than their Nernst potential. The presence of UPD Ag on various crystal facets of the growing nanorod serves to retard growth depending on the location of the Ag adlayer. Ag UPD has also been utilized to make a variety of anisotropic nanoparticles with bipyramidal type features or high index faceted nanoparticles in addition to nanorods[49, 50].

Halide ions have displayed shape directing effects in Au nanoparticle synthesis, also. First proposed by Ha and coworkers[52], and later expanded upon by Millstone and coworkers[53], iodide is capable of directing the shape of Au nanoparticles at various concentrations. Iodide is believed to bind to Au<111> facets with high affinity, retarding growth along that facet. This effect has been exploited in the synthesis of both Au nanorods and nanoprisms, which depending on the iodide concentration, will be the primary product of the reaction.

1.8 FABRICATION METHODOLOGIES

1.8.1 Nanoaperture Arrays

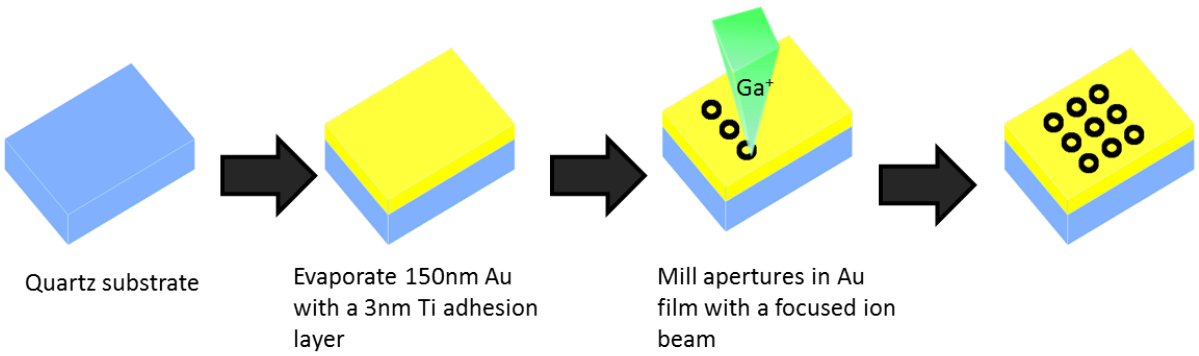

Figure 1.16. Process flow for nanoaperture array device fabrication

The basic sequence for device fabrication is outlined in figure 1.16. Initially a quartz microscope slide is cleaned with a piranha solution (3:1 H_2SO_4/H_2O_2) at 80°C for at least 10 minutes in order to remove any organic residue. Following piranha cleaning the substrate is rinsed thoroughly with deionized water. Cleaned substrates are then placed into an e-beam evaporator

(Thermionics VE-180) and Au is evaporated thermally at a pressure of $<10^{-5}$ Torr. A very thin (1-3nm) Ti layer is evaporated first to enhance the adhesion of the Au to the quartz surface. Following thin film evaporation, nanoapertures are milled with a focused ion beam system (Seiko 3050SE) at 30kV accelerating voltage with 30pA of current. For a typical nanoaperture array, sets of 20 x 20 apertures are fabricated. For transmission measurements, a reference window is milled into the same Au film that contains the nanoaperture arrays. Normal beam conditions for the reference window are 30kV and 3nA.

1.8.2 Colloidal Lithography

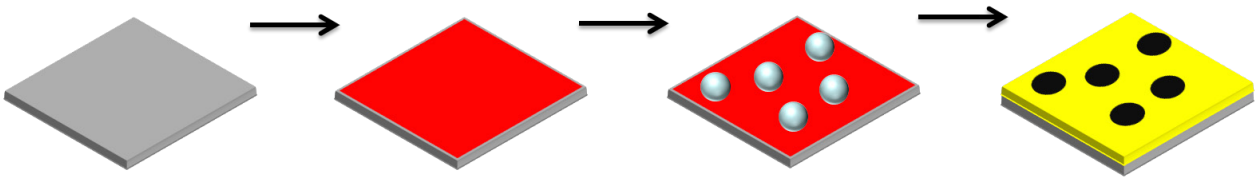

Figure 1.17. Process flow for colloidal lithography to produce randomly oriented nanoapertures in a thin Au film

Initially introduced by Van Duyne and coworkers[40], colloidal nanosphere lithography is a very versatile tool for fabricating nanostructures arranged as both arrays or randomly on any substrate. For this work, randomly oriented nanoapertures were fabricated on glass microscope slides in a manner similar to Mirin and coworkers[54]. Piranha cleaned microscope slides were immersed in a dilute solution of the cationic polymer polydiallyldimethylammonium chloride (PDDA) briefly to form a thin layer of the polymer on the glass surface. The positively charged surface from the adsorption of the polymer enables the binding of negatively charged polystyrene-sulfate or silica

microspheres via electrostatic interactions. Once the nanospheres are attached to the glass substrate Au is thermally evaporated. The nanospheres act as a negative mask for nanoapertures. Removal of the nanospheres is accomplished by ultrasonication or tape. This process results in randomly oriented nanoapertures in a thin Au film on a transparent glass substrate.

1.8.3 Alkanethiol Self-assembled Monolayers

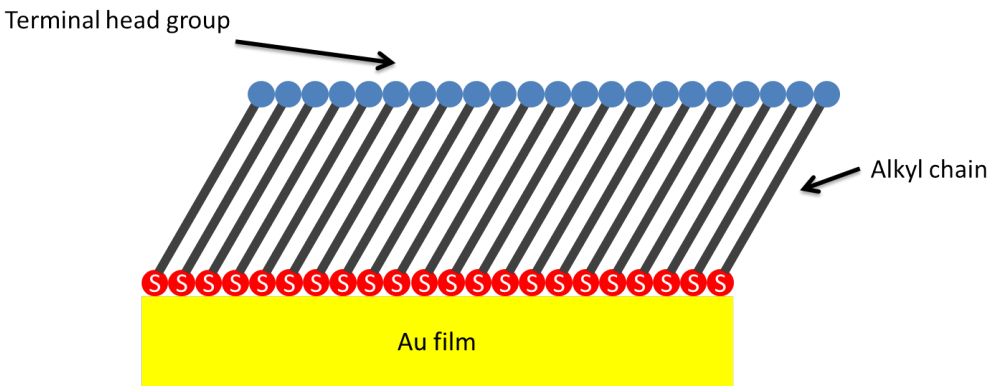

Figure 1.18. Cartoon of an alkanethiol self-assembled monolayer on a gold film

Self-assembly is a fundamental process in nature that enables molecules to spontaneously form complex structures that exhibit novel physical properties. Chemisorption of molecules onto surfaces via self-assembly has been a subject of general research interest owing to the ability of chemisorbed molecules to change the physical properties of the surfaces to which they attach. Chemisorption via self-assembly is an especially useful process because it proceeds spontaneously and under amenable conditions. Self-assembly of small molecules has been found to occur on a variety of surfaces such as metal oxides[55], semiconductors[56], and noble metals[57]. Self-assembly of alkanethiols onto metal films has been studied extensively and shown to have numerous applications in fundamental research and nanotechnology[58].

Alkanethiols are known to form well packed, stable, self-assembled monolayers on Au films[59, 60] (figure 1.18) from solution at mM concentration and the process has been found to follow a two-step mechanism[61]. The initial step involves the random chemisorption of the molecules onto the film, driven by the strong interaction between Au and the sulfur on the thiol group of the adsorbed molecule. This process is rapid and generally follows Langmuir isotherm kinetics. The second step involves organization of the adsorbed molecules into a semi-crystalline film mediated by the favorable van der Waals and dipole-dipole interactions that promote close packing of the alkyl chains. Thus for longer alkyl chains the interactions are more favorable and the resultant films have better organization and stability[62, 63]. The total time required to finish self-assembly is determined by the alkyl chain length as well as the terminal functional group.

1.9 OVERVIEW OF MAJOR FINDINGS

This first part of this dissertation explores the extraordinary optical transmission phenomena in both annular apertures and nested nanoparticle / nanoslit arrays. Chapter 2 introduces annular aperture arrays and explores the relationship between the observed transmission of the device and the array period. The relationship between the array period and the transmission reveal the role of surface plasmon polariton modes in enhancing the transmission. To support this conclusion the symmetry in the array was broken by changing the periodicity along only one axis while recording the polarization dependent transmission. This experiment provided the evidence necessary to conclude that SPPs excited because of the periodicity of the array were essential to the enhanced transmission. Chapter 3 further extends the knowledge about transmission in AAAs by exploring the relationship between the geometry of the aperture and the transmission. Through these studies it was shown that the geometry of the central disk within the aperture can dictate the location of maximum transmission. These results show that the LSPR modes excited on the central disk of the annulus are important to the EOT process. Moreover, it was demonstrated that diffractive coupling effects seen in nanoparticle arrays can be reproduced with AAAs because of the LSPR excited upon the annulus. These studies suggest that EOT can be significantly influenced by LSPR modes present within the device.

Nanoparticle nanoslit arrays (Chapter 4), inspired by the significant role of LSPR modes in AAA transmission, demonstrated for the first time a nanoaperture device in which the EOT was modulated exclusively by the LSPR based interactions. These devices consisted of nanoslits with nested nanoparticle arrays. The nanoslit was designed in such a fashion that incident light polarized along the long-axis of the array would show minimal transmission, that is any observed transmission would be caused by LSPRs excited upon the nanoparticles within the slit. To prove

that the transmission was in fact LSPR mediated, experiments were carried out to demonstrate the geometric dependence of the nanoparticle on the transmission, which demonstrated the tunability of the device through the LSPR. Also, both diffractive and near-field coupling between the nanoparticles was shown to have a significant impact on the optical response of the device in a manner analogous to two-dimensional nanoparticle arrays.

The last part of the dissertation covers recent work aimed towards using chemical methods to fabricate annular aperture type devices with greater precision than is currently possible via standard nanofabrication procedures. Surprisingly, a novel method to functionalize Au nanostructures with CTAB mediated anisotropic synthetic methods was discovered. It was found that forming a hydrophobic self-assembled monolayer on an Au film with randomly oriented nanoapertures and then carrying out CTAB/Au nanoparticle synthesis results in the seedless growth of arbitrary structures within the nanoapertures. It is believed that the nanoapertures acted as a soft template that provides the symmetry breaking conditions required for the nanoparticle growth. Studies into the mechanism behind nanoparticle nucleation and growth reveal that the length of the alkanethiol chain is critical for successful nucleation and growth, which implies that interactions between the hydrophobic tail of the CTAB surfactant and the alkanethiol SAM are important in driving the nanoparticle growth. Introduction of shape directing ions (Ag or I) or changing the terminal head group on the alkanethiol SAM has a profound influence on the morphology, shape, and arrangement of nanoparticles within the nanoapertures. This methodology is also extended to Au nanoparticles immobilized on a transparent substrate to generate novel heteroaggregates both of Au/Au and Ag/Au. These studies demonstrate a novel and seedless approach to functionalize both nanoapertures and nanoparticles with sub-5nm gaps and novel nanoparticle structures. These findings should have

significant implications towards developing a more comprehensive understanding of both the nucleation and growth process of anisotropic nanoparticles as well as the development of novel plasmonic structures.

1.10 REFERENCES

1. T. W. Ebbesen, H. J. Lezec, H. F. Ghaemi, T. Thio and P. A. Wolff, Nature **391** (6668), 667-669 (1998).
2. H. A. Bethe, Phys. Rev. **66**, 163-182 (1944).
3. H. Raether, (1988).
4. H. F. Ghaemi, T. Thio, D. E. Grupp, T. W. Ebbesen and H. J. Lezec, Physical Review B **58** (11), 6779-6782 (1998).
5. A. G. Brolo, R. Gordon, B. Leathem and K. L. Kavanagh, Langmuir **20** (12), 4813-4815 (2004).
6. T. Nikolajsen, K. Leosson and S. I. Bozhevolnyi, Applied Physics Letters **85** (24), 5833-5835 (2004).
7. K. Tanaka, M. Tanaka and T. Sugiyama, Opt. Express **13** (1), 256-266 (2005).
8. T. W. Ebbesen, C. Genet and S. I. Bozhevolnyi, Physics Today **61** (5), 44-50 (2008).
9. P. Drude, Ann. Phys **1**, 566-613 (1900).
10. P. B. Johnson and R. W. Christy, Physical Review B **6** (12), 4370-4379 (1972).
11. E. Kretschmann and H. Raether, Z. Naturforsch. A **23**, 2135 (1968).
12. J. Homola, S. S. Yee and G. Gauglitz, Sensors and Actuators B: Chemical **54** (1–2), 3-15 (1999).

13. C. Kittel, *Introduction to solid state physics*. (Wiley, New York, 1996).

14. F. I. Baida, D. Van Labeke, G. Granet, A. Moreau and A. Belkhir, Applied Physics B: Lasers and Optics **79** (1), 1-8 (2004).

15. E. Altewischer, M. P. van Exter and J. P. Woerdman, J. Opt. Soc. Am. B **20** (9), 1927-1931 (2003).

16. F. I. Baida and D. Van Labeke, Optics Communications **209** (1–3), 17-22 (2002).

17. F. I. Baida and D. Van Labeke, Physical Review B **67** (15), 155314 (2003).

18. F. I. Baida, D. Van Labeke and B. Guizal, Appl. Opt. **42** (34), 6811-6815 (2003).

19. J. Salvi, M. Roussey, F. I. Baida, M. P. Bernal, A. Mussot, T. Sylvestre, H. Maillotte, D. Van Labeke, A. Perentes, I. Utke, C. Sandu, P. Hoffmann and B. Dwir, Opt. Lett. **30** (13), 1611-1613 (2005).

20. Y. Poujet, J. Salvi and F. I. Baida, Opt. Lett. **32** (20), 2942-2944 (2007).

21. M. I. Haftel, C. Schlockermann and G. Blumberg, Applied Physics Letters **88** (19), 193104-193103 (2006).

22. S. M. Orbons and A. Roberts, Opt. Express **14** (26), 12623-12628 (2006).

23. W. Fan, S. Zhang, B. Minhas, K. J. Malloy and S. R. J. Brueck, Physical Review Letters **94** (3), 033902 (2005).

24. K. L. Kelly, E. Coronado, L. L. Zhao and G. C. Schatz, The Journal of Physical Chemistry B **107** (3), 668-677 (2002).

25. S. A. Maier, *Plasmonics: Fundamentals and Applications*. (2007).

26. K. A. Willets and R. P. Van Duyne, Annual Review of Physical Chemistry **58** (1), 267-297 (2007).

27. K.-S. Lee and M. A. El-Sayed, The Journal of Physical Chemistry B **110** (39), 19220-19225 (2006).

28. A. J. Haes and R. P. Van Duyne, Journal of the American Chemical Society **124** (35), 10596-10604 (2002).

29. A. D. McFarland and R. P. Van Duyne, Nano Letters **3** (8), 1057-1062 (2003).

30. E. B. Dickerson, E. C. Dreaden, X. Huang, I. H. El-Sayed, H. Chu, S. Pushpanketh, J. F. McDonald and M. A. El-Sayed, Cancer Letters **269** (1), 57-66 (2008).

31. X. Huang, I. H. El-Sayed, W. Qian and M. A. El-Sayed, Journal of the American Chemical Society **128** (6), 2115-2120 (2006).

32. A. M. Gobin, M. H. Lee, N. J. Halas, W. D. James, R. A. Drezek and J. L. West, Nano Letters **7** (7), 1929-1934 (2007).

33. C. Li, C. Wu, J. Zheng, J. Lai, C. Zhang and Y. Zhao, Langmuir **26** (11), 9130-9135 (2010).

34. K. L. Wustholz, A.-I. Henry, J. M. McMahon, R. G. Freeman, N. Valley, M. E. Piotti, M. J. Natan, G. C. Schatz and R. P. V. Duyne, Journal of the American Chemical Society **132** (31), 10903-10910 (2010).

35. Y. Chen, K. Munechika and D. S. Ginger, Nano Letters **7** (3), 690-696 (2007).

36. C. E. Talley, J. B. Jackson, C. Oubre, N. K. Grady, C. W. Hollars, S. M. Lane, T. R. Huser, P. Nordlander and N. J. Halas, Nano Letters **5** (8), 1569-1574 (2005).

37. S. Nie and S. R. Emory, Science **275** (5303), 1102-1106 (1997).

38. M. W. Knight, H. Sobhani, P. Nordlander and N. J. Halas, Science **332** (6030), 702-704 (2011).

39. A. D. McFarland, M. A. Young, J. A. Dieringer and R. P. Van Duyne, The Journal of Physical Chemistry B **109** (22), 11279-11285 (2005).

40. J. C. Hulteen and R. P. Van Duyne, Journal of Vacuum Science & Technology A: Vacuum, Surfaces, and Films **13** (3), 1553-1558 (1995).

41. C. L. Haynes, A. D. McFarland, L. Zhao, R. P. Van Duyne, G. C. Schatz, L. Gunnarsson, J. Prikulis, B. Kasemo and M. Käll, The Journal of Physical Chemistry B **107** (30), 7337-7342 (2003).

42. B. Lamprecht, G. Schider, R. T. Lechner, H. Ditlbacher, J. R. Krenn, A. Leitner and F. R. Aussenegg, Physical Review Letters **84** (20), 4721-4724 (2000).

43. W. Rechberger, A. Hohenau, A. Leitner, J. R. Krenn, B. Lamprecht and F. R. Aussenegg, Optics Communications **220** (1–3), 137-141 (2003).

44. P. K. Jain, W. Huang and M. A. El-Sayed, Nano Letters **7** (7), 2080-2088 (2007).

45. Yu, S.-S. Chang, C.-L. Lee and C. R. C. Wang, The Journal of Physical Chemistry B **101** (34), 6661-6664 (1997).

46. M. Grzelczak, J. Perez-Juste, P. Mulvaney and L. M. Liz-Marzan, Chemical Society Reviews **37** (9), 1783-1791 (2008).

47. J. Pérez-Juste, L. M. Liz-Marzán, S. Carnie, D. Y. C. Chan and P. Mulvaney, Advanced Functional Materials **14** (6), 571-579 (2004).

48. N. R. Jana, L. Gearheart and C. J. Murphy, The Journal of Physical Chemistry B **105** (19), 4065-4067 (2001).

49. A. Gole and C. J. Murphy, Chemistry of Materials **16** (19), 3633-3640 (2004).

50. T. K. Sau and C. J. Murphy, Langmuir **20** (15), 6414-6420 (2004).

51. Liu and P. Guyot-Sionnest, The Journal of Physical Chemistry B **109** (47), 22192-22200 (2005).

52. T. H. Ha, H.-J. Koo and B. H. Chung, The Journal of Physical Chemistry C **111** (3), 1123-1130 (2006).

53. J. E. Millstone, W. Wei, M. R. Jones, H. Yoo and C. A. Mirkin, Nano Letters **8** (8), 2526-2529 (2008).

54. N. A. Mirin, M. Hainey and N. J. Halas, Advanced Materials **20** (3), 535-538 (2008).

55. M. Dubey, T. Weidner, L. J. Gamble and D. G. Castner, Langmuir **26** (18), 14747-14754 (2010).

56. P. Thissen, M. Valtiner and G. Grundmeier, Langmuir **26** (1), 156-164 (2009).

57. H. Rieley, G. K. Kendall, R. G. Jones and D. P. Woodruff, Langmuir **15** (26), 8856-8866 (1999).

58. J. C. Love, L. A. Estroff, J. K. Kriebel, R. G. Nuzzo and G. M. Whitesides, Chemical Reviews **105** (4), 1103-1170 (2005).

59. R. G. Nuzzo and D. L. Allara, Journal of the American Chemical Society **105** (13), 4481-4483 (1983).

60. C. D. Bain, E. B. Troughton, Y. T. Tao, J. Evall, G. M. Whitesides and R. G. Nuzzo, Journal of the American Chemical Society **111** (1), 321-335 (1989).

61. A. Ulman, Chemical Reviews **96** (4), 1533-1554 (1996).

62. R. G. Nuzzo, E. M. Korenic and L. H. Dubois, The Journal of Chemical Physics **93** (1), 767-773 (1990).

63. L. H. Dubois, B. R. Zegarski and R. G. Nuzzo, Journal of the American Chemical Society **112** (2), 570-579 (1990).

2.0 THE EFFECT OF PERIODICITY ON THE EXTRAORDINARY OPTICAL TRANSMISSION OF ANNULAR APERTURE ARRAYS

This work has been published as Matthew J. Kofke, David H. Waldeck, Zahra Fakhraai, Shell Ip, and Gilbert C. Walker, *Appl. Phys. Lett*. 94, 023104 (2009). The thesis author fabricated structures,collected and analyzed experimental data, and wrote the manuscript. Dr. Zahra Fakhraai conducted FDTD simulations of the experimental systems studied.

2.1 INTRODUCTION

This work systematically evaluates the effect of array periodicity on the near infrared (NIR) transmission characteristics of annular aperture arrays (AAA) in gold films. Both the experimental spectra and the FDTD simulated transmission spectra of AAAs are shown to be sensitive to the period and the arrangement of the apertures within the array. The spectra of square arrays with periods ranging from 1400nm – 600nm show a strong correlation with SPP-Bloch modes of the metal/dielectric interfaces. For rectangular AAAs the transmission spectra are significantly attenuated and reveal a polarization sensitivity that arises from the breaking of the symmetry and degeneracy of the SPP-Bloch modes. These findings show that the

metal/substrate interface contributes significantly to the extraordinary optical transmission of the AAAs.

Nanoscale metal structures have generated considerable interest since Ebbesen *et al*[1] demonstrated that an array of subwavelength holes transmits more light than predicted by the classical diffraction theory[2] and correlated the extraordinary optical transmission (EOT) with the resonant excitation of surface plasmons[3] that arise from the periodic nature of the arrays.[4] On a fundamental level, this discovery has sparked interest in the basic process underlying the ability of a nanoaperture to tunnel light with high efficiency and the physics of surface plasmons. On an applied level this work has encouraged researchers to explore the potential of creating nanoscale sensors,[5] communication devices,[6] optical circuits,[7] and other devices from such arrays.

In contrast with cylindrical hole arrays, coaxial, or annular aperture arrays (AAAs), contain a metallic island within the cylindrical nanoaperture so that a ring with a <100 nm gap is created (see Fig. 2.1). It was first predicted by Baida and van Labeke[8] that these structures would be capable of supporting coaxial TE_{11} waveguide modes, and it was later demonstrated that structures in a two dimensional square array exhibit excellent transmission,[8-12] approaching 90%[13] under the right geometric configuration. Orbons and Roberts[14] and Haftel *et al*[15] proposed that the enhanced transmission arises from the excitation of cylindrical surface plasmons at the edges of the coaxial structure on both the inner and outer rings. It also was suggested that, owing to the periodic nature of the AAA, surface plasmons could be excited and thus affect the transmission.[16] Most recently it was suggested that the mechanism for EOT in AAAs does not solely arise from a waveguide resonance within the individual aperture but also from array-induced surface plasmons being in resonance with the waveguide mode.[17] This study extends recent work on AAAs by exploring how surface plasmon polariton (SPP)-Bloch modes excited

by a two dimensional array of annular apertures influence the EOT process. To this end, AAAs in which the array period was systematically varied were fabricated. The experimental transmission spectra are compared with the results of finite difference time domain (FDTD) calculations.

2.2 EXPERIMENTAL METHODS

2.2.1 Device Fabrication and Characterization

Annular aperture arrays were milled into 150nm Au films (with a 1nm Ti adhesion layer) on quartz with a focused ion beam system (Seiko SMI 3050SE). Two series of arrays (Fig. 1) were fabricated with nominally identical annular aperture geometry R1 = 125nm and R2 = 215nm. In the first series, the period was varied between 1400nm and 600nm while keeping the total number of apertures constant at 20 x 20. The second series consisted of arrays with different periodicity along the x and y-axis of the arrays. Along one axis the period was held fixed at 1400nm, and on the other axis the period was varied from 1000nm to 600nm. Zeroth order transmission spectra were collected with a microspectrophotometer (CRAIC QDI 2010) equipped with a 0.13NA 5x objective, a collimated illumination source (Fiber coupled 75W Xe Arc), and a Glan-Taylor polarizer placed directly below the substrate. The reference for the transmission spectra was a 20μm window milled into the same gold film as the arrays. All arrays were spaced at least 150μm apart in order to ensure that they do not couple with one another. Light was incident on the quartz side of the sample and polarized along the x-axis of the AAA.

2.2.2 Theoretical simulations

For a more accurate comparison with the experimental data AAA transmission simulations were done using finite difference time domain (FDTD) technique with Lumerical FDTD software (Lumerical Solutions Inc). For the FDTD simulations the dielectric values for Au and Ti were taken from experimental data[18] and fit within the software. The boundary conditions in the x and y directions were chosen to be anti-symmetric/symmetric and the structure was periodic. The structure was illuminated from the quartz side, and the transmission was calculated at two different heights above the surface (z = 600nm and z = 2000nm) to make sure that the transmission data were consistent. All of the reported values here are from the distance of 2000nm. The illumination source was a plane wave with polarization in the x direction. The simulation was run until the value of the electric field has decayed below 10^{-5} of the original value of the electric field.

2.3 RESULTS AND DISCUSSION

Two series of arrays (Fig. 2.1) were fabricated with nominally identical annular aperture geometry $R1 = 125$ nm and $R2 = 215$ nm. In the first series, the period was varied between 1400 and 600 nm while keeping the total number of apertures constant at 20×20. The second series consisted of arrays with different periodicities along the *x*- and *y*-axes of the arrays. Along one axis the period was held fixed at 1400 nm and on the other axis the period was varied from 1000 to 600 nm.

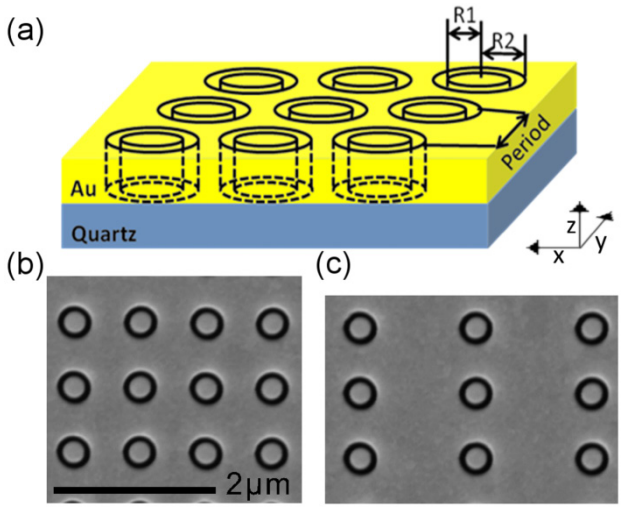

Figure 2.1. (a) Diagram of the system under study: a 150 nm gold film on quartz with annular apertures in an array. Individual annular apertures are defined by the inner radius R1 and the outer radius R2 with a fixed period that represents the spacing between each aperture. (b) SEM of FIB milled AAAs with R1 = 125 nm, R2 = 215 nm and period = 800 nm. (c) SEM of AAAs with period = 1400 nm on the *x*-axis and 800 nm on the *y*-axis.

The wavelength of SPPs excited by Bragg-type scattering over a two dimensional nanoaperture array can be approximately calculated by:

$$\lambda_{SPP}(i,j) = \frac{p}{(i^2 + j^2)}\left(\frac{\varepsilon_d \varepsilon_m}{\varepsilon_d + \varepsilon_m}\right)^{\frac{1}{2}} \tag{2.1}$$

where P is the period of the array, i,j are integers corresponding to Bragg-type scattering modes, ε_d is the dielectric constant for the dielectric, and ε_m is the real component of the complex dielectric function of the metal. Using the above relationship it is possible to estimate λ_{SPP} at a given period. In Eq. (2.1) a Drude model was used for the dielectric function of Au, which is fit to experimental data from 450 to 2000 nm.[19] The dielectric constant of air was taken to be 1.0 and that of the quartz substrate was taken to be 2.10. For a more accurate comparison with the experimental data, AAA transmission simulations were done using the FDTD technique.

2.3.1 Effect of Periodicity for Symmetric AAAs

Figure 2.2 shows the experimental and FDTD simulated transmission spectra of AAAs with periods ranging from 1400 to 600 nm. Panels (a) and (b) show experimental spectra and panels (c) and (d) show simulated spectra. Systematic trends in the transmission spectra as a function of period are evident, namely, the overall transmission increases, the λ_{max} of the dominant resonance blueshifts, and the transmission peak broadens as the period of the array is decreased. These trends correlate with SPP-Bloch modes that are excited by the AAA at the Au/quartz interface. For $R1$ = 125 nm and $R2$ = 215 nm, the cutoff wavelength of the TE_{11} guided mode[11] is 1068 nm, which is significantly to the blue of the main transmission peaks for all periods$P$>700 nm. The simulated transmission spectra in panels (c) and (d) show strong qualitative agreement with the experimental spectra in panels (a) and (b). In particular, the modes

exhibit a similar period dependence on the width of the transmission peak and the wavelength of maximum transmission.

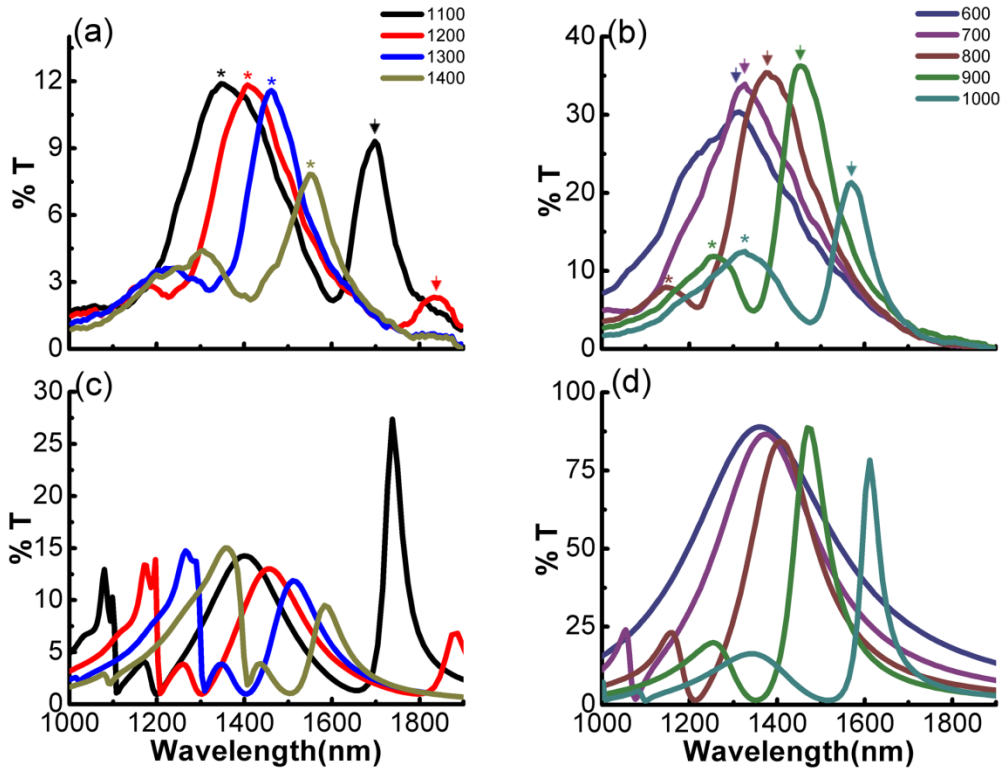

Figure 2.2. Experimental [(a) and (b)] and simulated [(c) and (d)] transmission spectra of AAAs with periods of 1400–1100 nm and 1000–600 nm corresponding to ±(1,1) Au/quartz and ±(1,0) Au/quartz SPP-Bloch modes, respectively. For clarity, in panels (a) and (b), ✱ denotes ±(1,1) Au/quartz and ↓ denotes ±(1,0) Au/quartz modes.

Figure 2.2a, 2.2b show the experimental transmission spectra of AAAs as a function of period. For P = 1400–1100 nm, one primary mode is present and it correlates with the ±(1,1) Au/quartz mode, starting at λ = 1575 nm for P = 1400 nm. This mode blueshifts with decreasing period and the transmission reaches a maximum of roughly 12%. For P = 1200 and 1100 nm, another transmission resonance appears on the red edge between 1700 and 1800 nm,

and it corresponds with the ±(1,0) Au/quartz mode. Figure 2.2b shows the spectra for AAA's with periods from 1000 nm to 600 nm. For these shorter array periods the ±(1,1) Au/quartz mode has a weak transmission and is no longer evident past a period of 800 nm. The dominant transmission band in these spectra arises from the ±(1,0) Au/quartz mode. Its transmission maximum blueshifts with decreasing period and its maximum transmission increases significantly, from 9% to 35%, between $P = 1100$ nm and $P = 900$ nm. Past the point of maximum transmission at $P = 900$ nm, the transmission maximum of the mode continues to blueshift and the full width at half maximum (FWHM) of the peak increases along with a slight decrease in overall transmission.

Figures 2.2c, 2.2d show the results of the FDTD simulations for AAAs whose geometries correspond with the experimental AAAs (c with a and d with b). All the experimentally observable resonances are reproduced well in the FDTD calculations, with a few notable exceptions. At $P = 1400$ nm [Fig. 2.2c], in addition to the ±(1,1) Au/quartz mode at 1600 nm, there is another peak at 1390 nm, which is weakly present in the experimental spectra. In the FDTD calculation, this peak blueshifts and its FWHM decreases; however, this behavior is not evident in the experimental spectra. In addition, a very weak transmission peak, also not present in the experimental spectra, appears at 1450 nm for $P = 1400$ nm and shifts to 1150 nm for $P = 1100$ nm. The calculated spectra for periods 1000–600 nm [Fig. 2.2d] show excellent agreement with the experimental spectra [Fig. 2.2b], the only noteworthy difference is the lack of decreasing transmission past $P = 900$ nm, which is not present in the calculations. In addition to these differences, the absolute transmission found in the simulation is higher than that found experimentally and the calculated resonances are always sharper than the experimental resonances. The spectral features in Fig. 2.2c at the shorter wavelength arise from a combination

of the ±(1,1) Au/air SPP-Bloch mode as well as the ±(1,1) Au/air woods anomaly. These features are not seen in the experimental spectra [Fig. 2.2a] due to the low transmission of the FIB milled AAAs; however, a weakly defined ±(1,1) Au/air mode is evident. These spectral differences likely result from differences between the idealized structure of the arrays used in the simulation and the imperfect experimental structures, which may give rise to a "lossier" device that has a lower transmission and broader resonance for a given mode.

2.3.2 Comparison of λ_{max} Between Experimental and FDTD Simulated Spectra

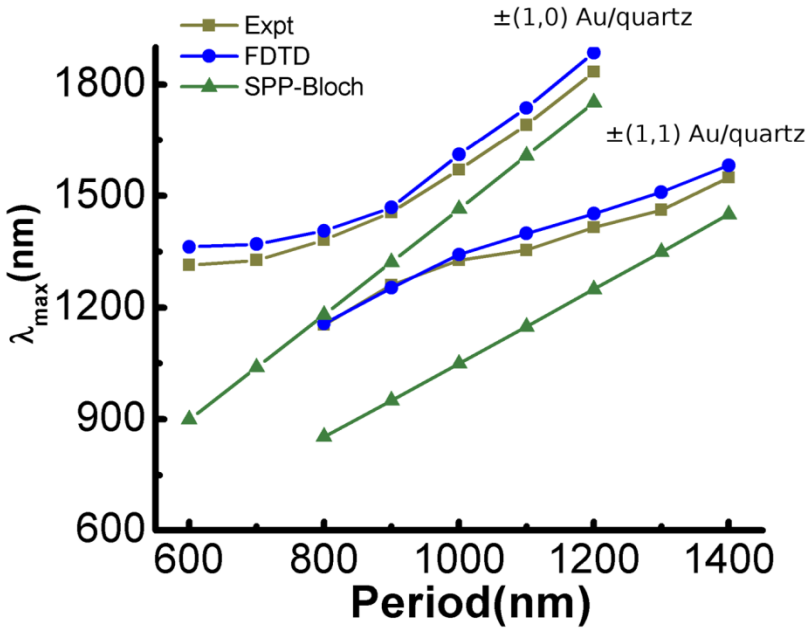

Figure 2.3. Comparison of measured λ_{max} (squares) from transmission spectra, FDTD calculated (circles) spectra, and calculatedλ_{SPP} (triangles) for AAAs at different periods.

A comparison between the observed transmission peaks, FDTD simulated peaks, and the calculated λ_{SPP} from Eq. (2.1) for a given period (Fig. 2.3) show similar trends for both the ±(1,1) and ±(1,0) Au/quartz modes. In general, the λ_{max} of the simulated peaks are in agreement with the

experimental λ_{max} to within 50 nm and they appear to show a redshift. The λ_{SPP} calculated from Eq. (2.1) shows a strong correlation but a large blueshift from the experimental λ_{max}. As the period is decreased the difference between the location of the calculated λ_{SPP} and the experimental λ_{max} remains within 150 nm for the Au/quartz modes. As the apertures are brought closer together, however, the difference between the calculated λ_{SPP} and measured λ_{max} increases substantially, approaching 400 nm for the ±(1,0) Au/quartz mode at $P = 600$ nm.[20] In the regime where the apertures are spaced far enough apart so that no significant overlap of the annular aperture's waveguide mode with the SPP-Bloch modes λ_{max}>1450 nm (this value is obtained from an FDTD simulation for a single annular aperture)] can occur, it is possible to correlate a particular transmission peak of the AAA to a SPP-Bloch mode. As the apertures are brought closer together so that the SPP-Bloch modes and the AAA waveguide modes can interact with each other, the nanostructure's transmission spectrum appears to reflect a more complex collection of processes occurring over the array. The FDTD simulations appear to capture these features.

2.3.3 Effect of Breaking Array Symmetry

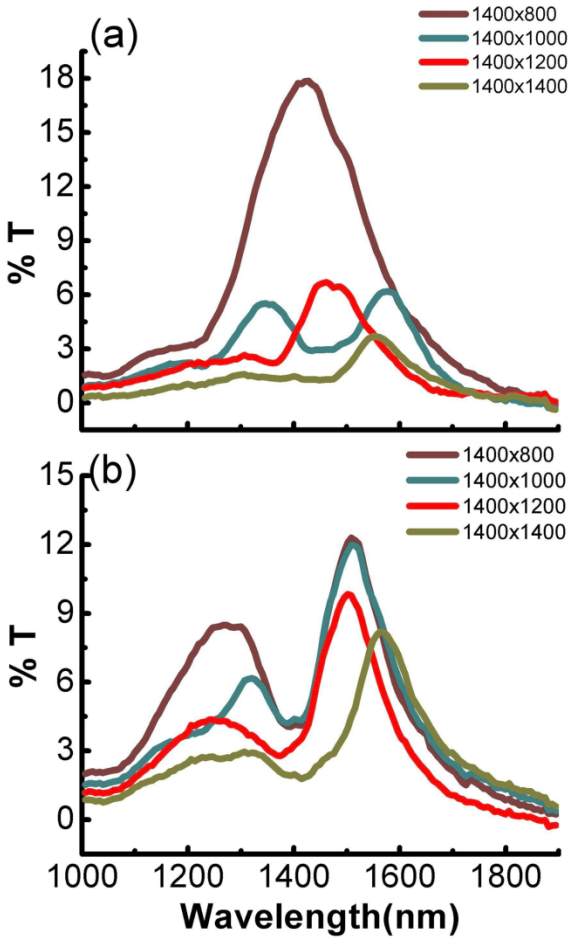

Figure 2.4. (a) Transmission spectra for asymmetric AAAs with the period on one axis held fixed at 1400 nm and the period along the perpendicular axis varied from 1000 to 600 nm, with the polarization of incident light along the varied axis and (b) asymmetric AAAs with the polarization along the axis with the fixed period.

The set of spectra in Fig. 2.4 show the dramatic effect of breaking the square symmetry of the AAAs. Figure 2.4a shows the transmission of AAAs for linearly polarized light whose field is

oriented along the axis in which the period changes. As the period is decreased the transmission peak corresponding to the ±(1,1) Au/quartz mode[21] (originally present in the square 1400×1400 nm^2 AAA) blueshifts and reaches a maximum transmission at 6% (half of that for the P = 1200×1200 nm^2 counterpart) and decreases to roughly 4% at P = 1400×800 nm^2. The dominant transmission peak in Fig. 2.4a is assigned to the ±(1,0) Au/quartz mode. This mode first appears near λ = 1600 nm for the 1400×1000 nm array. It blueshifts and increases in transmission from 6% to 18%, for the 1400×800 nm array. Changing the axis of the light polarization to be oriented along the direction of the static period gives rise to the spectra in Fig. 2.4b, which are quite distinct from those in Fig. 2.4a. The transmission spectra in this case do not show a strong systematic shift with the change in period. Rather, the transmission maintains the same features of the square 1400×1400 array, with the overall magnitude increasing as the period is decreased, along with a slight blueshift in the ±(1,1) Au/quartz mode. These data show that the SPP-Bloch modes play a significant role for the transmission of AAAs, and that the symmetry of the AAAs can be used to tailor the devices' frequency response for particular polarizations.

2.4 CONCLUSIONS

These studies show that the strong transmission observed with AAAs is strongly linked to the periodicity of the annular apertures in the array and the resonant excitation of SPP-Bloch modes, especially for the metal/substrate interface. In the context of creating frequency tunable structures, it is possible to optimize the spacing between the apertures so that the width of the transmission resonance is minimized and the transmission magnitude is maximized. These

findings have significant implications for the use of such structures in telecommunications and sensing applications with NIR photonic devices.

Acknowledgements: This work was supported by funds from NSF-NIRT (Grant No. ECS-0403865). The authors thank Alexandre Brolo for helpful discussions and Michael McDonald for nanofabrication technical support.

2.5 REFERENCES

1. T. W. Ebbesen, H. J. Lezec, H. F. Ghaemi, T. Thio and P. A. Wolff, Nature **391** (6668), 667-669 (1998).
2. H. A. Bethe, Physical Review **66** (7-8), 163-182 (1944).
3. H. Raether, *Surface Plasmons on Smooth and Rough Surfaces and on Gratings*. (Springer, Berlin, 1988).
4. H. F. Ghaemi, T. Thio, D. E. Grupp, T. W. Ebbesen and H. J. Lezec, Physical Review B **58** (11), 6779-6782 (1998).
5. A. G. Brolo, R. Gordon, B. Leathem and K. L. Kavanagh, Langmuir **20** (12), 4813-4815 (2004).
6. T. Nikolajsen, K. Leosson and S. I. Bozhevolnyi, Applied Physics Letters **85** (24), 5833-5835 (2004).
7. K. Tanaka, M. Tanaka and T. Sugiyama, Opt. Express **13** (1), 256-266 (2005).
8. F. I. Baida and D. Van Labeke, Optics Communications **209** (1–3), 17-22 (2002).

9. J. Salvi, M. Roussey, F. I. Baida, M. P. Bernal, A. Mussot, T. Sylvestre, H. Maillotte, D. Van Labeke, A. Perentes, I. Utke, C. Sandu, P. Hoffmann and B. Dwir, Opt. Lett. **30** (13), 1611-1613 (2005).

10. F. I. Baida, D. Van Labeke and B. Guizal, Appl. Opt. **42** (34), 6811-6815 (2003).

11. F. I. Baida, D. Van Labeke, G. Granet, A. Moreau and A. Belkhir, Applied Physics B: Lasers and Optics **79** (1), 1-8 (2004).

12. F. I. Baida and D. Van Labeke, Physical Review B **67** (15), 155314 (2003).

13. Y. Poujet, J. Salvi and F. I. Baida, Opt. Lett. **32** (20), 2942-2944 (2007).

14. S. M. Orbons and A. Roberts, Opt. Express **14** (26), 12623-12628 (2006).

15. M. I. Haftel, C. Schlockermann and G. Blumberg, Applied Physics Letters **88** (19), 193104-193103 (2006).

16. W. Fan, S. Zhang, B. Minhas, K. J. Malloy and S. R. J. Brueck, Physical Review Letters **94** (3), 033902 (2005).

17. S. M. Orbons, M. I. Haftel, C. Schlockermann, D. Freeman, M. Milicevic, T. J. Davis, B. Luther-Davies, D. N. Jamieson and A. Roberts, Opt. Lett. **33** (8), 821-823 (2008).

18. E. D. Palik, *Handbook of Optical Constants of Solids II, 1st ed.* . (San Diego, 1991).

19. J. J. Penninkhof, L. A. Sweatlock, A. Moroz, H. A. Atwater, A. van Blaaderen and A. Polman, Journal of Applied Physics **103** (12), 123105-123107 (2008).

20. It was not possible to assign the ±(1,0) Au/air SPP-Bloch modes, which for all AAA periods are ~50nm to the blue of the ±(1,1) Au/quartz modes. Because the FWHM for the transmission peaks is > 150nm, it may be that both modes contribute to the transmission in Fig. 2B.

21. $\lambda_{SPP}(i,j) = \frac{P_x P_y}{(P_x^2 i^2 + P_y^2 j^2)^{\frac{1}{2}}} \left(\frac{\varepsilon_d \varepsilon_m}{\varepsilon_d + \varepsilon_m}\right)^{\frac{1}{2}}$ is the analogous expression for SPP-Bloch modes when the period is unique along the x and y axis. P_x and P_y denote the periods along the x and y axis.

3.0 LOCALIZED SURFACE PLASMON EFFECTS IN NANOAPERTURE ARRAY EXTRAORDINARY OPTICAL TRANSMISSION

The thesis author performed device fabrication and experimental analysis for all the devices studied.

3.1 INTRODUCTION

This chapter explores how localized surface plasmons influence the transmission properties of both annular aperture array (AAA) devices as well as composite nanoparticle/nanoslit (NPNS) arrays. AAAs are compared to cylindrical nanohole arrays with identical geometry at multiple array periods and the results indicate that the optical response of AAAs is more complex than for cylindrical nanohole arrays. Looking at AAAs with different aperture geometry showed that the localized surface plasmon resonance (LSPR) excited within the metallic island nested within the aperture of the array modulates the wavelength of maximum transmission, however, the period of the array and the resonant excitation of SPP-Bloch modes are important as well. For NPNS arrays, we show that subwavelength transmission, without grating induced SPP-Bloch modes, is readily achieved and can be tuned solely by changing the geometry of the nanoparticles within the nanoslit.

It is generally accepted that for two-dimensional nanoaperture arrays in an optically thick metal film that the observed extraordinary optical transmission (EOT)[1] is due to the resonant excitation of surface plasmon polaritons that, depending on the array period and type of metal, exhibit discrete transmission peaks at wavelengths given by the following relationship[2]:

$$\lambda_{SPP}(i,j) = \frac{p}{(i^2 + j^2)}\left(\frac{\varepsilon_d \varepsilon_m}{\varepsilon_d + \varepsilon_m}\right)^{\frac{1}{2}} \tag{3.1}$$

where p is the array period, i,j are integers that correspond to the Bragg-type scattering order, ε_d is the dielectric constant for the dielectric medium, and ε_m is the wavelength dependent dielectric function for the metal. While this straightforward model provides a succinct description of the wavelength at maximum transmission for a given SPP-Bloch mode, it does not yield any predictive insight into the shape of the peak or magnitude of the transmission. Additionally for more complex nanoaperture array structures, such as the annular aperture arrays discussed in chapter 2, the model deviates significantly from experimental data. This is presumably due to the fact that the model encompasses transmission due to surface plasmon polaritons Bloch (SPP-Bloch) modes, so for devices in which other physical processes are important to the optical response, it is not surprising that the model does not adequately describe observed experimental data.

Recent work by several groups has explored the role of localized surface plasmons in the EOT process for a variety of novel nanoaperture array devices. It has been shown that a single subwavelength aperture can support localized surface plasmon modes[3] and Degiron and Ebbesen[4] have investigated their role in two-dimensional nanoaperture arrays. They found that for nanoaperture arrays localized modes can influence the transmission, but the array period was the dominant factor in the transmission process. For more complex devices such as annular aperture arrays, Hu and coworkers[5] found that when the annulus inside the aperture was

asymmetric, the transmission showed peaks that varied with the polarization of the incident light. They attributed this to localized surface plasmons excited on the center annulus; however this study did not systematically explore the relationship between propagating modes and localized modes in AAA devices.

As seen in chapter 2 of this thesis, the AAA devices studied deviated from both the SPP-Bloch model as well as the model proposed by Baida and coworkers[6] for AAAs which states that the transmission is primarily due to the TE_{11} coaxial waveguide mode supported by the device. The cutoff for a TE_{11} waveguide mode is given as

$$\lambda_{cTE_{1,1}} = \pi(R1 + R2) \tag{3.2}$$

where R1 and R2 are the inner and outer radius of the annular aperture. This model implies that the only pertinent variable in the transmission of an AAA is the geometry of the aperture, which is in clear contrast to the results shown in chapter 2. One possible explanation for the discrepancy could be due to localized surface plasmon modes that can be supported by the central disk inside the annular aperture. To better understand the reason for this discrepancy, AAAs were fabricated in which both the geometry and period of the device were varied. In addition, nanohole arrays with outer geometry identical to AAAs were fabricated at different periods and compared to AAAs. The data for different geometry AAAs combined with the comparison to nanohole arrays suggest that localized surface plasmons are playing a significant role in the location of the primary transmission peak.

To further probe for LSPR based effects, square annular aperture arrays are fabricated and the period is varied systematically along one axis while keeping the other axis held constant. The transmission shows non-monotonic shifts with changes in the period and the characteristic red-shift to blue-shift transmission as observed for nanoparticle array diffractive coupling. This

suggests that the central disk inside the coaxial aperture is functioning in a manner analogous to a nanodisk array. These findings suggest that LSPR modes in annular aperture array devices play a significant role in the extraordinary optical transmission process.

To further probe the role of LSPR modes in the EOT of nanoaperture arrays, a novel device was fabricated that consists of nanoparticles nested within a nanoslit. The nanoslit aperture is unique in that it poorly transmits light that is polarized along the long-axis of the aperture. Studies were conducted in which both the shape, size and number of nanoparticles in the aperture were varied and show a distinct dependence of the LSPR on the transmission. This represents a novel device which can support EOT without grating based SPP modes.

3.2 DEVICE FABRICATION AND CHARACTERIZATION

Nanoaperture aperture arrays were milled into 150nm Au films (with a 3nm Ti adhesion layer) on a quartz substrate with a focused ion beam system (Seiko SMI 3050SE). Unless otherwise noted, Zeroth order transmission spectra were collected with a microspectrophotometer (CRAIC QDI 2010) equipped with a 0.13NA 5x objective, a collimated illumination source (Fiber coupled 75W Xe Arc), and a Glan-Taylor polarizer placed directly below the substrate. The reference for the transmission spectra was a 20μm window milled into the same gold film as the arrays. All arrays were spaced at least 150μm apart in order to ensure that they do not couple with one another. Light was incident on the quartz side of the sample.

3.3 RESULTS AND DISCUSSION

3.3.1 Comparison of AAAs to Nanoaperture Arrays

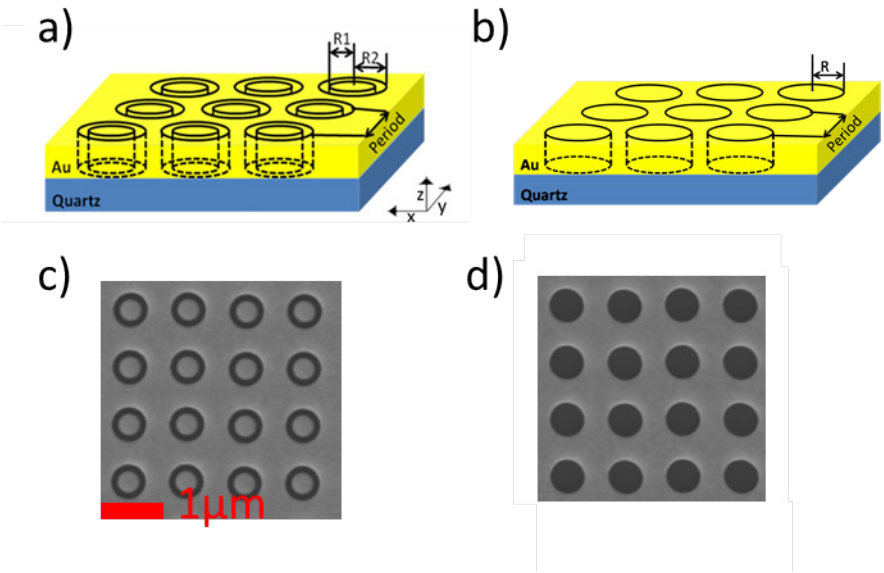

Figure 3.1. Diagram of the system under study: a 150 nm gold film on quartz with a) annular apertures and b) nanoholes in an array. Individual annular apertures are defined by the inner radius R1 and the outer radius R2. Individual nanoholes are defined by a radius R. The period represents the spacing between adjacent apertures in the array. C) SEM image of FIB milled AAAs with R1 = 125 nm, R2 = 215 nm and period = 1000 nm. (d) Nanohole array SEM image with R = 215nm with period = 1000nm.

The period dependent transmission characteristics of AAAs and nanohole arrays with complementary geometry were studied (figure 3.1). The nanohole arrays were fabricated such that they had an identical outer radius to the AAAs so that any differences in the transmission could be attributed to the presence of the central disk inside the annular aperture. Figure 3.2a shows the 0^{th} order transmission for AAAs with R1 = 125nm and R2 = 215nm for an array

period 1000nm to 600nm. For these array periods the ±(1,1) Au/quartz mode has a weak transmission and is no longer evident past a period of 800 nm. The dominant transmission band in these spectra arises from the ±(1,0) Au/quartz mode. Its transmission maximum blue-shifts with decreasing period and its maximum transmission increases significantly, from 20% to 35% relative to the $20\mu m^2$ reference, between $P =$ 1000 nm and $P =$ 900 nm. Past the point of maximum transmission at $P =$ 900 nm, the transmission maximum of the mode continues to blue-shift and the full width at half maximum (FWHM) of the peak increases along with a slight decrease in overall transmission.

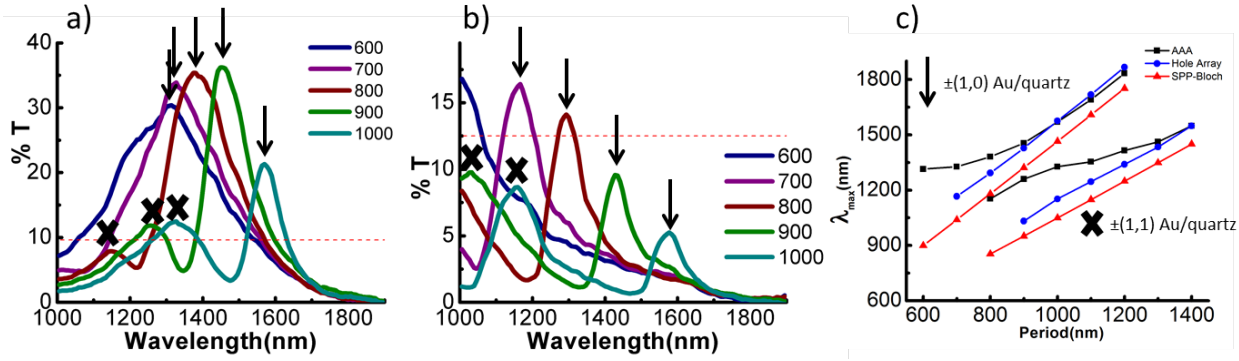

Figure 3.2. Comparison of the near-infrared 0^{th} order transmission of a) annular aperture arrays, b) nanohole arrays for array period 1000nm to 600nm and c) a comparison of λ_{max} vs. array period for AAAs, nanohole arrays, and the SPP-Bloch model (Eq. 3.1). The red dashed line corresponds to the total percentage open area of the device.

The set of spectra in figure 3.2b are for nanohole arrays with a radius = 215nm. In comparison to the transmission for AAAs as shown in figure 3.2a, there are both similarities and differences which highlight the effect of aperture geometry on the optical response of the devices. In figure 3.2b, as the period is decreased from 1000nm to 600nm the peaks

corresponding to the ±(1,0) Au/quartz mode and ±(1,1) Au/quartz blue-shift and the intensity increases which is similar to the response of the AAAs. Looking at the magnitude of the overall transmission compared to the total open area of the device gives a useful metric of the EOT, which by definition is percent transmission beyond the percent total open area of the device. It is evident that AAAs show significantly enhanced transmission relative to the nanohole arrays. This is especially evident in the transmission for the ±(1,0) Au/quartz mode. For the AAAs, at all array periods, the transmission normalized to the total open area exceeds unity by up to a factor ≈ 3 for P = 900nm. Whereas for the nanohole arrays, the ±(1,0) Au/quartz mode only shows transmission beyond unity for P < 800nm. Another contrast between both devices is seen in the trends for the overall peak shape and FWHM. For the nanohole array ±(1,0) Au/quartz mode, as the period is decreased the FWHM and overall shape of the peak show little variation, unlike the AAA ±(1,0) Au/quartz mode. Additionally the magnitude of the blue-shift as the period is decreased appears to be consistent for the nanoholes arrays, unlike the AAAs that show a change in the magnitude of the blue-shift for the ±(1,0) Au/quartz mode below P = 900nm.

To better understand the behavior of the peak shift vs. period, λ_{max} is plotted for AAAs, nanohole arrays, and the SPP-Bloch model from Eq. 3.1 (Figure 3.2c) for both ±(1,0) Au/quartz and ±(1,1) Au/quartz modes for array period ranging from 1400nm – 600nm. For the AAAs, the overall agreement to the SPP-Bloch model is poor. This is particularly evident for the ±(1,1) Au/quartz mode. The ±(1,0) Au/quartz mode shows a qualitative agreement with the shift vs. period for array period 1200nm – 900nm, but deviates from the observed trend past that point. In contrast, the nanohole arrays capture the trend of the SPP-Bloch model with the exception that across all array periods the transmission is red-shifted. This is likely due to a mismatch between theory and experiment for the optical constants of both the metal and the quartz substrate. It is

evident based on the data presented in figure 3.2a-c that AAA transmission contains elements indicative of SPP-based transmission, namely the period dependence on the location of λ_{max}. However, compared to a geometrically analogous nanohole array as well as Ebbesen's model for SPP mediated nanoaperture array transmission, there are significant discrepancies which can only be attributed to the presence of the central disk inside the annular aperture. Since for the AAAs studied, the cutoff wavelength for the TE_{11} waveguide mode based on Eq. 3.2 is 1067nm, it is not certain whether or not the observed discrepancy is due to interactions between the waveguide mode with the SPP modes or possibly due to localized surface plasmon resonances that can be supported by the central disk.

3.3.2 Effect of Aperture Geometry on AAA Transmission

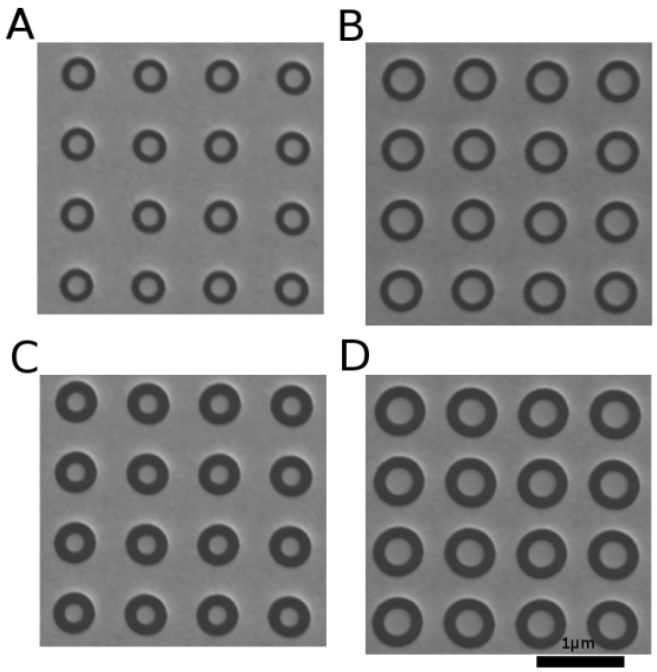

Figure 3.3 - SEM of AAAs under study A: R1 = 120nm R2 = 170nm, B: R1 = 170nm R2 = 220nm, C: R1 = 120nm R2 = 220nm, D: R1 = 170 R2 = 270nm

In section 3.4.1 it was shown that the EOT phenomenon observed in annular aperture arrays in part arises from the resonant excitation of SPP-Bloch modes, which then couple into the coaxial waveguide mode of the annular aperture to produce the very strong transmission which is sensitive to the period of the array. However, it was also observed that interesting behavior happens in the transmission spectra for AAAs as the period is reduced and the apertures are brought closer together. Namely, the transmission broadens significantly, deviates considerably from the SPP-Bloch model for predicting λ_{SPP}, and for periods less than 900nm the transmission begins to attenuate. Work with cylindrical nanoaperture arrays have shown that localized surface plasmons excited at the edges of the nanoaperture can influence the transmission properties[4]. With annular aperture arrays, not only is it possible to excite localized surface plasmons at the edges of the aperture, but on the metallic island within the aperture as well. To explore the relationship between local modes excited on the center pillar, four sets of AAAs were fabricated (Fig 3.3). The unique geometries of the four AAAs created two conditions: one in which the gap between the center pillar and outer ring was 50nm and another where it is 100nm. These geometries were created for two different center pillar sizes R1 = 120nm and R1 = 170nm. With this configuration of geometries it is possible to separate effects arising from the local surface plasmons within the center disk from effects arising from the change in the cutoff of the TE_{11} waveguide mode from the different geometries.

As with previous AAAs, 20 x 20 arrays were FIB milled into a 150nm thick gold film with a 3nm Ti adhesion layer. Transmission measurements were collected with an unmodified microspectrophotometer (CRAIC QDI-2010), for these studies standard köhler illumination conditions, in which instead of using a fiber-optic collimated beam of light to illuminate the arrays, the light was focused using a standard microscope condenser. These measurements were

taken with unpolarized light. A 20µm x 20µm square milled into the gold film was used at the reference for the transmission measurements.

The results are shown in figure 3.4 panels A-D. As was seen with previously studied AAAs in chapter 2, decreasing the periodicity of AAAs yields transmission resonances that initially appear at ~1800nm for a given mode, blue shift, broaden, and increase in transmission to a point at which the transmission attenuates and broadens significantly. For each AAA, there are two primary modes for the periods studied: ±(1,0) and ±(1,1) Au/quartz SPP-Bloch modes. The ±(1,1) modes are the weakly transmitting (relative to the ±(1,0) modes) broad peaks between 1500nm and 1000nm. The ±(1,0) Au/quartz modes however can be tracked from their onset at P=1100nm and followed with each subsequent decreasing step in the period of the AAA.

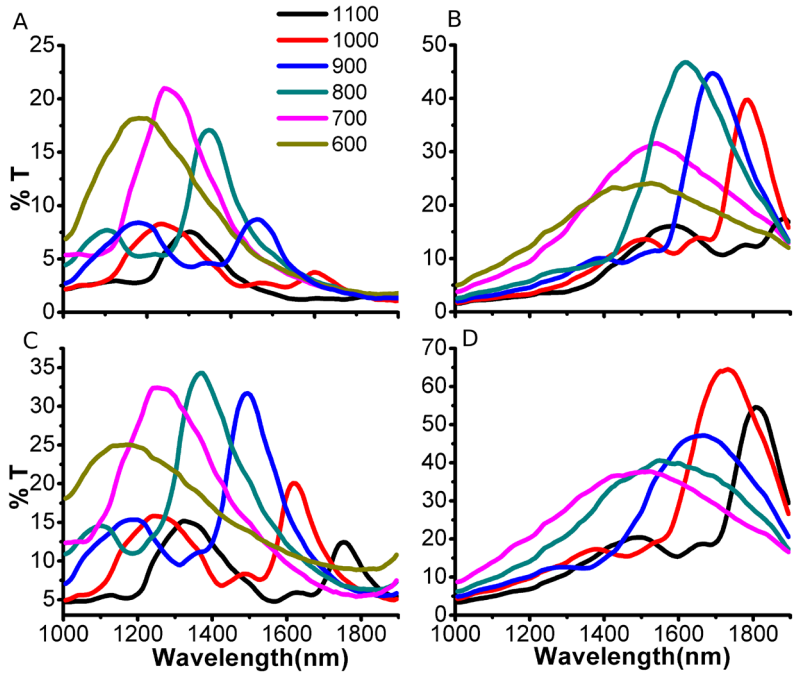

Figure 3.4. Transmission spectra of AAAs at periods corresponding to ±(1,0) SPP-Bloch modes for A: R1 = 120nm R2 = 170nm, B: R1 = 170nm R2 =220nm, C: R1 = 120nm R2 = 220nm, and D: R1 = 170nm R2 = 270nm.

The set of spectra in Figure 3.4 A and C are for a fixed R1 = 120nm and R2 = 170nm (A) and 220nm (C). The primary effect of the change in aperture size is an overall increase in maximum transmission and FWHM of each mode at all periods. In the context of the significance of the TE_{11} waveguide constraint on geometry this is a surprising result. If the waveguide was playing a significant role in the transmission of the AAA, then the cutoff for the transmission within the waveguide should red-shift by increasing the outer ring width, which clearly is not the case. For AAAs with R1 = 170nm and R2 = 220nm (Figure 3.4 B) and 270nm (Figure 3.4 D), λ_{max} is significantly red shifted for all periods and their corresponding SPP-Bloch modes. As with AAAs with R1 = 120nm, the effect of increasing the difference R2-R1 is to increase the overall transmission as well as the FWHM. However, looking at the threshold from where the transmission of the ±(1,0) Au/quartz SPP-Bloch mode passes through the maximum for the AAA series, it is clear that by increasing R1 the period corresponding to the maximum transmission for the AAA increases and the subsequent transmission for arrays with periodicity less than that which corresponds to maximum transmission display very significant attenuation in the signal in addition to large broadening to the extent that there is no single peak, rather a broadband signal that encompasses the range of the NIR detector.

The relationship between the location of maximum transmission for the ±(1,0) SPP-Bloch mode and AAA geometry is summarized in figure 3.5. For reference SPP-Bloch calculations for the ±(1,0) Au/quartz interface for all periods are also included. It is evident that at larger periods, it is possible to correlate the transmission to a given SPP-Bloch mode, however this model breaks down as the arrays are brought closer together. For all array periods, the wavelength of maximum transmission is red-shifted for AAAs in which the center disk is larger

(R1 = 170nm). In addition, these results indicate that the SPP-Bloch approximation is more accurate for AAAs with a smaller center disk.

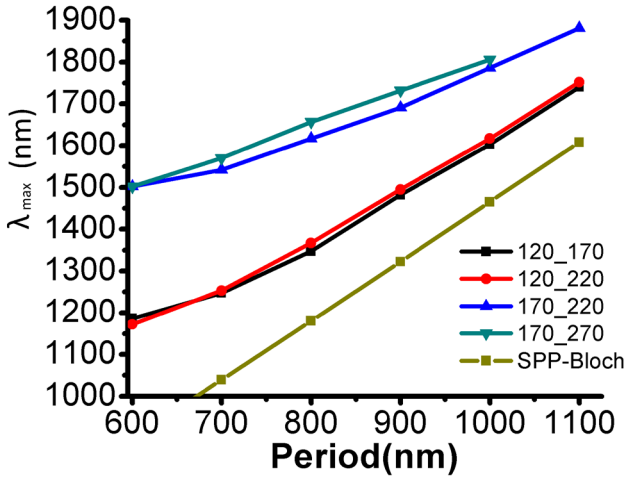

Figure 3.5. λ_{max} vs. period for all AAAs studied as well as SPP-Bloch calculations for the ±(1,0) Au/quartz interface.

These data suggest that the transmission for AAAs is not mediated solely by a waveguide mode due to the geometry of the aperture or plasmonic Bloch modes excited over the array. It is clear that the center disk has a significant effect not only on the period of maximum transmission, but the width over the transmission for a given mode as well. The dependence on R1 for the AAAs are analogous to the dependence of the scattering of plasmonic nanodisk arrays on the radius of the nanodisk[7].

3.3.3 Nanoparticle array diffractive coupling in annular aperture arrays

As demonstrated in the previous sections, the optical response of annular aperture arrays cannot be described by a simple SPP-Bloch model or through a TE_{11} waveguide model. There is

evidence based on the studies of the effect of aperture geometry that localized surface plasmons excited upon the central disk of the annular aperture play a significant role in the transmission of the devices. However, it is difficult to isolate LSPR based effects from other optical phenomena. One approach would be to consider an annular aperture array as a combination of a nanohole array and a nanoparticle array superimposed upon one another. In this context the annular aperture array should retain features of both devices. This can be affirmed by the period dependent transmission of the AAAs which is analogous to the response of nanohole arrays, but fail to agree well with Eq. 3.1 for predicting the location of λ_{max}. Likewise, features of nanoparticle arrays should be present within the optical response of the annular aperture array if LSPRs excited upon the nanoparticle within the aperture are affecting the transmission process.

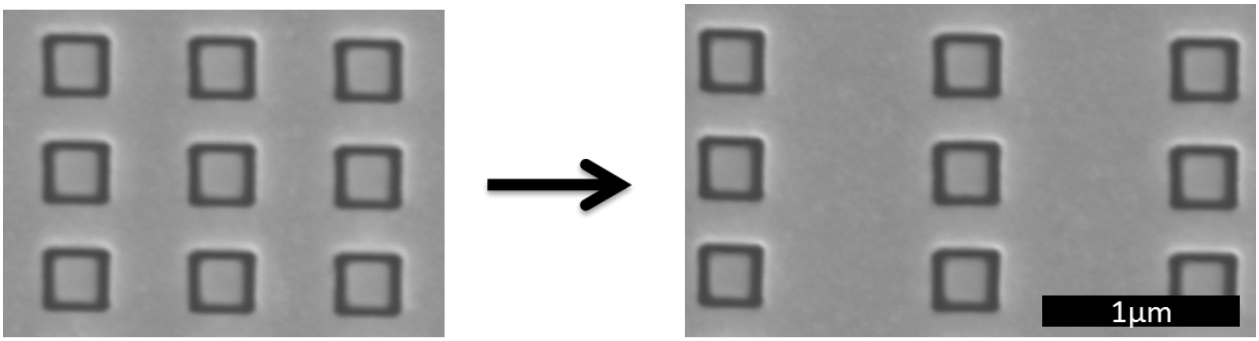

Figure 3.6. SEM images of square annular aperture arrays studied. The geometry of the aperture is defined by an inner width of 250nm and an outer width of 430nm. The arrays are FIB milled into a 150nm thick Au film on quartz and the array period is fixed along the y-axis at 800nm and varied along the x-axis from 800nm to 1300nm.

In order to decouple LSPR effects from SPP effects in an annular aperture array, devices were fabricated in such a manner that the period was held fixed along one axis and sequentially

changed on the perpendicular axis. By looking at transmission when the incident light E-field is polarized along the fixed axis of the array, changes due to diffractive coupling between light scattered isotropically by the nanoparticle within the nanoaperture and grating modes scattered over the array that are not due to SPPs can be elucidated.

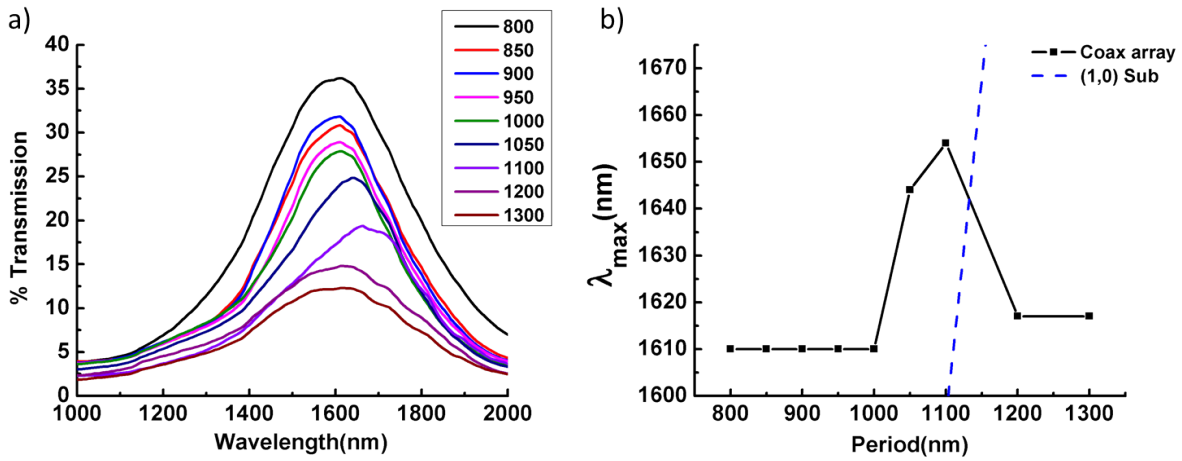

Figure 3.7. a) experimental transmission spectra and b) λ_{max} vs. period of the square annular aperture arrays. The period of the array is varied along one axis from 800nm to 1300nm and kept fixed at 800nm on the perpendicular axis. The dashed line in panel b) represents the light line: $\lambda = n_{substrate} \bullet period$.

The transmission for different array periods for the square annular apertures is shown in figure 3.7 a). In general, the devices exhibit a single, broad, transmission peak at all array periods. As the period is increased from 800nm to 1000nm in 50nm increments there is a slight decrease in the observed transmission magnitude from 36% to 28% and no significant shift in the position of λ_{max} is observed. Upon an increase in the period to 1050nm, the transmission peak begins to redshift, broaden, and continues to decrease in magnitude. At array period of 1100nm

the transmission peak appears to become asymmetric, the red-shift in λ_{max} continues and the observed intensity has decreased to 18%. As the array period is increased to 1200nm, the peak now blue-shifts, becomes symmetric, and the observed intensity is decreased. Past 1200nm, the only change is a decrease in the observed transmission magnitude.

The plot of λ_{max} vs. period illustrates the interaction between the observed transmission and the light line for the ±(1,0) diffractive mode (dashed line) of the nanoparticle array. It is evident that the red-shift to blue-shift behavior occurs at array periods in which the light line overlaps with the observed λ_{max} for the device transmission. This effect has been observed and characterized for nanoparticle arrays and is the first time such an effect has been reported for nanoaperture array based transmission. The observed dependence of the transmission magnitude, the width of the resonance, and the position of λ_{max} on the period suggests that the transmission through the nanoapertures is influenced by the LSPR excitation of the nanoparticles and their coupling effects in both the near and far field. Earlier studies have shown[8-14] that the period of both two dimensional arrays and linear chains of noble metal nanoparticles exhibit spectral changes in the visible that are analogous to those observed here in the near-IR for square annular aperture arrays. It is believed that the non-monotonic shift of λ_{max} for two dimensional arrays of nanoparticles, which was first predicted by Meier *et al*[15] and later experimentally verified and elaborated upon by Lamprect *et al*[16], is caused by the interaction of lattice modes with light scattered by the nanoparticles as the transmission peak approaches and intersects the light line, $\lambda = n_{substrate} \cdot period$ (dashed line, Fig 3.7b). For $period$ = 800nm to 1000nm, $\lambda_{max} > \lambda_{light}$ and along the x-axis of the array the nanoparticles are spaced close enough that interactions between their dipole fields are important. The in-phase addition of the dipole fields results in a gradual red-shift which is observed as the period is increased. For array periods from 1050nm to

1100nm, λ_{max} intersects λ_{light} and a new diffractive order that radiates at a grazing angle and interacts with the scattered fields of individual nanoparticles emerges and corresponds to the point of maximum red-shift and minimum bandwidth. As the period increases towards 1300nm the array enters the regime where $\lambda_{max} < \lambda_{light}$, and the radiative damping of the scattered fields of each nanoparticle within the array increases, causing the increased broadening and the decrease in total transmission.

3.3.4 LSPR Mediated EOT

Studies of the optical transmission of both circular and square annular aperture arrays in sections 3.4.2 and 3.4.3 have indicated that localized surface plasmons excited upon the central disk inside the aperture these devices can have a significant influence on the observed transmission. However due to the variety of processes that play a part in the transmission mechanism: SPP-Bloch modes, coaxial waveguide modes, and localizes surface plasmon modes, it is challenging to elucidate the impact of each process on the overall transmission which is important to understand for designing structures for nanophotonic applications.

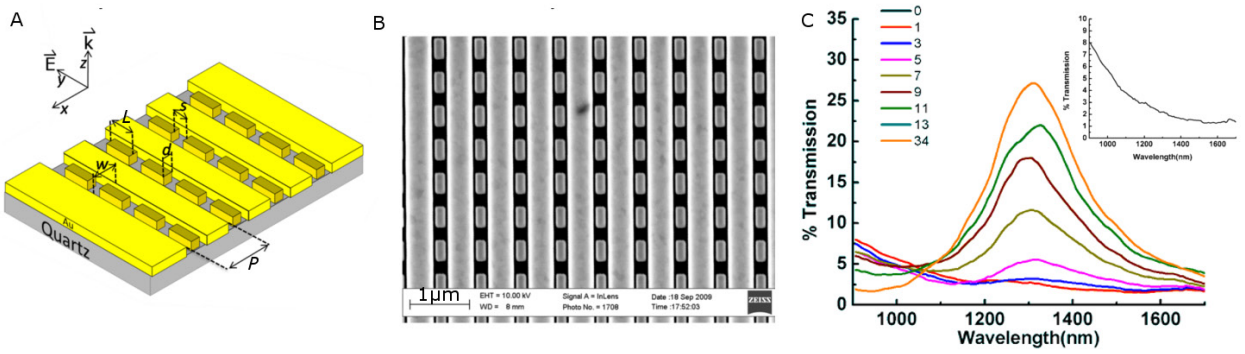

Figure 3.8. Diagram of the system under study A: a 150nm gold film on quartz with a 3nm Ti adhesion layer in which nanoparticle chains are nested within a subwavelength nanoslit. Single nanoslits are defined by a width *w* and fixed spacing *P*, which represents the period of the array. The nanoparticle chains within the slit are defined by a length along the y-axis *L* and width along the x-axis *d*. The separation between individual nanoparticles within the chain is defined as *s*. B: SEM image of a FIB milled nanoparticle/nanoslit array. For the nanoslit: $w = 240$nm and $P = 517$nm and for the nanoparticles: $L = 305$nm, $w = 160$nm, $s = 210$nm. C: Transmission spectra of NPNS arrays as a function of the number of nanoparticles per slit ranging from 1(red line) to 34(orange line), inset is the spectra for bare nanoslits with no nanoparticles present.

To further understand the role of LSPR excitation of a nanoparticle within a subwavelength aperture on the transmission spectrum, composite nanoparticle / nanoslit arrays (NPNS, Figure 3.8a) were fabricated. To separate grating induced plasmonic modes from the LSPR of the nanoparticle, the electric field of the incident light was polarized along the direction of the nanoslit axis. The transmission spectra shown in Figure 3.8 panel c) are for NPNS arrays in which the number of nanoparticles per slit was increased from 1 nanoparticle per slit up to 34 nanoparticles per slit. Initially, for < 8 nanoparticle per slit, the transmission resonance is very weak and less than 5% in total magnitude. Increasing the number of nanoparticles in each

nanoslit causes the initially broad resonance to narrow and take on a nearly Lorentzian shape. Although the open area in the nanoslit is decreasing with increasing nanoparticle number, its transmission increases. At 34 nanoparticles per slit, at which point the 20μm long nanoslit is fully occupied, one observes a well defined resonance with a λ_{max} of 1300nm and an overall transmission magnitude approaching 30%.

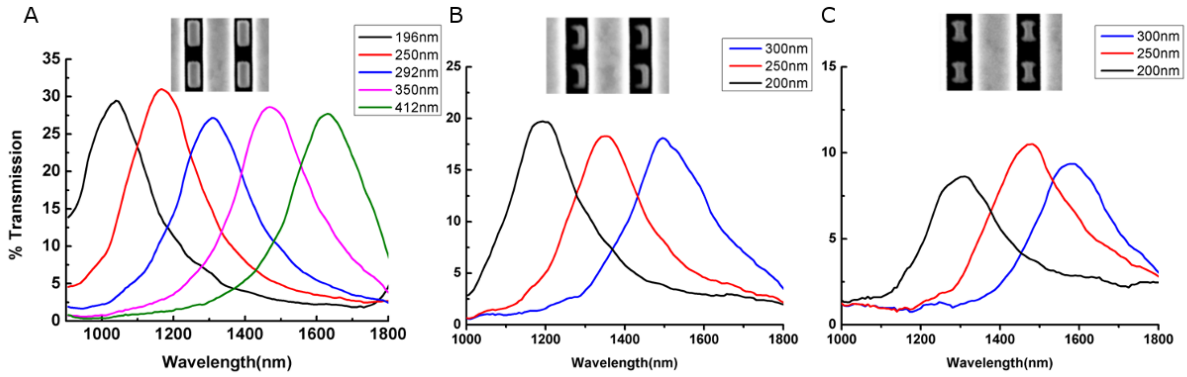

Figure 3.9. NPNS array near-IR transmission spectra with an inset SEM image for A: rectangular nanoparticles in which the length is varied from 412nm – 196nm, B: C-shaped nanoparticles of length 300nm – 200nm, and C: I-shaped nanoparticles of length 300nm – 200nm. For all arrays P = 650nm, s = 210nm, w = 240nm.

To better understand the relationship between the nanoparticle geometry and the transmission, different types of nanoparticles were fabricated within the NPNS array device (Figure 3.9) and the length of the nanoparticle along the axis of the E-field polarization was varied. Figure 3.9A shows the transmission spectra of NPNS arrays for which the length of a rectangular nanoparticle within the nanoslit was varied from 412nm – 196nm. The nanoslit period was fixed at 650nm and the spacing between nanoparticles was fixed at 213nm. As L is decreased, λ_{max} blue-shifts and its transmission is consistently above 25%. Each individual resonance is relatively broad,

and has a FWHM of about 200nm, regardless of the size of the nanoparticle. Similar trends are apparent in Fig 3.9B and 3.9C, for the "I" and "C" shaped nanoparticles. Notable differences are the modest red-shift in the transmission relative to the rectangular nanoparticles and the lower overall transmission magnitude, which is probably caused by the reduced scattering cross section of the individual nanoparticles.

The relationship between the scattering of nanoparticles and nanoparticle size has been extensively studied for single nanoparticles as well as linear chains and two-dimensional arrays [11, 17-20]. The studies reported here appear to be the first in which the transmission through subwavelength apertures in an optically thick metal film has been controlled by the localized surface plasmon resonance of noble metal nanoparticles. Comparisons of these spectra with those of extinction measurements for both nanoparticle chains and arrays underscores their similarity and suggests that the phenomenology observed with the latter should be reproduced by the subwavelength transmission through NPNS arrays. Given that the transmission is consistently above 25% for all NP sizes and that the total open area relative to the reference aperture is about 20%, implies that the device is transmitting light through subwavelength geometries with an efficiency of about unity.

3.4 SUMMARY AND CONCLUSION

The studies reported herein have illustrated the discrepancy between the transmission of AAAs and nanohole arrays. AAA devices were found to retain some qualitative features of the SPP-Bloch model, namely the period dependent location of λ_{max}, however AAAs were found to show significant deviations as well which were attributed to the influence of LSPR modes supported

by the central disk of the AAA. The ability of the nanoparticle-based LSPR to interact with two-dimensional SPP-Bloch modes and to drive subwavelength transmission is an altogether surprising result with implications for both understanding the nature of the subwavelength transmission process and for the design of novel plasmonic devices. We expect that many of the phenomena associated with both linear chains of nanoparticles as well as two-dimensional nanoparticle arrays can be exploited in a nested nanoparticle/nanoaperture format.

3.5 REFERENCES

1. T. W. Ebbesen, H. J. Lezec, H. F. Ghaemi, T. Thio and P. A. Wolff, Nature **391** (6668), 667-669 (1998).
2. H. F. Ghaemi, T. Thio, D. E. Grupp, T. W. Ebbesen and H. J. Lezec, Physical Review B **58** (11), 6779-6782 (1998).
3. J. Prikulis, P. Hanarp, L. Olofsson, D. Sutherland and M. Käll, Nano Letters **4** (6), 1003-1007 (2004).
4. A. Degiron and T. W. Ebbesen, Journal of Optics A: Pure and Applied Optics **7** (2), S90 (2005).
5. D. Hu, C.-Q. Xie, M. Liu and Y. Zhang, Physical Review A **85** (4), 045801 (2012).
6. F. I. Baida and D. Van Labeke, Optics Communications **209** (1–3), 17-22 (2002).
7. C. L. Haynes, A. D. McFarland, L. Zhao, R. P. Van Duyne, G. C. Schatz, L. Gunnarsson, J. Prikulis, B. Kasemo and M. Käll, The Journal of Physical Chemistry B **107** (30), 7337-7342 (2003).
8. B. Auguié and W. L. Barnes, Physical Review Letters **101** (14), 143902 (2008).

9. A. Bouhelier, R. Bachelot, J. S. Im, G. P. Wiederrecht, G. Lerondel, S. Kostcheev and P. Royer, The Journal of Physical Chemistry B **109** (8), 3195-3198 (2005).

10. E. M. Hicks, S. Zou, G. C. Schatz, K. G. Spears, R. P. Van Duyne, L. Gunnarsson, T. Rindzevicius, B. Kasemo and M. Käll, Nano Letters **5** (6), 1065-1070 (2005).

11. A. Pinchuk and G. Schatz, Applied Physics B: Lasers and Optics **93** (1), 31-38 (2008).

12. J. Sung, E. M. Hicks, R. P. Van Duyne and K. G. Spears, The Journal of Physical Chemistry C **111** (28), 10368-10376 (2007).

13. J. Sung, E. M. Hicks, R. P. Van Duyne and K. G. Spears, The Journal of Physical Chemistry C **112** (11), 4091-4096 (2008).

14. L. Zhao, K. L. Kelly and G. C. Schatz, The Journal of Physical Chemistry B **107** (30), 7343-7350 (2003).

15. M. Meier, A. Wokaun and P. F. Liao, J. Opt. Soc. Am. B **2** (6), 931-949 (1985).

16. B. Lamprecht, G. Schider, R. T. Lechner, H. Ditlbacher, J. R. Krenn, A. Leitner and F. R. Aussenegg, Physical Review Letters **84** (20), 4721-4724 (2000).

17. G. C. Schatz, A. A. Lazarides and K. L. Kelly, Abstr Pap Am Chem S **224**, U298-U298 (2002).

18. C. L. Haynes, A. D. McFarland, L. Zhao, R. P. Van Duyne, G. C. Schatz, L. Gunnarsson, J. Prikulis, B. Kasemo and M. Kall, The Journal of Physical Chemistry B **107** (30), 7337-7342 (2003).

19. J. Sung, E. M. Hicks, R. P. Van Duyne and K. G. Spears, J Phys Chem C **111** (28), 10368-10376 (2007).

20. J. Sung, E. M. Hicks, R. P. Van Duyne and K. G. Spears, J Phys Chem C **112** (11), 4091-4096 (2008).

4.0 COMPOSITE NANOPARTICLE NANOSLIT ARRAYS: A NOVEL PLATFORM FOR LSPR MEDIATED SUBWAVELENGTH OPTICAL TRANSMISSION

This work has been published as Matthew J. Kofke, David H. Waldeck, and Gilbert C. Walker, *Optics Express* **18** (8), 7705-7713 (2010). The thesis author fabricated nanostructures, collected and analyzed data, and wrote the manuscript.

4.1 INTRODUCTION

Near infrared transmission of light through subwavelength slit arrays is shown to be significantly influenced by resonant metallic nanoparticles placed within the structure. Experimental and calculated transmission spectra show how the size, orientation of the nanoparticles, and the period of the nanoslit array influence the maximum transmission wavelength, the magnitude of the transmission, and width of the resonance. These findings suggest that the localized surface plasmon resonance (LSPR) of metallic nanoparticles and their subsequent near and far-field interactions can modulate the subwavelength transmission and bandwidth of nanoaperture array devices in optically thick metal films.

The investigation of the optical response of subwavelength metallic nanoparticle[1-3] and nanoaperture array[4] devices has yielded fundamental insights[5, 6] into the interaction of visible and

near-IR light with nanomaterials. Much of the attention has focused on the optical response to ordered arrays of noble metal nanoparticles. Fundamental studies[7-13] show that it is possible to fine tune the optical response of these systems by varying the coupling of localized surface plasmons through key geometrical properties such as nanoparticle size or spacing. In addition to fundamental studies, numerous reports demonstrate the application of such plasmonic nanostructures in areas such as near field imaging[14], plasmonic waveguiding[15], photovoltaics[16, 17], biosensing[18-20], and as molecular rulers[9, 11, 21-24] among others. The electromagnetic field confinement and amplification, which arises from the excitation and interaction of localized surface plasmons with the environment, shows potential for application in numerous fields of study.

Analogous to nanoaperture arrays, nanoslit arrays are capable of transmitting light beyond the diffraction limit. However, the transmission process has proven to be less straightforward[25-33], because the nanoslit can support multiple modes of transmission. Typically nanoslit array devices have transmission profiles that reflect the complex nature of the transmission process. Because transmission of light polarized along the nanoslit direction is strongly attenuated, the transmission of nanoslit array devices is commonly measured with the incident light polarized perpendicular to the slit. Scattering by the nanoslit grating excites surface plasmons that contribute to the transmission of the array. Conversely, when the incident light field is polarized along the slit direction the transmission is weak because of the inability to excite surface plasmons by the grating and the inability to support waveguide modes for that polarization. Despite this complexity, nanoslit arrays have shown promise as high resolution biosensors[34, 35].

This study shows that the placement of nanoparticle chains within the nanoslits of an array act to enhance their transmission significantly over that without nanoparticles. Moreover, it is shown that the maximum wavelength for the transmission may be understood by consideration of the resonant excitation of the localized surface plasmon resonance (LSPR) on the nanoparticles, and the diffractive coupling between the nanoparticles.

4.2 EXPERIMENTAL METHODS

Composite nanoparticle nanoslit arrays (NPNS, Fig. 4.1) were milled into 150nm Au films (with a 3nm Ti adhesion layer) on quartz with a focused ion beam system (Seiko SMI 3050SE). Series of arrays were fabricated with a nominally identical nanoslit geometry, namely a slit width w = 240nm and a length of 20μm. The zeroth order transmission spectra were collected with a microspectrophotometer (CRAIC QDI 2010) that was equipped with a 0.13NA 5x objective, a collimated illumination source (Fiber coupled 75W Xe Arc), and a Glan-Taylor polarizer placed directly below the substrate. The reference for the transmission spectra was a 20μm window milled into the same Au film as the arrays. All arrays were spaced at least 150μm apart in order to ensure that they do not couple with one another. Light was incident on the quartz side of the sample and polarized along the y-axis of the array, i.e., along the nanoslit axis.

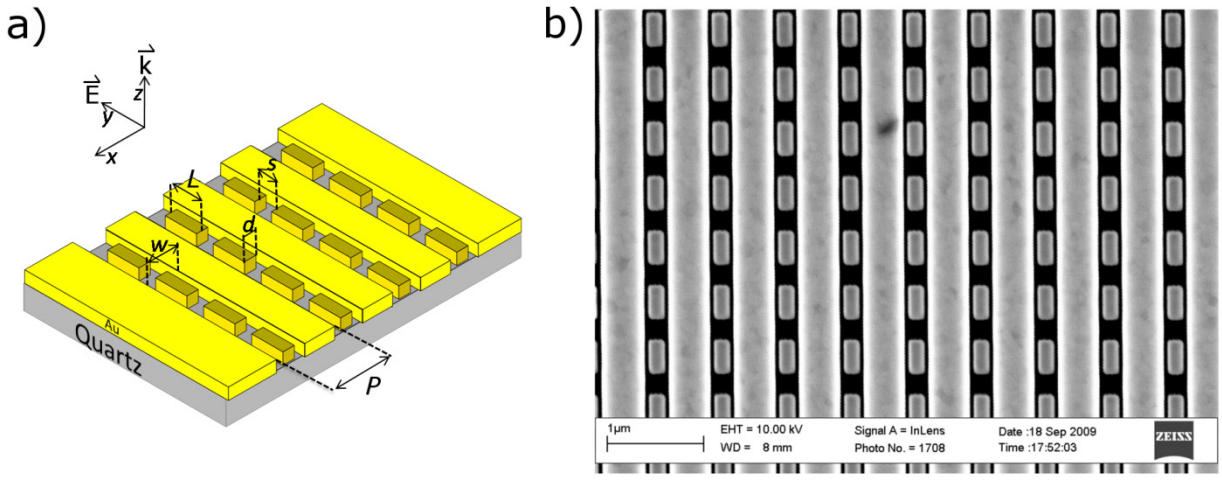

Figure 4.1. a) Diagram of the system under study: a 150nm gold film on quartz with nanoparticle chains nested within a subwavelength nanoslit. Single nanoslits are defined by a width w and fixed spacing P that represents the period of the array. The nanoparticle chains within the slit are defined by a length along the y-axis L and width along the x-axis d. The separation between individual nanoparticles within the chain is defined as s. b) SEM image of a FIB milled nanoparticle/nanoslit array. For the nanoslit: w = 240nm and P = 517nm, and for the nanoparticles: L = 290nm, d = 160nm, s = 210nm.

For a quantitative comparison with the experimental data, composite nanoparticle nanoslit (NPNS) array transmission spectra were simulated by the finite difference time domain (FDTD) method (Lumerical Solutions Inc). For the FDTD simulations the dielectric parameters for Au and Ti were taken from experimental data[36] and fit within the software. The boundary conditions in the plane of the structures (i.e. the x and y direction) were chosen to be symmetric/anti-symmetric. The structure was illuminated from the quartz side, and the transmission was calculated at two different heights above the surface (z = 200nm and z = 3000nm) to ensure that the transmission data are consistent. All of the reported values are from a

distance of 3000nm. The illumination source was modeled as a plane wave with polarization along the *y*-axis (slit direction).

4.3 RESULTS AND DISCUSSION

4.3.1 Role of Nanoparticle Length

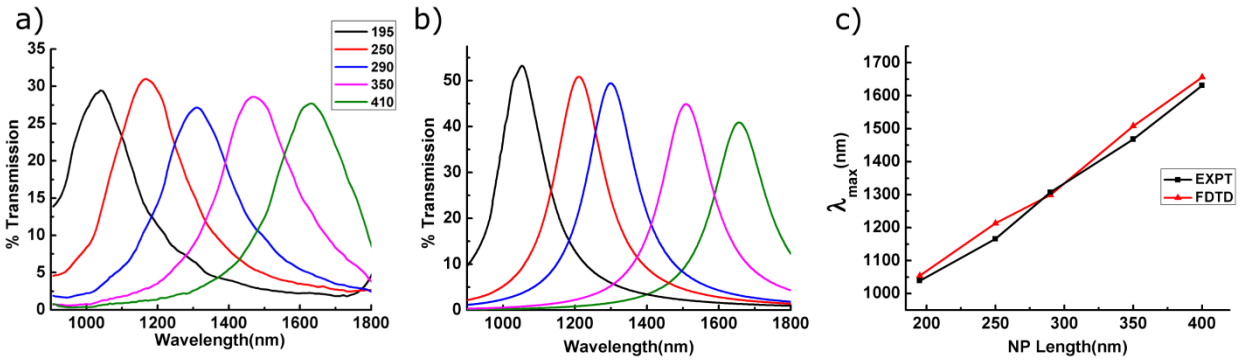

Figure 4.2. a) Experimental and b) FDTD simulated near infrared transmission spectra of NPNS arrays for nanoparticle lengths 195nm to 410nm. The period of the arrays is fixed at 670nm with the spacing between nanoparticles fixed at 210nm. A comparison of λ_{max} at the different nanoparticle lengths between a) and b) is shown in c).

Figure 4.2 shows the transmission spectra of five different NPNS arrays for which the length *L* of the nanoparticle within the nanoslit is varied from 195nm to 410nm. The nanoslit period is fixed at 670nm and the spacing between nanoparticles is fixed at 210nm. Panel a) shows experimental spectra; panel b) shows FDTD simulated spectra; and panel c) shows λ_{max} vs. *L* for both the FDTD and experimental data. Figure 4.2a shows that a nanoparticle with *L* = 410nm has a transmission spectrum with a single, symmetric peak that has a well defined maximum at λ_{max} = 1630nm. As *L* is decreased, λ_{max} blue-shifts and the transmission at λ_{max} is

consistently above 25%. Each individual resonance is relatively broad, and has a FWHM of about 200nm, regardless of the size of the nanoparticle. The essential features of the experimental transmission spectra are reproduced by the FDTD simulated spectra shown in Fig. 4.2b. Namely, a single well defined transmission peak is present and the λ_{max} of the transmission blue-shifts as L decreases. Comparison of the λ_{max} for both the experimental and theoretical spectra, reveals good agreement between experiment and theory and demonstrates the monotonic relationship between L and λ_{max} (Fig 4.2c). Lastly, note that the transmission remains relatively fixed as L is decreased. While the total number of nanoparticles per slit increases as L is decreased, it is unlikely that this accounts for the reduced scattering of each individual nanoparticle. We speculate that this effect arises from the transmission increasing as the nanoparticle resonance approaches the diffraction edge, which, as will be shown in Fig 4.4, can significantly affect the total transmission. Future studies are aimed at better quantifying and understanding this observation.

The relationship between the scattering of nanoparticles and nanoparticle size has been extensively studied for single nanoparticles as well as linear chains and two dimensional arrays (both nanoparticles and nanoapertures)[1, 7, 8, 37-42]. The spectra reported here appear to be the first in which the transmission through subwavelength apertures in an optically thick metal film is controlled by the collective LSPR of noble metal nanoparticle chains nested within a nanoslit. Comparisons of these spectra with those of extinction measurements for both nanoparticle chains and arrays underscores their similarity and suggests that the phenomenology observed with the latter is largely reproduced by the subwavelength transmission through NPNS arrays. Given that the transmission is consistently above 25% for all NP sizes and that the total open area relative to the reference aperture is about 20%, implies that the device is transmitting light through

subwavelength geometries with an efficiency of about unity. It has been shown previously[7, 43] that the FDTD method is reliable for both studying the scattering of subwavelength nanoparticles and the transmission process within nanoaperture arrays, so that the agreement between the FDTD and the experimental spectra should not be surprising. The primary discrepancies between the FDTD and experimental data can be rationalized by the difference between the simulation geometry and imperfections in the FIB milled structure, as well as any experimental error in the measurement.

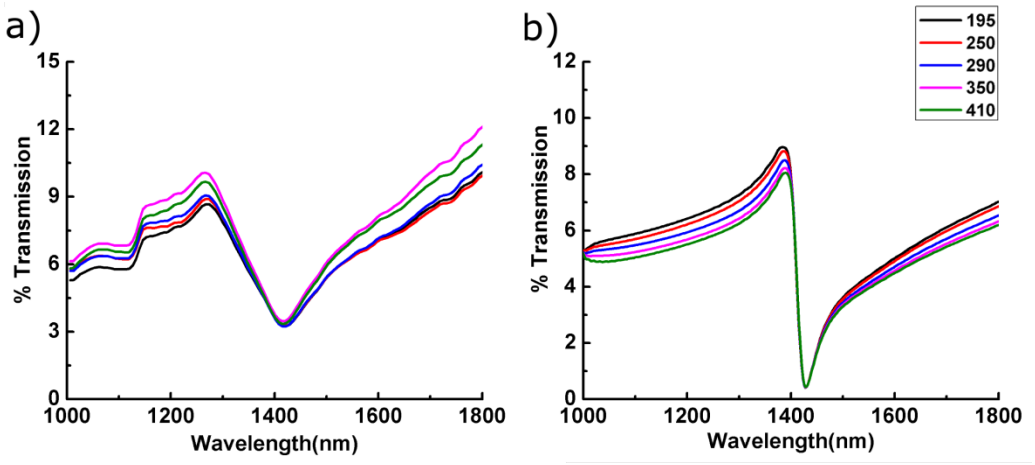

Figure 4.3. a) Experimental and b) theoretical transmission spectra with the incident light polarized along the *x*-axis of the NPNS array for nanoparticle lengths of 195 to 410nm. The period is fixed at 965nm and the spacing between the nanoparticles is 210nm.

Transmission spectra for NPNS arrays in which the incident light is polarized along the *x*-axis of the array are shown in Fig 4.3. For all nanoparticle lengths, the key feature of the transmission in both the FDTD and experimental spectra is a dip in the transmission at λ = 1410nm that corresponds to an Au/SiO_2 Woods anomaly which is given as $\lambda_{woods} = n \bullet P$,

where n is the refractive index of the dielectric (1.45 for SiO_2) and P is the nanoslit period. In contrast to the transmission spectra in Fig 4.2 for y-axis polarization, the features seen here are unremarkable. Since the widths of the nanoparticles are fixed at 160nm, no localized resonances are excited on the nanoparticle within the spectral range studied.

4.3.2 Role of Array Period

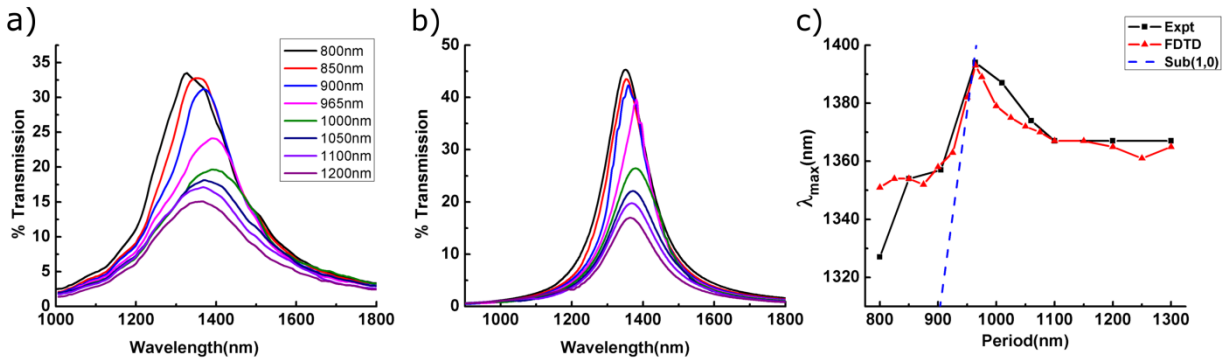

Figure 4.4. a) experimental and b) theoretical transmission spectra as well as c) λ_{max} vs. period of the NPNS arrays with L = 305nm, d = 160nm and s = 210nm. The period of the array is varied from 800nm to 1300nm. Panel a/b display the transmission spectra for P = 800nm to 1300nm, while the plot of λ_{max} vs. period is shown for P = 800nm to 1300nm. The period in c) was incremented in 50nm intervals for both experimental and 25nm for the FDTD. The dashed line represents the light line $\lambda = n_{substrate} \bullet P$.

The role of the nanoslit period in the NPNS transmission is revealed by the data in Fig 4.4, which shows spectra for arrays with L = 305nm and s = 210nm and has the period P varied from 800nm to 1300nm. The experimental transmission spectra (Fig 4.4a) consist of a single transmission resonance whose λ_{max} and peak width change non-monotonically with the period. Initially

for P = 800nm, the transmission is very broad with an overall magnitude of ≈32%. As the nanoslit period is increased up to 900nm, the λ_{max} red shifts and both the magnitude of the transmission as well as the peak width decrease. Above P = 965nm, the magnitude of the transmission continues to attenuate while λ_{max} begins to blue shift and the peak width increases by about 100nm. The transmission spectra calculated by FDTD (Fig 4.4b) show the same trend that is found in the experimental data. For clarity, several transmission spectra were omitted from Fig 4.4b, but they are represented in Fig 4.4c which explores the non-monotonic shift of λ_{max} with the period. The FDTD simulations (Fig 4.4b) show strong qualitative agreement with the experimental data. The key trends noted in the experimental spectra, the decrease in the magnitude of transmission with increasing period and the variation of the peak width and λ_{max}, are present.

The change of λ_{max} with period P is plotted in Fig 4.4c for both experimental and FDTD data, and it illustrates the non-monotonic nature of the wavelength shift with P. From P = 800nm to P = 900nm, the λ_{max} of the experimental spectra red-shifts from λ_{max} = 1327nm to λ_{max} = 1357nm while the FDTD spectra show a weak change of λ_{max} and reasonable agreement with experiment. From P = 900nm to 965nm, both the experimental and FDTD spectra exhibit a strong red-shift that reaches a maximum at P = 965nm. A subsequent increase in the period causes a blue-shift that begins to level off at P = 1100nm whereupon λ_{max} does not change significantly upon further increase in the period up to P = 1300nm. Yet, the λ_{max} remains red-shifted relative to λ_{max} for P= 800nm. In general, variations of λ_{max} with the change in array period are modeled well by the FDTD calculation. The key feature, namely the pronounced red-shift as the period approaches 965nm, followed by a smaller blue-shift for subsequent increases beyond 965nm, appear to be captured in the FDTD simulations.

The observed dependence of the transmission magnitude, the width of the resonance, and the position of λ_{max} on the period P suggests that the transmission through the nanoapertures is primarily caused by the LSPR excitation of the nanoparticles and their coupling effects in both the near and far field. Earlier studies have shown[37, 39, 40, 42, 44-46] that the period of both two dimensional arrays and linear chains of noble metal nanoparticles exhibit spectral changes in the visible that are analogous to those observed here in the near-IR for NPNS arrays. It is believed that the non-monotonic shift of λ_{max} for two dimensional arrays of nanoparticles, which was first predicted by Meier *et al*[47] and later experimentally verified and elaborated upon by Lamprect *et al*[48], is caused by the interaction of lattice modes with light scattered by the nanoparticles as the primary resonance approaches and intersects the light line, $\lambda = n_{substrate} \cdot P$(dashed line, Fig 4.4c). For P = 800nm to 950nm, $\lambda_{max} > \lambda_{light}$ and along the x-axis of the array the nanoparticles are spaced close enough that interactions between their dipole fields are important. The in-phase addition of the dipole fields results in a gradual red-shift which is observed as P is increased. From P = 950nm to 1000nm, λ_{max} intersects λ_{light} and a new diffractive order that radiates at a grazing angle and interacts with the scattered fields of individual nanoparticles emerges and corresponds to the point of maximum red-shift and minimum bandwidth. As the period increases towards P = 1300nm the array enters the regime where $\lambda_{max} < \lambda_{light}$, and the radiative damping of the scattered fields of each nanoparticle within the array increases, causing the increased broadening and the decrease in total transmission.

4.3.3 Role of Nanoparticle Separation

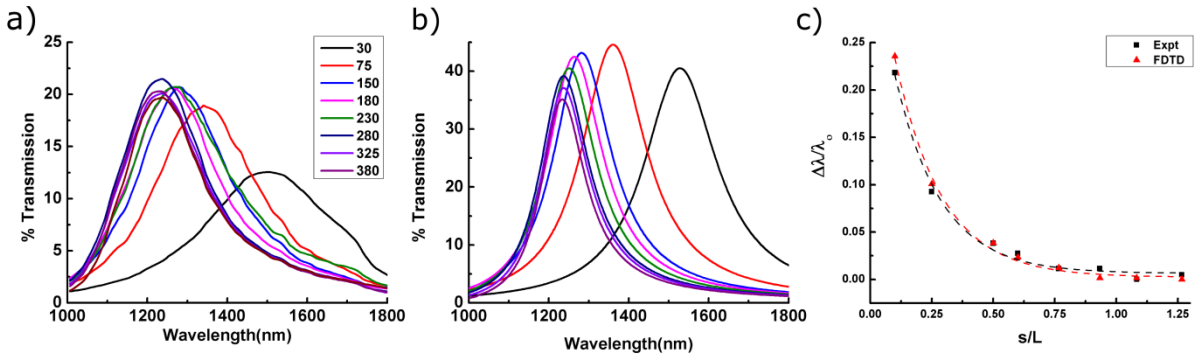

Figure 4.5. a) Experimental and b) FDTD calculated transmission spectra of NPNS arrays in which w = 240nm, P = 650nm, L = 305nm, d = 160nm. The spacing between nanoparticles is varied from 30nm to 360nm for both the experimental and the FDTD data. c) Nanoparticle spacing as a function of $\Delta\lambda/\lambda_o$ for both experimental and theoretical data. The solid line represents the exponential fit of the form $\frac{\Delta\lambda}{\lambda} \approx A * \exp\left(\frac{-\left(\frac{s}{L}\right)}{\tau}\right)$ with $R^2 = 0.99$. For the experimental data A = 0.37 ± 0.02, τ = 0.20 ± 0.02 and for the FDTD data A = 0.39 ± 0.02, τ = 0.19 ± 0.01.

The dependence of the transmission spectra of NPNS arrays on the interparticle spacing is shown in Fig 4.5 and reveals a distinct relationship between λ_{max} and the nanoparticle spacing. Figure 4.5a shows how the experimental spectra change as the nanoparticle spacing changes from s = 30nm to 380nm. For this study the total number of nanoparticles was held constant, and as a consequence, the size of the nanoslit and thus its total open area decreases significantly for small values of s. To an extent, this decrease can account for the reduced transmission seen for s = 30nm. From s = 30nm to s = 70nm, the λ_{max} shifts by 155nm from 1502nm to 1347nm. Subsequent increases in s result in further reductions of λ_{max}; as s approaches 230nm, the shift in

λ_{max} becomes minimal. In addition to λ_{max}, these data reveal that the width of the transmission peak depends on *s*, namely, it decreases about 150nm from *s* = 30nm to *s* = 380nm. The increase in peak width is probably caused by the decrease in LSPR lifetime which reflects the interaction and subsequent coupling between the nanoparticles as *s* is decreased. Other than the noticeable difference in transmission magnitude, which arises from the failure of FDTD calculations to account for the change in nanoslit length as the spacing is reduced while keeping the total number of nanoparticles constant, the FDTD simulated spectra show good agreement with the experimental spectra.

Numerous studies have characterized how the optical response of nanoparticles changes with distance between the individual nanoparticles[8, 49], both in solution[23] and affixed on substrates in ordered arrays, chains, and pairs. For electrostatic dipolar coupling between two nanoparticles one expects a d^{-3} dependence of the plasmon shift with the interparticle distance. Jain *et al*[22] showed that at short nanoparticle separations, an exponential function of the form

$$\frac{\Delta\lambda}{\lambda} \approx A * \exp\left(\frac{-\left(\frac{S}{L}\right)}{\tau}\right) \qquad (4.1)$$

can be used to approximate the dependence of the plasmon resonance coupling between the nanoparticles on the distance *s*, where $\frac{\Delta\lambda}{\lambda}$ is the fractional wavelength shift relative to an uncoupled nanoparticle, *A* is the amplitude of the decaying field, *s* is the center to center distance between nanoparticles, *L* is the length of an individual nanoparticle, and τ is a characteristic decay constant. Recently Funston *et al*[21] demonstrated that this model breaks down for situations in which $s/L < 0.09$. In the context of NPNS arrays (Fig 4.5c), it is clear that the transmission resonance shift with the interparticle spacing can be fit by an exponential function, akin to the plasmonic ruler equation. A fit of the experimental data to this model gives values of $\tau = 0.2$

and $A = 0.37$, which fall within the range expected for much smaller nanoparticles, indicating that the length of the dipole coupling between the nanoparticles is within the same regime as that of sub 100nm spherical Au nanoparticles. Note that these fitting parameters are sensitive to the minimum spacing achieved between the nanoparticles, which arises from the resolution limits of the focused ion beam system and was 30nm. Indeed, by taking the separation to be 15nm in the FDTD simulations and fitting those data, one finds fitting parameters of $\tau = 0.06$ and $A = 3.35$(data not shown). These considerations suggest that not only does dipolar coupling influence the subwavelength transmission, but that in the regime where $s/L < 0.5$ the device exhibits remarkable sensitivity to the spacing between nanoparticles. This finding could have implications not only in tailoring the transmission resonances of plasmonic devices but in the rational design of plasmonic ruler based sensors.

4.4 SUMMARY

In summary it was shown that focused ion beam fabricated nanoparticle chains within a subwavelength nanoslit array are capable of subwavelength transmission that is modulated through LSPR based interactions. It was found that by varying the size of the nanoparticle within the nanoslit the maximum transmission wavelengths could be tuned. The response of the NPNS arrays to changes in the period resulted in a non-monotonic shift of the position of λ_{max}, which was correlated to a change in the nature of the nanoparticles coupling from an evanescent to far-field radiative mode of the grating. Lastly, the position of λ_{max} showed a strong dependence upon the spacing between nanoparticles within the nanoslit. It was shown that λ_{max} red-shifts significantly as the spacing between nanoparticles drops below 100nm, and the relative shift in

λ_{max} as the spacing changed for a fixed nanoparticle size could be fit to an exponential decay function in a manner analogous to the plasmon ruler equation. Given the great interest in localizing and controlling the propagation of light through a noble metal nanostructure, these findings have significant implications for the design and utilization of transmission based plasmonic devices in numerous areas of study.

Acknowledgements: This work was funded by NASA (NNX09CB64C), NSF (CHE-0404579) and NSERC (BiopSys). The authors would like to thank Jianjun Wei for helpful discussions and Michael McDonald at the Peterson Institute for Nanoscience and Engineering for nanofabrication technical support/

4.5 REFERENCES

1. S. K. Ghosh and T. Pal, Chemical Reviews **107** (11), 4797-4862 (2007).
2. K. L. Kelly, E. Coronado, L. L. Zhao and G. C. Schatz, The Journal of Physical Chemistry B **107** (3), 668-677 (2002).
3. K. A. Willets and R. P. Van Duyne, Annual Review of Physical Chemistry **58** (1), 267-297 (2007).
4. H. F. Ghaemi, T. Thio, D. E. Grupp, T. W. Ebbesen and H. J. Lezec, Physical Review B **58** (11), 6779-6782 (1998).
5. W. L. Barnes, A. Dereux and T. W. Ebbesen, Nature **424** (6950), 824-830 (2003).
6. C. Genet and T. W. Ebbesen, Nature **445** (7123), 39-46 (2007).
7. A. A. L. G.C. Schatz, and K.L. Kelly, Abstr Pap Am Chem S **224**, U298-U298 (2002).

8. C. L. Haynes, A. D. McFarland, L. Zhao, R. P. Van Duyne, G. C. Schatz, L. Gunnarsson, J. Prikulis, B. Kasemo and M. Käll, The Journal of Physical Chemistry B **107** (30), 7337-7342 (2003).

9. P. K. Jain and M. A. El-Sayed, The Journal of Physical Chemistry C **112** (13), 4954-4960 (2008).

10. L. L. H. S.L. Zou, N. Janel, and G.C. Schatz, Abstr Pap Am Chem S **227**, U266-U266 (2004).

11. C. Tabor, R. Murali, M. Mahmoud and M. A. El-Sayed, The Journal of Physical Chemistry A **113** (10), 1946-1953 (2008).

12. S. Zou, N. Janel and G. C. Schatz, The Journal of Chemical Physics **120** (23), 10871-10875 (2004).

13. S. Zou and G. C. Schatz, The Journal of Chemical Physics **121** (24), 12606-12612 (2004).

14. M. Salerno, J. R. Krenn, A. Hohenau, H. Ditlbacher, G. Schider, A. Leitner and F. R. Aussenegg, Optics Communications **248** (4–6), 543-549 (2005).

15. S. A. Maier, P. G. Kik, H. A. Atwater, S. Meltzer, E. Harel, B. E. Koel and A. A. G. Requicha, Nat Mater **2** (4), 229-232 (2003).

16. V. E. Ferry, L. A. Sweatlock, D. Pacifici and H. A. Atwater, Nano Letters **8** (12), 4391-4397 (2008).

17. C. Hagglund, M. Zach and B. Kasemo, Appl Phys Lett **92** (1), 013113-013113 (2008).

18. J. Ferreira, M. J. L. Santos, M. M. Rahman, A. G. Brolo, R. Gordon, D. Sinton and E. M. Girotto, Journal of the American Chemical Society **131** (2), 436-437 (2008).

19. A. J. Haes, L. Chang, W. L. Klein and R. P. Van Duyne, Journal of the American Chemical Society **127** (7), 2264-2271 (2005).

20. W. P. Hall, J. N. Anker, Y. Lin, J. Modica, M. Mrksich and R. P. Van Duyne, Journal of the American Chemical Society **130** (18), 5836-5837 (2008).

21. A. M. Funston, C. Novo, T. J. Davis and P. Mulvaney, Nano Letters **9** (4), 1651-1658 (2009).

22. P. K. Jain, W. Huang and M. A. El-Sayed, Nano Letters **7** (7), 2080-2088 (2007).

23. Y.-w. Jun, S. Sheikholeslami, D. R. Hostetter, C. Tajon, C. S. Craik and A. P. Alivisatos, Proceedings of the National Academy of Sciences **106** (42), 17735-17740 (2009).

24. M. E. Stewart, J. Yao, J. Maria, S. K. Gray, J. A. Rogers and R. G. Nuzzo, Analytical Chemistry **81** (15), 5980-5989 (2009).

25. Q. Cao and P. Lalanne, Physical Review Letters **88** (5), 057403 (2002).

26. S. Collin, F. Pardo, R. Teissier and J. L. Pelouard, Physical Review B **63** (3), 033107 (2001).

27. Y. S. Jung, J. Wuenschell, H. K. Kim, P. Kaur and D. H. Waldeck, Opt. Express **17** (18), 16081-16091 (2009).

28. Y. S. Jung, Y. Xi, J. Wuenschell and H. K. Kim, Opt. Express **16** (23), 18881-18888 (2008).

29. P. Lalanne, J. P. Hugonin and J. C. Rodier, Physical Review Letters **95** (26), 263902 (2005).

30. K. G. Lee and Q. H. Park, Physical Review Letters **95** (10), 103902 (2005).

31. Y. Takakura, Physical Review Letters **86** (24), 5601-5603 (2001).

32. B. Wang and P. Lalanne, Appl Phys Lett **96** (5), 051115-051113 (2010).

33. J. Wuenschell and K. Hong Koo, Nanotechnology, IEEE Transactions on **7** (2), 229-236 (2008).

34. Y. S. Jung, Z. Sun, J. Wuenschell, H. K. Kim, P. Kaur, L. Wang and D. Waldeck, Appl Phys Lett **88** (24), 243105-243103 (2006).

35. K.-L. Lee, C.-W. Lee, W.-S. Wang and P.-K. Wei, Journal of Biomedical Optics **12** (4), 044023-044025 (2007).

36. P. B. Johnson and R. W. Christy, Physical Review B **6** (12), 4370-4379 (1972).

37. E. M. Hicks, S. Zou, G. C. Schatz, K. G. Spears, R. P. Van Duyne, L. Gunnarsson, T. Rindzevicius, B. Kasemo and M. Käll, Nano Letters **5** (6), 1065-1070 (2005).

38. M. J. Kofke, D. H. Waldeck, Z. Fakhraai, S. Ip and G. C. Walker, Appl Phys Lett **94** (2), 023104-023103 (2009).

39. A. Pinchuk and G. Schatz, Applied Physics B: Lasers and Optics **93** (1), 31-38 (2008).

40. J. Sung, E. M. Hicks, R. P. Van Duyne and K. G. Spears, The Journal of Physical Chemistry C **112** (11), 4091-4096 (2008).

41. S. Wu, Q.-j. Wang, X.-g. Yin, J.-q. Li, D. Zhu, S.-q. Liu and Y.-y. Zhu, Appl Phys Lett **93** (10), 101113-101113 (2008).

42. L. Zhao, K. L. Kelly and G. C. Schatz, The Journal of Physical Chemistry B **107** (30), 7343-7350 (2003).

43. K. L. Shuford, M. A. Ratner, S. K. Gray and G. C. Schatz, Applied Physics B: Lasers and Optics **84** (1), 11-18 (2006).

44. B. Auguié and W. L. Barnes, Physical Review Letters **101** (14), 143902 (2008).

45. A. Bouhelier, R. Bachelot, J. S. Im, G. P. Wiederrecht, G. Lerondel, S. Kostcheev and P. Royer, The Journal of Physical Chemistry B **109** (8), 3195-3198 (2005).

46. J. Sung, E. M. Hicks, R. P. Van Duyne and K. G. Spears, The Journal of Physical Chemistry C **111** (28), 10368-10376 (2007).

47. M. Meier, A. Wokaun and P. F. Liao, J. Opt. Soc. Am. B **2** (6), 931-949 (1985).

48. B. Lamprecht, G. Schider, R. T. Lechner, H. Ditlbacher, J. R. Krenn, A. Leitner and F. R. Aussenegg, Physical Review Letters **84** (20), 4721-4724 (2000).

49. W. Rechberger, A. Hohenau, A. Leitner, J. R. Krenn, B. Lamprecht and F. R. Aussenegg, Optics Communications **220** (1–3), 137-141 (2003).

5.0 SELF-ASSEMBLED MONOLAYERS AS TEMPLATES FOR SEEDLESS SURFACTANT MEDIATED SYNTHESIS OF NOVEL ANISOTROPIC NANOPARTICLES AND NANOPARTICLE CLUSTERS

The thesis author performed device fabrication and experimental analysis for all the devices studied.

5.1 INTRODUCTION

A seedless method for the synthesis of novel noble metal nanostructures, which employs alkanethiol self-assembled monolayer functionalized submicron apertures or surface bound colloidal nanoparticles as a template, has been developed. The method uses surfactant mediated anisotropic Au nanoparticle synthesis with cetyltrimethylammonium bromide (CTAB), and the results suggest that the interaction between CTAB and the alkanethiol monolayer template surface has a significant influence on the process. Nanoparticle nucleation and growth is found to depend on the chain length of the alkanethiol, with short chain SAMs showing little nanoparticle growth. The functional group of the SAM is shown to significantly affect the shape and geometric configuration of nanoparticles within the aperture. The addition of shape directing ions Ag^+ and I^- to the growth solution induced concentration dependent morphological

changes. When applied to 80nm Au nanoparticles immobilized on an ITO surface, this methodology resulted in oligomeric Au nanostructures with asymmetric geometries and separations on the order of the SAM thickness. In order to highlight the wide ranging applicability of this approach, Ag and Pd nanoparticles were grown within 200nm apertures also, and they displayed novel nanostructured features that were distinct from those of Au.

Subwavelength apertures, diameters < λ/2 of the incident light, in thin gold films have been studied extensively since the work of Ebbesen and coworkers[1] demonstrated the extraordinary optical transmission phenomena for a two dimensional array of subwavelength apertures in metal films. Studies of individual subwavelength apertures have elucidated both the electrodynamics[2, 3] of the structures, as well as shown the promise of these nanostructures for SERS[4]. Modifying the aperture, either by deposition of colloidal nanoparticles or fabricating apertures with optically resonant nanostructures nested inside[5], has extended the utility of these structures for single molecule spectroscopy studies[6]. Yet, preparation methods, which use nanoapertures as a scaffold to synthesize a nanoparticle / nanoaperture assembly, with novel optical properties, are lacking.

Anisotropic noble metal nanoparticles have garnered significant academic interest[7, 8] in recent years because of the variety of shapes that can be arbitrarily synthesized by changing reaction conditions, as well as for their potential applications in biosensing[9], surface enhanced Raman scattering (SERS)[10], live cell imaging[11, 12], and optoelectronics[13]. Methods that use the cationic surfactant cetyltrimethylammonium bromide (CTAB) have been developed and provide a wide variety of anisotropic structures for Au, Ag, and Pd nanomaterials. These developments have provided insight into the mechanisms for crystal growth and shape directing effects, as well. Typically, the introduction of ions such as Ag^+ or I^- in controlled amounts to the growth

solution strongly affects the resultant structures and in the case of nanorods, result in near 100% nanorod yield[14]. A common approach in all of these methods is to initiate the reaction by introducing small seeds because the typical reducing agent ascorbic acid (AA) is unable to fully reduce Au^{3+} to elemental Au in the presence of CTAB. To date there have been few reported[15, 16] synthetic methods for room temperature seedless CTAB mediated noble metal nanoparticle growth in aqueous media.

This work utilizes CTAB mediated Au nanoparticle synthetic methods to prepare novel anisotropic structures within 200 nm diameter nanoapertures. The nanoapertures were formed in 30nm thick gold films through colloidal lithography[17], and they were functionalized with alkanethiol self-assembled monolayers(SAMs). SAMs were grown from 1mM ethanoloic solutions of alkanethiols with incubation times lasting from 20 – 24h. We show that these nanoapertures are able to function as scaffolds that direct the seedless nucleation and growth of novel plasmonic nanostructures and that their chain length and terminal head functional group affect the final nanoparticle / nanoaperture assembly's structure. In order to understand better how the Au film surface and solution environment affect the final structure, systematic studies were conducted that vary both the nanoparticle growth solution conditions as well as the nature of the self-assembled monolayer. Variations of both the alkanethiol film composition (chain length and functional groups) and the nature of the shape directing ions (Ag^+ or I^-) are shown to play a significant role in the outcome of the nanostructure formation, but in a way that is strikingly dissimilar to those reported for solution based anisotropic nanoparticle synthesis. Lastly, silver and palladium nanoparticles were grown within the Au film nanoapertures by replacing the gold precursor salt with either silver or palladium precursors in the growth solution.

This latter result shows that any metal precursor / CTAB complex that has been shown to yield anisotropic nanoparticles can be extended to these systems.

This methodology was also applied to spherical Au nanoparticles that are immobilized on an ITO substrate. For this system the Au nanoparticles act as templates for the formation of Au nanoparticle heteroaggregates with integrated nanoscale gaps. In this case the alkanethiol template directs the assembly so that growths of the nanoparticles conform to the geometry of the Au nanoparticle template. This method serves as a route towards generating novel nanostructures in spectroscopically interesting configurations.

The studies reported herein demonstrate, for the first time, a simple and straightforward method to modify an alkanethiol functionalized plasmonic structure by using well known anisotropic metal nanoparticle synthetic methods without the use of seeds to initiate nanoparticle nucleation and growth. This method is demonstrated for a variety of metal (Au, Ag and Pd) nanoparticle systems both upon plasmonic nanoapertures in a thin gold film and upon 80nm colloidal nanoparticles immobilized on a transparent substrate. The resultant nanoparticle structures appear to derive their shape from the contour of the template structures. The additions of ions, known to direct the nanoparticle shape in solution, affect the morphology of the nanoparticle structure but not the final shape of the nanoparticle. This finding may provide an opportunity for understanding better the growth mechanism behind non-spherical metal nanoparticles, as well as lead to the development of novel functional plasmonic devices and nanoparticle geometries.

5.2 EXPERIMENTAL METHODS

Au nanoaperture fabrication: Nanoapertures were fabricated by using hole-mask colloidal lithography. A 1mm thick glass microscope slide (VWR) was cleaned with piranha solution (1:3 H_2O_2 / H_2SO_4, CAUTION: piranha solution reacts violently with organic material, handle with care) for 10 minutes and subsequently rinsed with ultrapure H_2O and dried under nitrogen. Immediately following piranha cleaning, the slides were immersed in a solution consisting of polydiallyldimethylammomium chloride (PDDA, MW 500,000, Aldrich) and 0.1M NaCl for 30 minutes to deposit a thin positively charged film on the surface. After incubation the slides were thoroughly rinsed with ultrapure H_2O and dried under nitrogen. The PDDA modified slides were next placed for 3 minutes in a solution of sulfate modified polystyrene microspheres (Polysciences Inc) which contained 0.01% solids in ultrapure water and then rinsed with ultrapure H_2O and dried under nitrogen. A 3 nm thick titanium adhesion layer followed by a 30 nm thick gold film was deposited onto the slides by e-beam evaporation. Following deposition the polystyrene microspheres were removed with wafer tape. This process produced 200 nm average diameter nanoapertures within the Au film that were distributed in a random pattern.

Colloidal Au nanoparticle immobilization: Eighty nanometer diameter citrate capped Au nanoparticles (Ted Pella) were immobilized onto an ITO coated microscope slide (Delta Technologies Inc.). Initially the slides were ultrasonically cleaned in isopropanol for 30 minutes and then dried under an N_2 gas stream. Next the slides were oxygen plasma cleaned (100W, 200mT, 50sccm) and then placed in a 1% w/w aqueous solution consisting of polyallylamine (PAH, MW 15000, Aldrich) and 0.1M NaCl for 30 s, rinsed with ultrapure water, and then dried under an N_2 gas stream. The Au nanoparticle solution was centrifuged to increase the

concentration tenfold. A drop of this solution was placed on the PAH modified ITO slides for 30 minutes in a humidity chamber, rinsed with ultrapure H_2O, and dried under an N_2 gas stream.

Formation of alkanethiol self-assembled monolayers: Octadecanethiol, dodecanethiol, octanethiol, pentanethiol, mercaptoundecanoic acid, mercaptoundecanol, and mercaptoundecylamine hydrocholoride were purchased from Aldrich for self-assembly of alkanethiol films on Au. The alkanethiol was dissolved in ethanol (1mM or 0.5 mM for COOH or NH_2 functionalized) and the nanoaperture or nanoparticle substrates were incubated for 20-24 hours in the solution. Subsequent to incubation, the substrates were rinsed with ethanol and then dried under and N_2 stream.

Metal nanoparticle synthesis: 1.0 mL CTAB (100mM), 100µL $HAuCl_4$ (10mM), and ultrapure H_2O (1.0 mL) were combined and briefly stirred until the solution turned light brown. At this stage any additional salts which were to be used (such as $AgNO_3$ or KI), were added to the solution. Ascorbic acid (33µL of a 200mM solution) was added and the reaction mixture was hand stirred until clear. Next 20µL was transferred to the alkanethiol passivated nanoapertures (or nanoparticles) substrate and left to incubate for 30 minutes in a humidity chamber at 32^{o}C, rinsed with H_2O, and then dried under an N_2 gas stream. For Ag and Pd nanoparticle synthesis, 100µL of $AgNO_3$ or H_2PdCl_2 (100mM) was used instead of $HAuCl_4$; in each such case 100µL of NaOH (1.0 M) was added to the growth solution. Pd nanoparticles were synthesized with the substrate completely immersed in the growth solution at 70^{o}C

Characterization: Samples were characterized by SEM and UV-Vis extinction spectroscopy. SEM images were acquired on a Raith E-line e-beam lithography instrument at 10kV. Extinction measurements were taken on a CRAIC microspectrophotometer equipped with a 15x reflecting objective. The spectral range was 400nm – 1500nm with a resolution of 0.8 nm

from 400 - 900nm and 6.0 nm from 900 – 1500nm. For nanoapertures, the extinction was referenced against unreacted regions of the sample; for nanoparticles the reference was regions without any nanoparticles.

5.3 RESULTS AND DISCUSSION

5.3.1 Effect of Au^{3+} Concentration

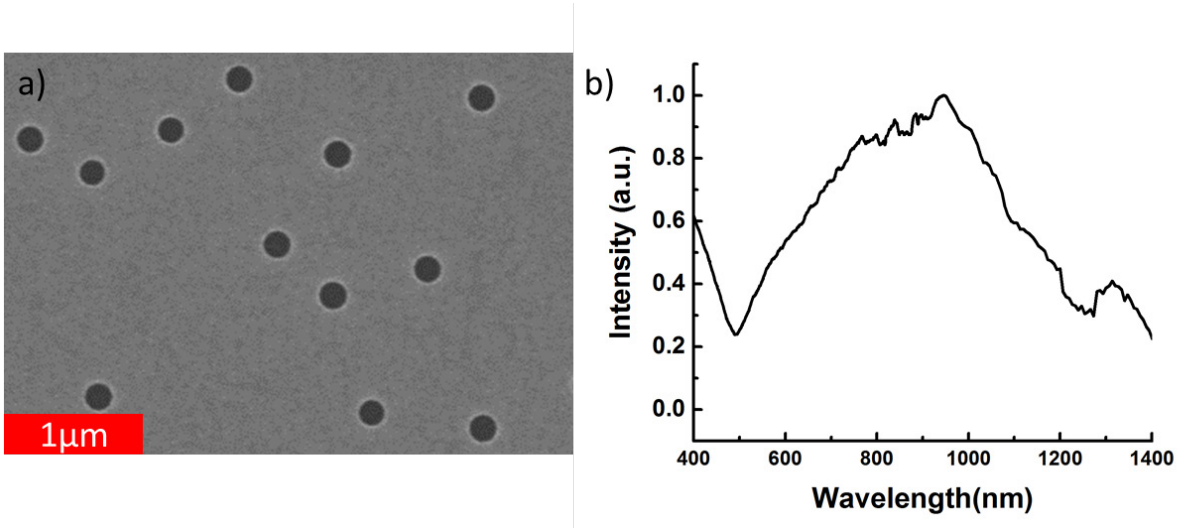

Figure 5.1. Panel a) shows a SEM image of the unmodified nanoaperture template used in this study: randomly distributed 200nm average diameter nanoapertures in a 30nm thick Au film. The corresponding dark field scattering spectra is shown in panel b).

For these studies 200 nm diameter apertures (figure 5.1a) were fabricated onto quartz microscope slides using nanosphere lithographic methods that were adapted from Mirin and coworkers[18] with minor modifications to minimize deposition of nanosphere aggregates onto the substrate. In this procedure 200 nm polystyrene sulfate nanospheres were attached to the substrate by electrostatic attraction to a polydiallyldimethylammomium chloride (PDDA) cationic polymer film that had been previously adsorbed to the surface. The nanospheres serve as negative masks upon which a 30nm thick film of Au metal was deposited via electron beam evaporation. Following Au deposition the nanospheres were removed with wafer tape, leaving 200 nm average diameter holes in the Au film that are randomly distributed on the surface. To remove the residual PDDA polymer in the base of the aperture as well as any organic residue from the

wafer tape, the samples were exposed to 50W oxygen plasma for 60 seconds. The Au surface was passivated with an alkanethiol self-assembled monolayer by exposing it to a 1mM ethanolic solution of octadecanethiol for 20 – 24 hours. The dark field scattering spectra are shown for the unmodified nanoapertures (Figure 5.1b) and in general the optical response of the system is very broad, with the extinction due to the nanoaperture plasmon ranging from λ = 500nm - 1400nm.

Gold nanostructures were grown within the alkanethiol passivated nanoapertures using a CTAB / Au nanoparticle growth procedure modified in order to allow probing of various reaction conditions, such as ion concentration, whilst minimizing substrate use. A 20 μL drop that contained 47 mM CTAB, 3 mM ascorbic acid, and $HAuCl_4$ at concentrations ranging from 117μM – 936 μM was placed on the substrate and left to incubate for at least 30 minutes in a humidity chamber to minimize growth solution evaporation. The total growth area on the substrate from the 20μL drop was approximately 28mm^2, corresponding to a 3mm radius circle. The incubation times were purposely left short to ensure the barrier properties of the hydrophobic SAM, which have been shown to breakdown for long exposures to aqueous solutions[19], were maintained. Using a single drop allowed multiple experiments to be performed on the same substrate to minimize substrate induced variability. At the end of the incubation period the drop was rinsed away with ultrapure H_2O and the sample was dried under a stream of nitrogen gas.

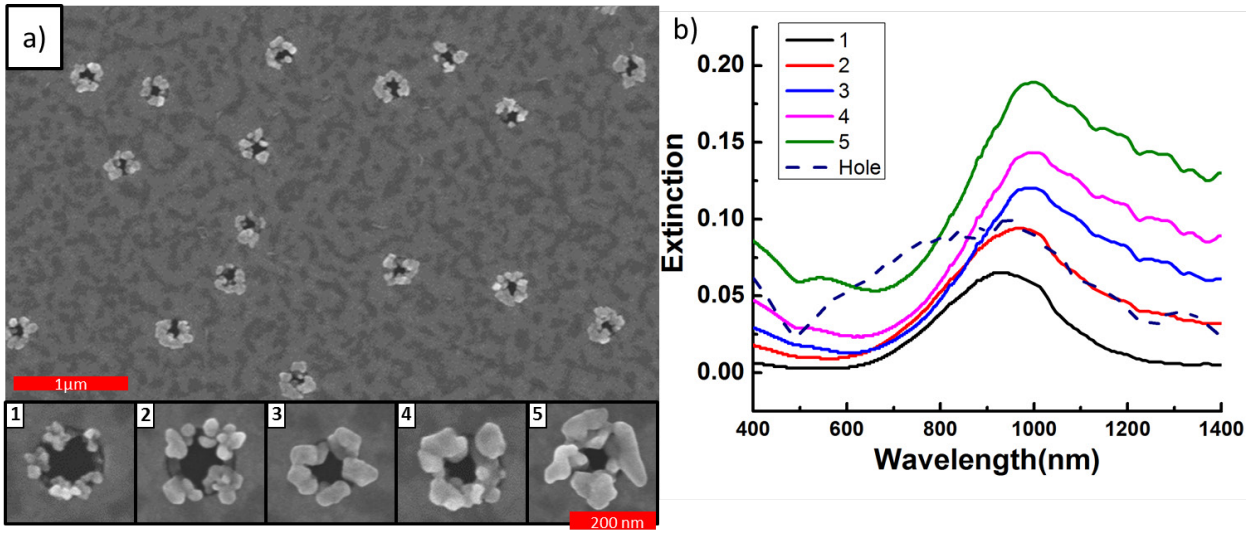

Figure 5.2. Panel a) shows SEM images of Au nanoparticle clusters that were synthesized upon 200nm diameter apertures in a 30nm thick Au film modified with an octadecanethiol self-assembled monolayer. Inset SEM images 1 – 5 show representative aperture / nanoparticle clusters at higher SEM magnification for different concentrations of Au^{3+} ranging from 1: 117µM, 2: 234µM, 3: 468µM, 4: 702µM, and 5: 936µM. Panel b) shows the corresponding extinction spectra, and for a point of reference, the dashed navy blue line for dark field scattering spectra of the unmodified Au nanoholes (Fig 5.1b) is overlaid.

The effect of conducting the CTAB/Au nanoparticle synthesis upon an octadecanethiol functionalized 30nm thick Au film with 200nm average diameter nanoapertures is shown in figure 5.2. The SEM image in Figure 5.2 panel a) shows that non-spherical nanoparticles grow at the edge of the aperture. The growth of the nanostructures inwards towards the center of the aperture and outwards past the sidewall of the aperture suggests that nanoparticles within the nanostructure can extend above the height of the nanoaperture. The observed nucleation and growth of the Au nanoparticles within the nanoapertures is a surprising result because no seeds

were present either in the growth solution or bound to the surface of the octadecanethiol monolayer. This observation suggests that the octadecanethiol functionalized Au film / solvent interface itself enables nanoparticle nucleation and growth. The SEM images also reveal that the nanostructures within each individual nanoaperture have no preferred orientation or morphology, and that the nanostructure nucleation and growth is restricted to the nanoaperture and does not occur on the SAM coated top surface. It is apparent there is organic material present on the surface of the Au film, which is denoted by the dark grey patches observed throughout the image. This feature appears to arise from the alkanethiol functionalization and the incubation with the growth solution, however it can be fully removed by oxygen plasma cleaning after the nanoparticle growth.

The effect of aurate ion concentration, $[Au^{3+}]$, on the NP-aperture nanostructures was explored systematically. The inset SEM images of magnified individual nanoapertures (Figure 5.2a, inset images 1 – 5) were obtained for five different Au^{3+} concentrations, from 117 μM (panel 1) to 936 μM (panel 5). These images reveal several morphological changes to the individual nanoparticles and the nanoparticle clusters in the nanoaperture with Au^{3+} concentration. Panels 1 and 2 show that doubling the Au^{3+} concentration from 117 μM to 234 μM increases the overall size of both the nanoparticles and nanoparticle clusters within the nanoaperture. As the Au^{3+} concentration is increased to 468 μM (panel 3), it appears that the overall size of the nanoparticles within the nanoaperture increase and extend both towards the center of the aperture and beyond the sidewall. The total density of features within the aperture seems to decrease with the increasing feature size of the nanoparticles. The nanostructure consists of a ring of Au nanoparticles which appear to originate at the sidewall of the nanoaperture and have random orientations. This trend continues for subsequent increase in

[Au^{3+}], as seen in panels 4 and 5, until the aperture is almost fully occluded by the Au nanoparticle-ring structure. Thus, increasing the aurate ion concentration increases the overall volume of the nanoparticle-ring structure that grows within the aperture; also it increases the nanoparticle feature size, but decreases the total nanoparticle density.

Figure 5.1 b) shows extinction data, collected with a CRAIC microspectrophotometer in transmission mode, for the nanoparticles grown in the apertures at various [Au^{3+}]. The spectra were taken over a 100μm x 100μm area which encompasses roughly 5500 nanoapertures, and shows a single, very broad peak (300 nm FWHM) in the NIR that extends from 600 nm to 1300 nm for nanoparticles corresponding to 117μM [Au^{3+}]. As the concentration of Au^{3+} increases, the magnitude of the extinction increases with approximately a 100 nm redshift of the $\lambda_{max.}$ The shape of the peak appears to become more asymmetric, tailing off into the Near-IR as [Au^{3+}] increases. The overall increase in extinction and slight redshift can be attributed to an increase in the total volume of the nanoparticles / nanoparticle clusters within the nanoaperture. Relative to the unmodified nanoapertures, the optical signal is shifted further into the Near-IR, however there still is significant overlap. It is likely that the spectra represent the collective extinction (absorbance + scattering) from both the nanostructure nested within the aperture, localized resonances supported on the nanoscale morphological features that become more pronounced with increased [Au^{3+}], and the nanoaperture resonance which would be red-shifted relative to the reference apertures due to the presence of the nanoparticle-ring structure in the nanoaperture.

5.3.2 Effect of Ag^+ and I^- Addition

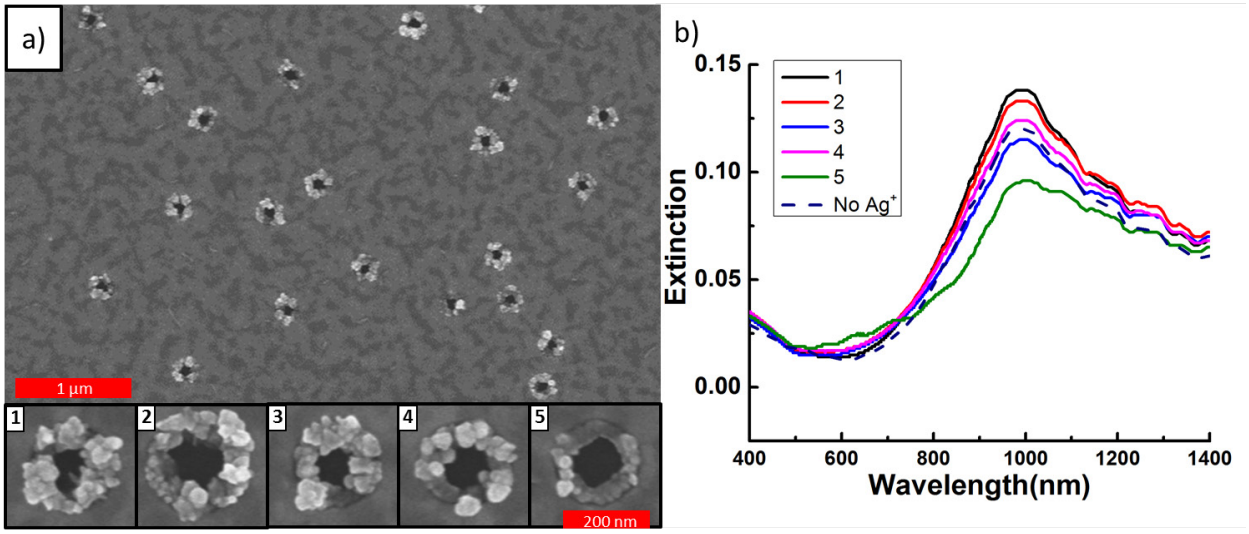

Figure 5.3. Panel a) shows SEM images of ring-like Au nanoparticle nanostructures within 200nm diameter nanoapertures grown with an Ag:Au molar ratio of 1:10. The inset SEM images of magnified individual nanoapertures are for Ag:Au molar ratio of 1) 1:50, 2) 1:20, 3) 1:10, 4)1:5, and 5) 1:1. Panel b) shows the corresponding extinction spectra with the dashed navy blue line representing the nanostructures grown without any Ag^+ ions present in the growth solution.

The effect of the shape directing ion Ag^+ on the CTAB/Au nanoparticle growth was investigated. For these studies the molar ratio of Ag^+ to Au^{3+} in the growth solution was varied and the resultant SEM and extinction data was collected (Figure 5.3). The SEM image in figure 5.3 a) was taken for a 1:10 Ag^+/Au^{3+} molar ratio and shows individual nanoapertures which appear to contain nanoparticle-rings in which the nanoparticles are still randomly oriented but appear to have more distinct features than those observed for the CTAB/Au nanostructures without Ag^+. The inset shows SEM images of magnified individual nanoapertures at different Ag^+ / Au^{3+}

molar ratios. It is evident that small amounts of Ag^{+} (9.4 μM for the 1:50 ratio, inset panel 1) yields a dramatic change in the resulting structure and the expected shape directing effects seen for seed mediated synthesis of nanoparticles in the presence of Ag^{+} are not present. The concentration of Ag^{+} was controlled so that the ratio of Ag^{+}:Au^{3+} ranged from 1:50 (see SEM image in panel 1) to 1:1 (see SEM image in panel 5). The typical Ag^{+}:Au^{3+} ratio used for nanorod growth in solution is 1:5; an SEM image for this ratio is shown in panel 4. As the concentration of Ag^{+} is increased it appears that the density of the nanoscale features on the nanostructure are reduced and at a 1:1 Ag^{+} / Au^{3+} ratio the nanostructure appears as a single ring with few nanoscale morphological features. Extinction data for the Ag^{+} directed reactions shows a single asymmetric peak with a ~600nm bandwidth, as without Ag^{+}. The lack of new features or a systematic trend in the extinction with changing Ag^{+}:Au^{3+} ratio indicates that the Ag^{+} induced changes in the nanostructure morphology do not significantly alter the average optical response of the system.

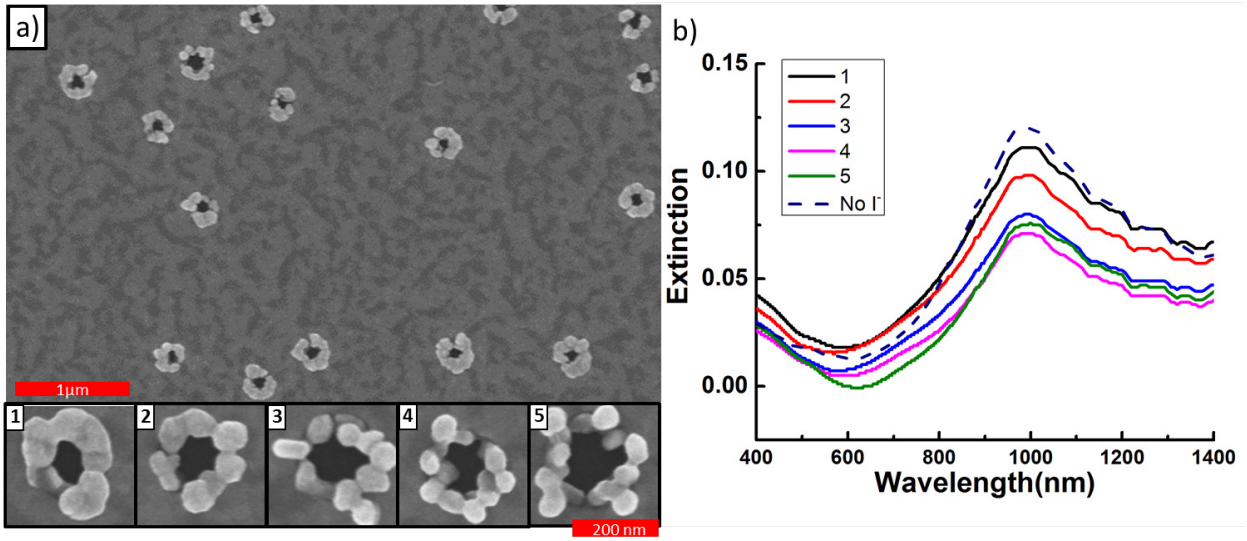

Figure 5.4. SEM image of ring-like Au nanoparticle nanostructures within 200nm diameter nanoapertures grown with 5μM I^- present in the growth solution are shown in panel a). The inset SEM images of magnified individual nanoapertures are for [I^-] of 1) 5 μM, 2) 10 μM, 3) 25 μM, 4)75 μM, and 5) 100 μM. Panel b) shows the corresponding extinction spectra with the dashed line representing the nanostructures grown in the absence of I^- for reference.

Experiments in which iodide ions were added to the growth solution were performed. The concentration of I^-, [I^-], was varied from 5 μM to 100 μM and the iodide ions induced significant morphological changes to the nanostructure within the nanoaperture. At 5μM I^- concentration (SEM inset panel 1) the nanoparticle-ring structure extends above the plane of the Au film, beyond the edge of the nanoaperture, and the nanoparticles appear to have fused into a relatively flat structure. As the iodide concentration is increased, nanoscale globular features are introduced into the nanostructure, disrupting the overall uniformity. This trend continues with subsequent increases in the iodide concentration. Extinction spectra for these structures (see Figure 5.4b) show a single asymmetric peak that begins at 600nm and extends out into the NIR. As observed in the case of Ag^+ ions, morphological changes in the nanoparticle-ring structure do not appear to significantly affect the resultant optical response aside from lowering the overall magnitude of the peak.

The stark contrast between the nanoparticles grown in the apertures and that reported for nanoparticles grown in solution raises some key questions regarding the mechanism behind the growth. The most striking difference is that the growth in the nanoapertures can initiate without the introduction of Au nanoparticle seeds, which is by far the most common approach used to initiate the CTAB / Au nanoparticle growth reaction in solution. Another contrast to reported

solution growth methods is the response of the system to the introduction of the shape directing ions Ag^+ and I^-. In solution, Ag^+ causes formation of nanorod type structures or nanostructures with spiked features,[20, 21] and the ratio between Ag^+ and Au^{3+} controls both the aspect ratio and overall yield of the final nanostructure. Also, Ag^+ has been used to generate complex nanostructures with high index facets; an outcome that has been attributed to underpotential deposition of Ag adlayers forming on the nanoparticle during growth[22]. Like Ag^+, I^- has been shown to affect the resultant nanoparticle structure[23] with the formation of spherical, rod-like, or triangular nanoprism structures as the primary reaction product, depending on the iodide concentration. The difference between the effect of shape directing ions in solution and in nanoapertures suggests that the seeds used to initiate the nanoparticle growth for the solution methods are critical to the shape directing mechanism; i.e. the shape directing ions effect is important in the earliest stages of growth. For the nanoapertures, however, the interface between the octadecanethiol monolayer along the edge of the nanoaperture must play the dominant role in both the nanostructure nucleation and shape direction during nanoparticle growth.

5.3.3 Influence of Alkanethiol Chain Length on Au nanoparticle Growth

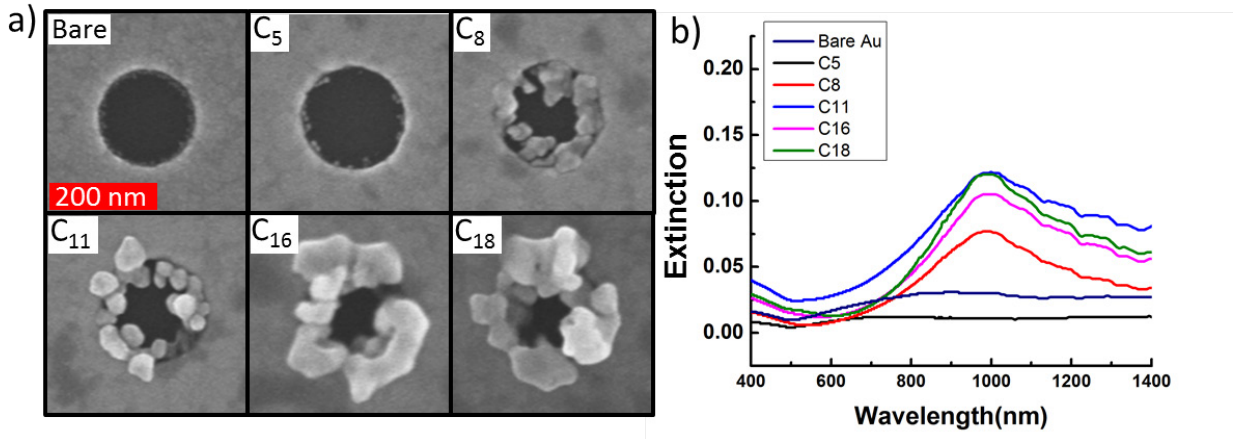

Figure 5.5. SEM images for CTAB/Au nanoparticles grown in 200nm average diameter nanoapertures functionalized with different chain length alkanethiols are shown in panel a) no alkanethiol (bare), pentanethiol (C_5), octanethiol (C_8), undecanethiol (C_{11}), hexadecanethiol (C_{16}), and octadecanethiol (C_{18}). The corresponding extinction spectra are shown in panel b).

To better understand the underlying mechanism behind the seedless nucleation and growth, as well as the shape directing effect of the SAM template, studies were conducted to elucidate the role of the alkanethiol SAM during nanoparticle growth. SAMs consisting of pentanethiol, octanethiol, undecanethiol, hexadecanethiol, and octadecanethiol were formed on the nanoaperture substrate and then they were reacted with a CTAB/Au growth solution with identical composition to that for the nanoapertures shown in Figure 5.2a inset panel 3. Figure 5.5a show representative images that were obtained for the different alkanethiol lengths. From these images, it is evident that nanoparticle nucleation and growth depends on the alkanethiol chain length. In the case of an unmodified Au film (panel Bare) little nucleation and growth is observed. Close inspection of the nanostructure indicates that extremely small (<5nm) nanoparticles are present along the side wall of the aperture which suggests some limited nucleation and growth upon the Au film. For the system modified with pentanethiol (panel C_5), there is a slight increase in the density of nanoparticles along the nanoaperture sidewall, however they remain extremely small. As the chain length was increased to octanethiol (panel C_8), systematic nucleation and growth of small Au nanostructures within the aperture are evident. With a further chain length increase to undecanethiol (panel C_{11}), hexadecanethiol (panel C_{16}), and octadecanethiol (panel C_{18}), the filling of the aperture with Au nanostructures is significant. The extinction data shown in figure 5.5b is in qualitative agreement with the observed onset of

significant nanostructure nucleation and growth for octanethiol and longer chain length alkanethiol SAMs. As seen previously, the extinction consists of a single peak that is onset at λ = 600 nm and extends towards the NIR. As the chain length is increased, the total magnitude of the extinction increases with minimal shift in the observed λ_{max}.

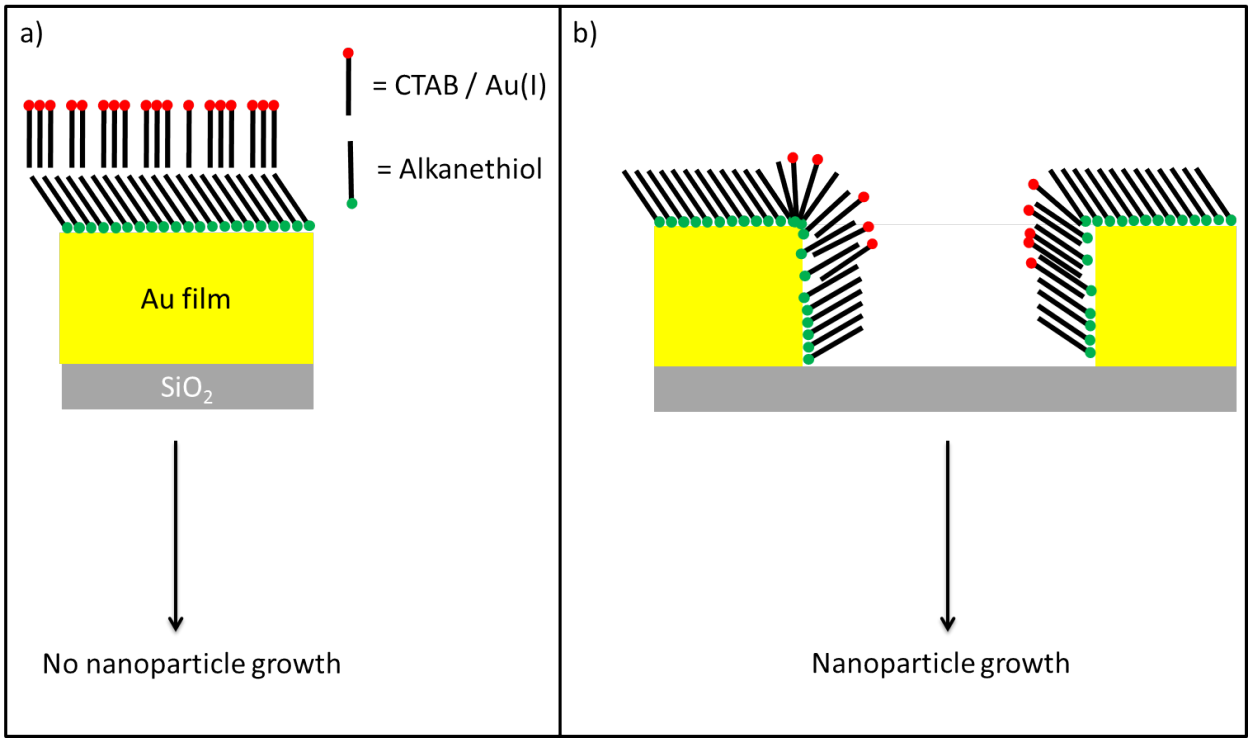

Figure 5.6. A cartoon diagram depicting the hypothesized mechanism for nanoparticle nucleation and growth selectively within alkanethiol functionalized nanoapertures. Panel a) depicts the interface between CTAB / Au moiety in the growth solution and a well packed alkanethiol monolayer on a planar Au film. Panel b) shows the CTAB / Au moiety and poorly packed alkanethiol monolayer interface on the Au film nanoaperture sidewall and ledge. It is expected that defects caused by the geometry of the nanoaperture enable insertion of the CTAB / Au moiety into the monolayer.

The proposed mechanism behind the seedless nucleation and growth of Au nanoparticle-ring structures from a CTAB / Au growth solution is presented in figure 5.6. Panel a) depicts the scenario in which the CTAB / Au moiety is present at the interface between the alkanethiol coated Au film and solvent. Interactions between amphiphilic molecules and hydrophobic SAMs have been well studied, especially for lipids[24]. In the case of CTAB, a cationic surfactant, it has been shown that it will form a bilayer at the interface between octadecanethiol and the solution[25]. Insertion into the SAM does not occur if the octadecanethiol forms a well packed monolayer. However, alkanethiol monolayers on nanostructured Au surfaces display an increased density of defects in the film.[26, 27] Because nanoparticle growth is seen almost exclusively within the aperture, it is likely that defects[28] in the SAM on the nanoaperture sidewall and ledge act as nucleation sites, and the reduced number of defects in the flat planar region reduces the likelihood of nanoparticle growth there. The higher density of defects in the aperture region, as compared to the Au film, likely allow for intercalation of the hydrophobic tail of the CTAB/Au moiety into the hydrophobic SAM (Figure 5.6b), enabling nanoparticle nucleation and growth. Since CTAB exhibits poor water solubility at room temperature, the mechanism by which CTAB inserts into the hydrophobic SAM is believed to be analogous to the self-healing mechanism utilized for alkanethiol monolayer wet etch resists[28-30]. That is, the poor aqueous solubility, which arises from the hydrophobic character of long alkyl chain, makes insertion into defect sites within alkanethiol SAMs energetically favorable. This conclusion is substantiated by the retarded nanoparticle nucleation / growth for the bare Au film and the short chain pentanethiol SAM, which would have a thermodynamically less favorable interaction with the C_{14} CTAB hydrophobic tail than for the longer chain alkanethiol SAMs. Also, the lack of non-specific nucleation and growth on the Au film suggests that the typical alkanethiol packing

geometry on thermally deposited polycrystalline Au does not contain sufficient density of defects to promote significant nanoparticle nucleation and growth. Future studies with branched alkanethiol monolayers that have controlled defect density would help elucidate the role of the monolayer defects in the nanostructure growth process.

5.3.4 Role of Alkanethiol Terminal Head Group

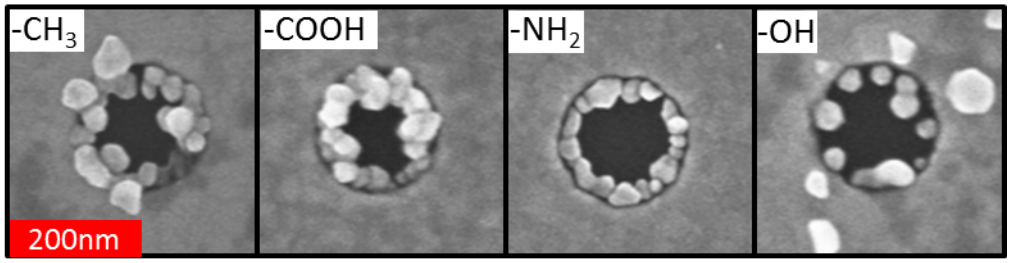

Figure 5.7. The effect of changing the alkanethiol SAM terminal functional group: SEM images of CTAB/Au nanoparticles grown in 200nm average diameter holes passivated with (–CH_3) undecanethiol, (-COOH) mercaptoundecanoic acid, (-NH_2) mercaptoundecylamine, and (-OH) mercaptoundecanol.

Another important property of the SAM is its terminal functional group, and its effect on the nanoparticle growth was examined C_{11} methylene chain alkanethiols. This chain length was chosen due to the commercial availability of various terminal head functional groups for this chain length. Mercaptoundecanoic acid, mercaptoundecylamine, and mercaptoundecanol were used and are shown to influence the final Au nanostructure grown within the nanoaperture. The SEM image in Figure 5.7 panel (-COOH) shows the effect of coating the surface with a mercaptoundecanoic acid SAM. In contrast to the undecanethiol SAM in panel (-CH_3), it is evident that the introduction of mercaptoundecanoic acid as the SAM in the template growth

(identical to previous conditions seen in Figure 5.2 panel 3) causes a better defined nanoparticle-ring structure; although the morphology is that of randomly oriented nanoparticles, they are better localized within the boundary of the nanoaperture. For a mercaptoundecylamine SAM (see Figure 5.7 panel $-NH_2$) the resultant nanoparticle-ring has an even better defined structured and the individual nanoparticles appear to have fused together to form a nanoring within the aperture. In contrast, the resultant nanostructure for the mercaptoundecanol SAM (Figure 5.7 panel -OH) gives rise to a much more poorly defined growth than the previous alkanethiolates. Instead of a fused nanoparticle-ring structure, the sample displays nucleation and growth of individual Au nanoparticles that are bound to the sidewall of the aperture. The ability of the terminal functional group on the SAM to influence the nanoparticle-ring morphology represents a novel approach for exerting control in templated anisotropic nanoparticle growth.

It remains unclear what underlying mechanism is responsible for the change in the resultant nanoparticle morphology and arrangement seen between the different terminal head functional groups. It is possible that electrostatic attraction or repulsion of the cationic CTAB surfactant with the positively charged amine functional groups and negatively charged carboxyl groups is the primary driving force. The local pH could also be responsible for the contrast. It has been shown that pH can have a significant impact on the nanoparticle growth process[31], and the pH at the surface will be different between the amine and the carboxylic acid SAMS in the unbuffered growth solutions used for this study. Another factor could be preferential binding of the functional groups to different Au crystal facets, which induce shape directing effects based on the interaction between the Au crystal lattice and the functional groups. Nevertheless, it is apparent that the interaction between the alkanethiol SAM and the CTAB/Au moiety is sensitive to the terminal head group of the SAM. This, coupled with the unusual response of the

nanoparticle growth to the shape directing ions Ag^+ and I^- suggest that for this system the mechanism for growth and critical parameters to introduce well defined shapes is different than for the analogous solution based synthetic methodologies for arbitrarily shaped noble metal nanoparticles.

5.3.5 CTAB Mediated Growth of Ag and Pd Nanoparticles in Nanoapertures

If the observed nanoparticle nucleation and growth is believed to be primarily caused by the interaction of the CTAB / metal ion complex with the alkanethiol SAM, then, any metal that can be grown in the presence of CTAB micelles and form complexes with the head group of the CTAB moiety should also be amenable to this method. To this end, both Ag and Pd nanoparticles were grown inside 200nm nanoapertures in a 30nm Au film that was coated with an octadecanethiol SAM. As for the Au nanoparticles, the nanoaperture enables nucleation and growth of Ag and Pd nanoparticles on the wall and ledge of the nanoaperture. The resultant nanostructures show novel orientation and morphology of the nanoparticle-rings, as compared to the Au nanostructures. For the Ag nanoparticles, the growth solution was essentially identical to the CTAB / Au solution used (47mM CTAB, 496μM Ag^+, 3 mM ascorbic acid) with the replacement of Au^{3+} with Ag^+ as well as 47mM NaOH added to raise the pH of the growth solution to enable [32] ascorbic acid to reduce Ag^+.

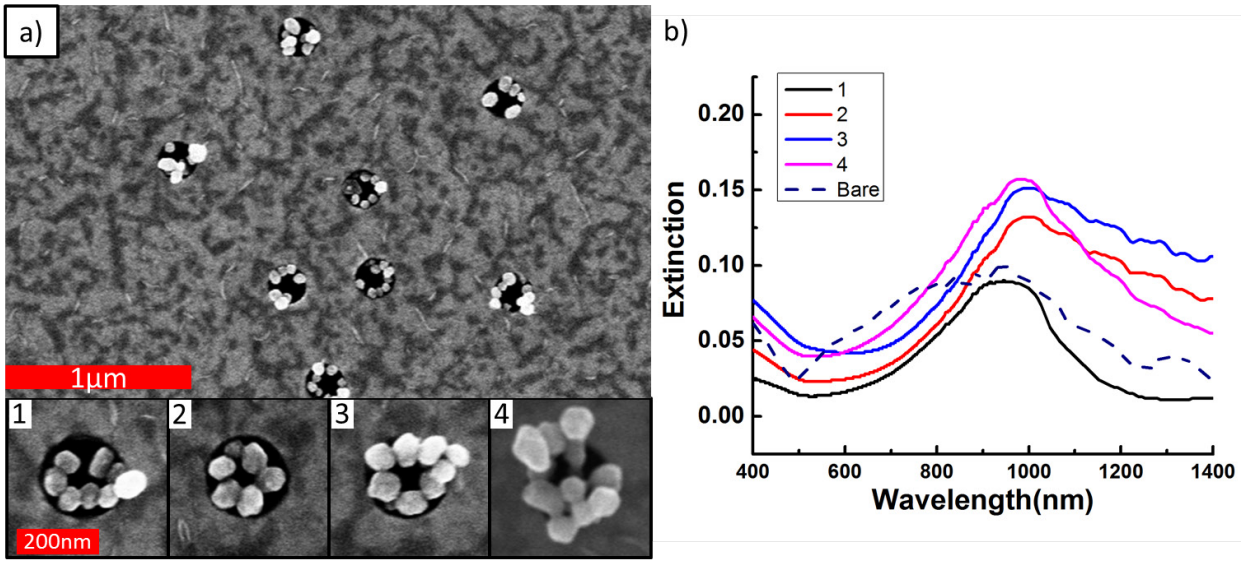

Figure 5.8. Panel a) shows SEM images Ag nanoparticle clusters synthesized upon 200nm diameter apertures that are randomly arranged in a 30nm thick Au film modified with an octadecanethiol self-assembled monolayer. Inset SEM images 1 – 4 show representative aperture/ nanoparticle clusters at higher SEM magnification for concentrations of Ag^{+} ranging from 1: 234µM, 2: 468µM, 3: 702µM, and 4: 936µM. The corresponding extinction spectra are shown in panel b) and for reference the dark field scattering spectra of the unmodified Au nanoholes is overlaid (dashed navy blue line).

The SEM image in figure 5.8 a) shows CTAB / Ag nanoparticles grown within 200nm nanoapertures for a 234µM Ag^{+} concentration. As with the CTAB / Au system, it is apparent that nanoparticle nucleation and growth is selective to within the nanoaperture. The Ag nanoparticles form tight clusters with an overall circular structure. The total concentration of Ag^{+} in the growth solution was varied and the results are shown in Figure 5.8a inset panels 1 – 4 which show magnified single apertures. It is clear that changing the Ag^{+} concentration in the growth solution from 234µM to 736µM results in no significant change in either the shape or

morphology of the Ag nanoparticle cluster within the aperture. However, as the concentration is increased to 936μM the nanoclusters appear to extend beyond the boundary of the nanoaperture and individual nanoparticles within the cluster appear to be larger and more randomly oriented. The extinction data is shown in Figure 5.8b and for each system, a peak is onset at λ = 600nm and extends out towards the Near-IR. For the Ag nanoparticles grown from the 234μM Ag^+ growth solution, the peak extends from 600nm to 1200nm. As the Ag^+ concentration is increased, λ_{max} red shifts ~50 nm, the magnitude of the extinction increases, and the peak becomes asymmetric tailing off into the Near-IR. This is a similar trend observed for the CTAB / Au system discussed in section 5.4.2. As with the CTAB / Au nanoparticle system, the observed extinction likely represents the collective resonances from the silver nanoparticle-ring structure in addition to the red-shifted resonance from the nanoaperture plasmon.

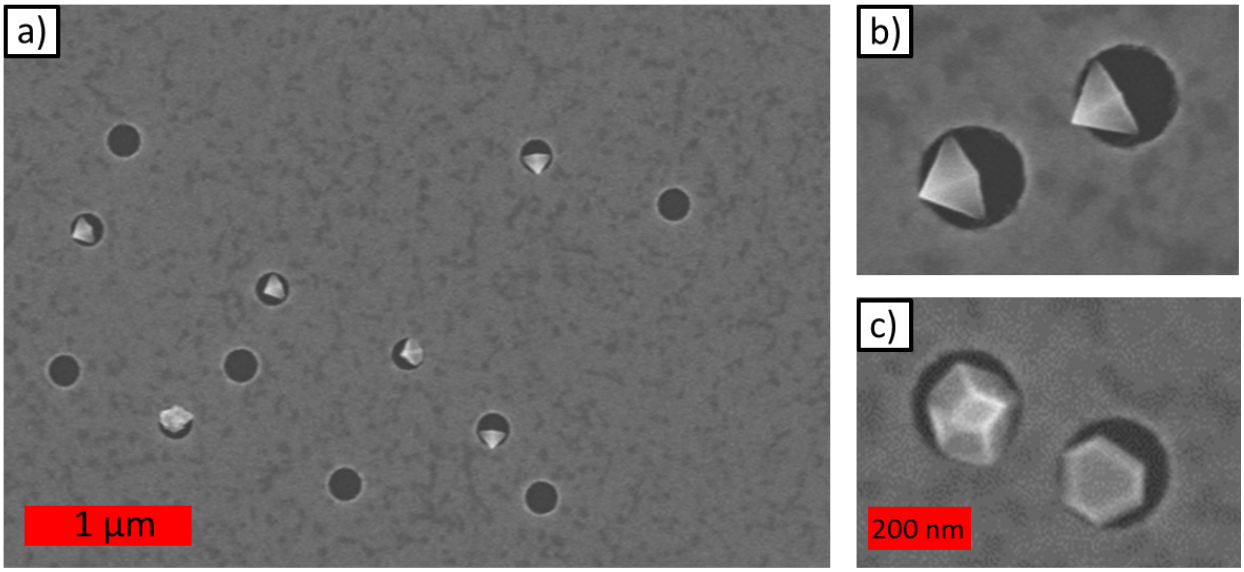

Figure 5.9. An SEM image for palladium nanoparticles grown within 200nm diameter nanoapertures in a 30nm thick Au film is shown in panel a). Panels b) & c) show magnified SEM images of individual nanoapertures with single palladium nanoparticles of different shape.

Palladium nanoparticles were also grown within the 200nm nanoaperture / octadecanethiol Au film templates. As seen in figure 5.9 a) individual palladium nanoparticles form within a nanoaperture or do not form at all. The nanoparticles appear either as an amorphous sphere or with a distinct geometry. It is evident that the nucleation and growth of the Pd nanoparticles does not occur within every aperture. It is possible that this is a direct result of the increased temperature (70^{o}C) used during the growth. The solubility of CTAB increases with temperature and thus the interaction between the hydrophobic tail of the CTAB moiety and the octadecanethiol SAM would become less thermodynamically favored. Looking at the magnified SEM images of the Pd nanoparticles (Figure 5.9 panel b and c), the Pd nanoparticles display unique anisotropic shapes. At this time, it appears that both the shape of the nanoparticle as well as its orientation within the nanoaperture are random in nature. Nevertheless these represent a novel heterometal plasmonic system which could have applications for both chemical sensing and catalysis.

5.3.6 CTAB/Au Methodology on Au Nanoparticle Templates

To explore the applicability of this methodology to structures other than nanoapertures, 80nm colloidal gold nanoparticles were investigated as templates. The 80 nm nanoparticles were immobilized onto an ITO substrate that was coated with a thin layer of the cationic polymer poly(allylamine); Au nanoparticles were then passivated with an octadecanethiol SAM, and the standard CTAB/Au nanoparticle growth was conducted with a growth solution identical that that used for nanostructures shown in Figure 5.2a panel 3. It is hypothesized that defects in the octadecanethiol monolayer, arising from the nanostructure of the colloidal Au nanoparticle

template[33] promote intercalation of CTAB/Au moieties at the SAM/solvent interface, and this feature will enable nanoparticle nucleation and growth on the colloidal Au template.

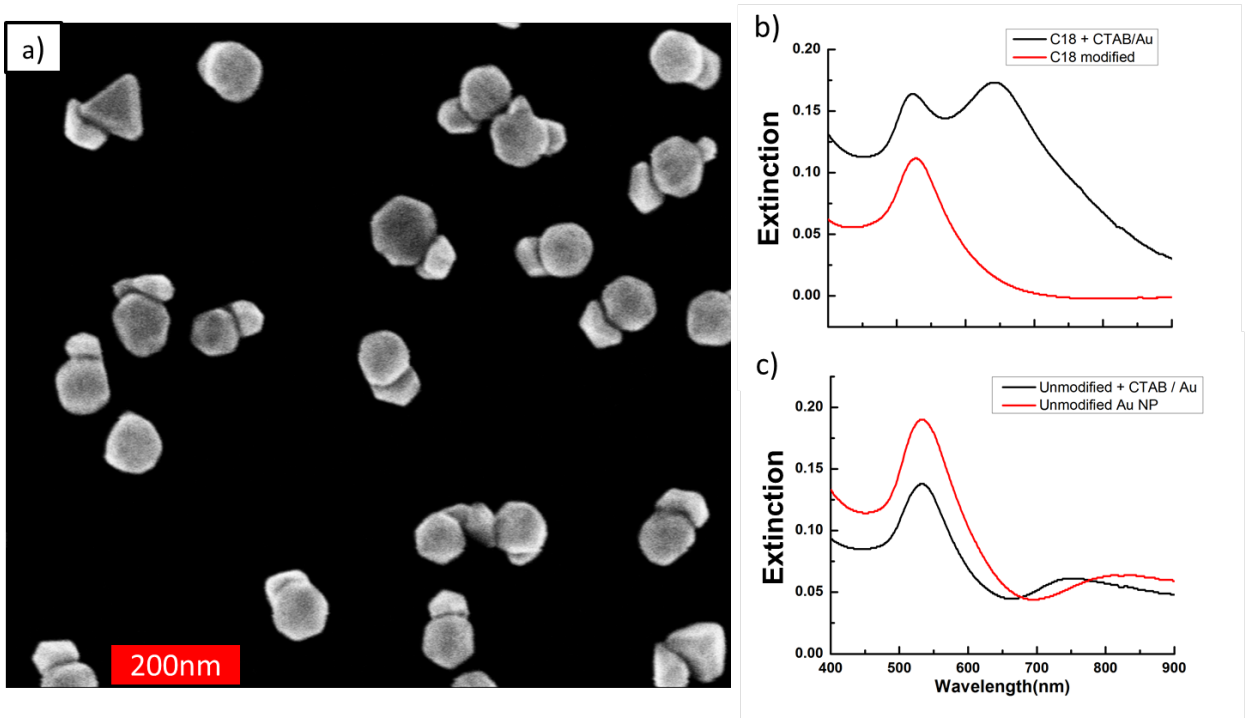

Figure 5.10. Templating methodology applied to colloidal nanoparticles: a) SEM image for 80nm colloidal Au nanoparticles modified with octadecanethiol and incubated with the default CTAB/Au growth solution and b) corresponding extinction spectra for the Au nanoparticles before and after the CTAB / Au nanoparticle growth. Panel c) shows spectra for the control sample consisting of 80nm Au nanoparticles without an octadecanethiol SAM both before and after the CTAB / Au reaction.

The SEM image in Figure 5.10 a) is for the 80nm Au nanoparticles after the growth reaction has completed. It is evident that nucleation and growth events occur on all but two of the 80nm Au nanoparticles within the field of view of the SEM image. It is also apparent that nucleation and growth events lead to dimers, trimers, and oligomers of Au nanoparticles with the majority of the nanostructures being dimers and trimers. For the dimeric nanostructures, a clear

separation between each nanoparticle is evident in the SEM image, which would correspond to a sub-5nm gap. In some cases it appears that the CTAB/Au nanoparticle follows the morphology of the 80nm colloidal nanoparticle template, forming a novel structural heterodimer.

Extinction spectra (Figure 5.10b) shows a red-shifted peak, which would correspond to the LSPR of the nanoparticle aggregate and a peak at 550nm that can be assigned to the off-axis excitation of the LSPR for the heterostructure. Conversely, for the control system without the octadecanethiol SAM, no change in the position of the extinction peak is evident(Figure 5.10 c), which is in agreement with the studies conducted for the Au film/ nanoaperture systems that found the alkanethiol SAM was critical for the successful nucleation and growth of the CTAB / Au nanoparticle. These results imply that alkanethiol modified Au nanostructures can serve as templates to create novel nanoparticle structures and orientations in clusters.

5.4 CONCLUSION

A seedless methodology for growing non-spherical Au, Ag, and Pd nanoparticles within 200 nm nanoapertures in alkanethiol passivated Au thin films and on 80nm colloidal Au nanoparticles immobilized onto an ITO substrate was developed. Studies into the nature of the reaction showed that the response of the system to changes in reactant concentration or through the introduction of shape directing ions strongly affects the growth, but these effects are quite different from the effects reported for anisotropic nanoparticle synthesis in solution. It was found that the nature of the SAM has a profound effect on the resultant nanoparticle orientation and geometry. This methodology represents a novel finding which should enable deeper insights into the mechanism behind surfactant mediated nanoparticle synthesis as well as the

development of novel nanoparticle / nanotemplate systems with interesting optical properties and applications.

5.5 REFERENCES

1. T. W. Ebbesen, H. J. Lezec, H. F. Ghaemi, T. Thio and P. A. Wolff, Nature **391** (6668), 667-669 (1998).
2. E. Popov, M. Nevière, J. Wenger, P.-F. Lenne, H. Rigneault, P. Chaumet, N. Bonod, J. Dintinger and T. Ebbesen, J. Opt. Soc. Am. A **23** (9), 2342-2348 (2006).
3. D. Gérard, J. Wenger, N. Bonod, E. Popov, H. Rigneault, F. Mahdavi, S. Blair, J. Dintinger and T. W. Ebbesen, Physical Review B **77** (4), 045413 (2008).
4. N. Djaker, R. Hostein, E. s. Devaux, T. W. Ebbesen, H. Rigneault and J. r. m. Wenger, The Journal of Physical Chemistry C **114** (39), 16250-16256 (2010).
5. A. Ahmed and R. Gordon, Nano Letters **11** (4), 1800-1803 (2011).
6. A. Ahmed and R. Gordon, Nano Letters **12** (5), 2625-2630 (2012).
7. Y. Xia, Y. Xiong, B. Lim and S. E. Skrabalak, Angewandte Chemie International Edition **48** (1), 60-103 (2009).
8. M. Grzelczak, J. Perez-Juste, P. Mulvaney and L. M. Liz-Marzan, Chemical Society Reviews **37** (9), 1783-1791 (2008).
9. I. H. El-Sayed, X. Huang and M. A. El-Sayed, Nano Letters **5** (5), 829-834 (2005).
10. H. Ko, S. Singamaneni and V. V. Tsukruk, Small **4** (10), 1576-1599 (2008).
11. A. M. Gobin, M. H. Lee, N. J. Halas, W. D. James, R. A. Drezek and J. L. West, Nano Letters **7** (7), 1929-1934 (2007).

12. X. Huang, I. H. El-Sayed, W. Qian and M. A. El-Sayed, Journal of the American Chemical Society **128** (6), 2115-2120 (2006).

13. M.-S. Hu, H.-L. Chen, C.-H. Shen, L.-S. Hong, B.-R. Huang, K.-H. Chen and L.-C. Chen, Nat Mater **5** (2), 102-106 (2006).

14. N. R. Jana, L. Gearheart and C. J. Murphy, J. Phys. Chem. B **105**, 4065 (2001).

15. J. Xie, J. Y. Lee and D. I. C. Wang, Chemistry of Materials **19** (11), 2823-2830 (2007).

16. P. C. Angelomé, H. Heidari Mezerji, B. Goris, I. Pastoriza-Santos, J. Pérez-Juste, S. Bals and L. M. Liz-Marzán, Chemistry of Materials **24** (7), 1393-1399 (2012).

17. J. Prikulis, P. Hanarp, L. Olofsson, D. Sutherland and M. Käll, Nano Letters **4** (6), 1003-1007 (2004).

18. N. A. Mirin, M. Hainey and N. J. Halas, Advanced Materials **20** (3), 535-538 (2008).

19. J. B. Schlenoff, M. Li and H. Ly, Journal of the American Chemical Society **117** (50), 12528-12536 (1995).

20. N. R. Jana, L. Gearheart and C. J. Murphy, The Journal of Physical Chemistry B **105** (19), 4065-4067 (2001).

21. T. K. Sau, A. L. Rogach, M. Döblinger and J. Feldmann, Small **7** (15), 2188-2194 (2011).

22. M. L. Personick, M. R. Langille, J. Zhang and C. A. Mirkin, Nano Letters **11** (8), 3394-3398 (2011).

23. J. E. Millstone, W. Wei, M. R. Jones, H. Yoo and C. A. Mirkin, Nano Letters **8** (8), 2526-2529 (2008).

24. S. Lingler, I. Rubinstein, W. Knoll and A. Offenhäusser, Langmuir **13** (26), 7085-7091 (1997).

25. R. N. Ward, D. C. Duffy, P. B. Davies and C. D. Bain, The Journal of Physical Chemistry **98** (34), 8536-8542 (1994).

26. E. Cortés, A. A. Rubert, G. Benitez, P. Carro, M. E. Vela and R. C. Salvarezza, Langmuir **25** (10), 5661-5666 (2009).

27. C. Vericat, G. A. Benitez, D. E. Grumelli, M. E. Vela and R. C. Salvarezza, Journal of Physics: Condensed Matter **20** (18), 184004 (2008).

28. I. Markovich and D. Mandler, Analyst **126** (11), 1850-1856 (2001).

29. M. Geissler, H. Schmid, A. Bietsch, B. Michel and E. Delamarche, Langmuir **18** (6), 2374-2377 (2002).

30. P. A. Lewis, Z. J. Donhauser, B. A. Mantooth, R. K. Smith, L. A. Bumm, K. F. Kelly and P. S. Weiss, Nanotechnology **12** (3), 231 (2001).

31. Liu and P. Guyot-Sionnest, The Journal of Physical Chemistry B **109** (47), 22192-22200 (2005).

32. N. R. Jana, L. Gearheart and C. J. Murphy, Chemical Communications (7), 617-618 (2001).

33. M.-C. Daniel and D. Astruc, Chemical Reviews **104** (1), 293-346 (2003).

6.0 CONCLUSIONS

The first part of this thesis described spectroscopic studies that provide fundamental insights into the mechanism of extraordinary optical transmission through nanoaperture array devices, (Chapters 2–4), and the second part describes exploratory studies that show how anisotropic nanoparticle growth techniques can be adapted to create novel nanoparticle-nanoaperture structures (Chapter 5). The nanoaperture arrays in these studies consisted of periodic optically resonant metallic structures either as coaxial apertures in which a metallic disk fills the center of an aperture or rectangular nanoslit structures with embedded nanoparticle chains. These device geometries provided a robust platform to probe the interaction between multiple plasmonic and diffractive processes that contribute to the overall optical response of these systems. For the templated nanoparticle – nanoaperture growth studies, soft lithographic techniques were used to create a disordered array of nanoapertures in thin gold films or randomly oriented colloidal nanoparticles bound to a transparent substrate. These systems were used to systematically probe the nature of the surface chemistry between the template structure and the solutions used during the growth of metal nanostructures in the nanoaperture. This work has yielded fundamental insight into the optical response of plasmonic systems in addition to the design and characterization of novel plasmonic structures.

In Chapter 2, annular aperture array (AAA) devices were fabricated and characterized. Systematic studies were conducted to probe the relationship between the optical transmission of

the device as a function of the array period. It was found that surface plasmon polariton (SPP) modes that are excited by the periodic nature of the device play a critical role in the observed transmission. This study was the first to show that AAA devices have transmission properties that are sensitive to the period of the array. To verify that the optical response was caused by SPP modes, asymmetric arrays were fabricated in which the period of the array was only changed along one axis. The observed transmission was found to be sensitive to the polarization of the incident light, and for cases in which the light polarization was aligned with the axis of the array in which the period was varied, the peak transmission wavelength displayed a shift, whereas when the polarization was oriented along the fixed axis of the array the transmission showed no dependence the array period. This observation confirmed the notion that plasmon modes excited by the periodic nature of the device are important to the overall optical response.

Chapter 3 extended the work from Chapter 2 by looking at the geometry of the aperture within AAAs and by conducting systematic comparisons with analogous nanohole array devices. Differences between the period dependent optical response of nanohole arrays and annular aperture arrays confirmed that the overall transmission in annular aperture arrays is more complex and that the current model used to describe the optical response of SPP modes is in poor agreement with experiment. To further understand the AAA transmission process, the geometry of the aperture was varied by changing the size of both the aperture and the central disk inside. These studies found that the peak transmission wavelength in AAA devices is sensitive to the inner radius of the metallic disk, not the outer radius of the aperture, which was in disagreement with reports that the TE_{11} waveguide mode of the coaxial structure was responsible for the optical response of the system. Our findings suggested that localized plasmon (LSP) modes excited within the central disk of the aperture were significant to the total optical response. This

fact was demonstrated through diffractive coupling experiments with square coaxial array devices that exhibited the classic diffractive interference effect observed for localized surface plasmons excited upon nanoparticle array devices. This finding suggested that the optical response of AAA devices is likely caused by a superposition of SPP modes and LSP modes.

Chapter 4 presented a novel nanoaperture array device that consisted of a nanoslit array in which each nanoslit contained linear chains of subwavelength nanoparticles, thus creating a nested nanoparticle / nanoslit (NPNS) array device. The optical response of these devices was systematically studied and it was found that the transmission in these devices arises from the LSPR modes excited upon the nanoparticles within the nanoslit. This work demonstrated that extraordinary optical transmission in a subwavelength device can be mediated solely by nanoparticle LSPR modes.

Chapter 5 described a templated method for the seedless growth of complex nanostructure upon nanoapertures in thin Au films. It was found that when the template structures were coated with a hydrophobic alkanethiol self-assembled monolayer, in the presence of the surfactant CTAB, it was possible to generate Au, Ag, and Pd nanoparticles and complex nanostructures selectively within the nanoaperture template. Systematic studies were conducted in which both the nature of the self-assembled monolayer, as well as the composition of the growth solutions, were varied. It was found that the interaction between the alkanethiol SAM and the CTAB surfactant plays a significant role in the nanostructure growth process. This methodology was extended to 80nm colloidal nanoparticles as templates and resulted in the formation of nanoparticle dimers, trimers, and oligomers with sub-5nm gaps. The nanoparticle structures grown on the template also seemed to conform to the template structure thus generating novel nanoparticle structures not previously seen.

In summary, the results presented in this thesis yield insight into the extraordinary optical transmission process in complex nanoaperture array devices as well as explore novel techniques for creating nanoparticles and complex nanostructures within optically resonant plasmonic templates. These studies should enable a better understanding of both the optical response of nanoaperture array devices as well as enable the creation of new plasmonic nanostructures with interesting optical properties.